UNIVERSIDAD NACIONAL AUTÓNOMA DE MÉXICO
PROGRAMA DE POSGRADO EN ASTROFÍSICA

Instituto de Astronomía

SIMULACIÓN DE CURVAS DE LUZ DE OCULTACIONES POR KBOS EN EL PROYECTO TAOS.

TESIS

QUE PARA OPTAR POR EL GRADO DE:

MAESTRA EN CIENCIAS (ASTRONOMÍA)

P R E S E N T A :

Águeda Paula Granados Contreras

T U T O R

Dr. Mauricio Reyes Ruíz.
Instituto de Astronomía, UNAM

Ensenada, B.C. Mayo, 2013.

UNIVERSIDAD NACIONAL AUTÓNOMA DE MÉXICO
PROGRAMA DE POSGRADO EN ASTROFÍSICA

Instituto de Astronomía

SIMULATION OF OCCULTATION LIGHTCURVES BY KBOS IN THE TAOS PROJECT.

THESIS

TO OBTAIN THE ACADEMIC DEGREE OF:

MASTER IN SCIENCE (ASTRONOMY)

P R E S E N T S :

Águeda Paula Granados Contreras

S U P E R V I S O R

Dr. Mauricio Reyes Ruíz.
Instituto de Astronomía, UNAM

Ensenada, B.C. May, 2013.

Un padre es un tesoro, un hermano es un consuelo: un amigo es ambos.

— Benjamin Franklin

You will teach to fly,
but they will not fly your flight.

You will teach to dream,
but they will not dream your dream.

You will teach to live,
but they will not live your life.

Nevertheless,
in every flight,
in every life,
in every dream,
the print of the way you taught,
will always remain.

— Mother Theresa

Abstract

The importance of this study is related to our present uncertainties in our knowledge of the spatial and size distribution of the TNOs. This characteristics are related, perhaps determined, by the actual theory about the formation and evolution of the Solar System is correct. The formation models, with their own considerations, can predict the present number and total mass of this objects. The distribution of objects with sizes lower than 30 km is of particular interest, since the known observational information about this objects is almost non-existent given the low amount of Sun-light they reflect. The objects studied in this thesis range from 0.4 to 30 km at a distance from Earth of 42 and 43 AU. The position of the object with respect to the opposition was also considered, 3 different positions were studied - 0, 45 and 60 degrees from opposition.

The aim of this thesis is to determine whether there will be an improvement in the detection of TNOs by the *Taiwanese-American Occultation Survey* (TAOS I), using the occultation method at a sampling rate of 10 Hz (with the recently installed frame-transfer cameras), instead of 5 Hz (at which the past image detectors of the project operate). The effective solid angle, Ω_e, is the ideal parameter to compare the efficiency of detection between the two sampling frequencies given its definition. To calculate Ω_e, the simulation of occultation lightcurves accounting for diffraction effects is needed, sampled at a frequency of 10 Hz and taking random values of the parameters that affect the shape of the lightcurve, to simulate the observational circumstances. Ω_e is closely related to the survey since we have to consider the characteristics of the TAOS I project, as its limiting magnitude ($m \leqslant 14.2$ at $\lambda \approx 600$ nm) and the CCDs technical specifications. The most important part is the "event recovery code", that not only simulates the lightcurves, but also determines whether the event is significant or not. In addition, the code implements a signal filtering (with 8 different filters) with the purpose of increasing the significance of the events that would be reflected in an greater value of the effective solid angle if compared with the non-filtered simulation. Each of the 8 filters differs from the others in the number of consecutive flux-points taken into account, e. g., the filter F1 and F4 operate in two consecutive points, in contrast to F8 which combine 10 points.

We found that there is an important improvement in the detection that would be expected just by increasing the sampling frequency to 10 Hz in the TAOS project.

The detection will be larger for each of the objects in the range of 0.4 to 30 km, even without taking into account the signal filtering and their corresponding values of Ω_e, in contrast with the case of sampling rate of 5 Hz. The detection improvement does not have a linear behavior, e. g., while an object of 30-km may be detected 2 times better by observing at 10 Hz instead of 5 Hz, an object of 0.5-km would have an improvement factor of 1000. Most of the filters used in this study proved to be useful to increase the significance of the events, however, none of them have a global effect, i. e., its efficiency depends on the size of the object. Several filters were chosen, those that maximized the value of Ω_e for 1-km and 30-km objects, where the opposition angle was considered also. In general, small objects are easier to detect if their opposition angle is greater than zero, since this parameter affects the duration of the occultation event, which in turn affects the number of measurements that make up the event. The best filters for the bodies of 1-km, are NF (non-filter) and F1, while for the 30-km object are F5, F6 and F8. This thesis lays the groundwork for future surveys for TNOs using the occultation method, given that we proved that the faster the sampling rate the difficulty for the survey to detect objects with sizes less than 1-km at 43 AU would be considerably smaller. There is still much work to do in this kind of study, like to also consider a variation in the semi-major axis of the objects and not just their size.

"Por muy larga que sea la tormenta, el sol siempre vuelve a brillar entre las nubes"
— Khalil Gibran

"Astronomy compels the soul to look upwards and leads us from this world to another."
— Plato

Acknowledgments

First of all, thanks to my family for their support. To my parents, who strove to make me get interested in knowledge, they succeeded. To Andy and Armando, my sister and brother, who helped me to take away the stress on those vacation days in which I was dedicated to my thesis, sometimes it is better being a little relaxed than having the cycled ideas.

Thanks also to my friends for giving me a supporting hand when I needed it the most. Carmen you know what I mean. Aceituna, thanks for those whole nights we worked together and for taking care of me.

Thank you very much to Mauricio Reyes, my tutor, and Matt Lehner for believing in me despite the long time between the initiation and completion of this work. Also to Kiwi Zhang and Esteban Luna for their help, time to explain me and above all, for their patience.

Without the economic support received after the end of the CONACyT scholarship I would not have finished this thesis and therefore either my master's degree.

Contents

h

List of Figures

List of Tables

Acronyms

TAOS I Taiwan-American Occultation Survey

TAOS II Transneptunian Automated Occultation Survey

TNO transneptunian object

KBO Kuiper belt object

OAN Observatorio Astronómico Nacional

SPM San Pedro Martir

OCO Oort cloud object

SMO slowly moving object

SDO scattered/ing-disk object

LPC long period comet

SPC short period comet

GMC giant molecular cloud

SPANISH SUMMARY.

Simulación de curvas de luz de ocultaciones por KBOs en el proyecto TAOS.

Introducción

La importancia de este estudio se relaciona con la urgencia existente en conocer la distribución espacial y de tamaños de los objetos transneptunianos (TNOs, por sus siglas en inglés), ya que al saber esta información se podrá determinar si la teoría actual sobre la formación y evolución del Sistema Solar es correcta. Los modelos, con sus correspondientes consideraciones, pueden predecir el presente número y masa total de estos objetos. Es de especial interés la distribución de objetos con tamaño menor a 30 km, ya que se cuenta con muy poca información observacional de los mismos. Esta falta de información tiene que ver con la cantidad de luz solar que estos objetos reflejan, dada su distancia al Sol y su albedo.

Esta tesis aborda la simulación de curvas de luz estelares en las que ocurren ocultaciones por objetos del cinturón de Kuiper (KBOs), como serían observados por el proyecto TAOS, con lo cual se busca calcular un parámetro muy importante en la determinación de la distribución de tamaños y espacial de los KBOs, el ángulo sólido efectivo. El valor del ángulo sólido efectivo es único para cada censo. El procedimiento y resultados descritos aquí son útiles no solo para KBOs, sino también para cualquier TNO, como lo son los objetos del disco dispersado (SDOs, scattered disk objects) y de la nube de Oort (OCOs).

Objetos transneptunianos.

Los objetos transneptunianos son aquellos que pertenecen al Sistema Solar y que tienen una órbita con semi-eje mayor más allá de la órbita de Neptuno ($a > a_N \sim$ 30 UA).

El escenario estándar de la formación del Sistema Solar empieza con un disco protoplanetario alrededor de una proto-estrella, compuesto de gas y polvo, del cual una gran cantidad de planetesimales (con tamaños $D \lesssim 1$ km) evolucionan. Los planetesimales colisionan unos con otros y muchos de ellos se funden en objetos de mayor tamaño. En el Sistema Solar externo, esto progresa hasta el punto en que la gravedad de dichos objetos es lo suficientemente fuerte que empiezan a atraer material gaseoso, hasta que se convirtieron en los planetas gigantes actuales. Los planetesimales restantes, por varios mecanismos, son removidos de la región planetaria del disco. Algunos son arrojados a orbitas distantes de los planetas gi-

gantes; en esta región, bastante alejada de los planetas, estos pequeños objetos ya no son afectados por perturbaciones gravitacionales de los planetas y pueden permanecer inalterados en las afueras del Sistema Solar por toda su vida.

El conocimiento observacional de los objetos transneptunianos es reciente, empezó con la detección de Plutón por Clyde Tombaugh en 1930. Edgeworth desarrollo la primera investigación cuantitativa sobre la posibilidad de existencia de un gran número de cometas potenciales formando un anillo más allá de las órbitas de Neptuno y Plutón (Edgeworth, 1943, 1949). Postuló un disco primordial de gas y pequeñas partículas sólidas orbitando alrededor del Sol, que en función de la distribución de densidad podrían causar que éste se condensara en varias subregiones, que posteriormente se fusionarían para dar nacimiento a los planetas mayores si el sistema es suficientemente denso. En la región menos densa de la nebulosa solar, como las cercanías de Neptuno y Plutón, los procesos de condensación no tendrían tiempo suficiente para operar totalmente, resultando en la inviabilidad de la formación de un planeta grande. Significando que la condensación, a grandes distancias del Sol, podría solo formar grandes cantidades de objetos relativamente pequeños, existentes en esa región a la fecha.

En «The Evolution of the Solar System», Edgeworth (1949) estimó un número y tamaño aproximado de la población de cometas potenciales ubicados más allá de Neptuno, considerando masas totales para el anillo de 0.1 $M_\oplus$ y 0.33 $M_\oplus$, encontró que debería haber 2000 millones de objetos con masas individuales $\sim 5 \times 10^{-11}$ $M_\oplus$[1] y 200 millones con $\sim 2 \times 10^{-9}$ $M_\oplus$. Además, concluyó que Neptuno representa el caso limite para la formación de un único planeta gigante en el Sistema Solar exterior, dejando aparentemente a Plutón como un problema abierto (es decir, si este es un planeta o un satélite que escapo de Neptuno).

La siguiente contribución fundamental en la investigación de los orígenes del Sistema solar vino de Kuiper, quien consideró en su trabajo (Kuiper, 1951a) el destino de un cinturón de material nebular más allá de Neptuno, extendiéndose desde aprox. 38 UA hasta 50 UA. Kuiper asumió que la temperatura de esta región era estable y lo suficientemente baja para que el vapor de agua, metano y amoníaco se condensara en forma de pequeñas piezas de hielo y posteriormente formaron hielos de unas decenas de centímetros de diámetro. Kuiper esperaba que estas «bolas de nieve» continuaran creciendo por alrededor de 1 Ga hasta tamaños de 1 km o incluso 100 km, resistiendo de esta manera la disipación de la nebulosa solar.

Jewitt et~al. (1992) descubrió el primer objeto con una órbita completamente transneptuniana, nombrado como 1992 QB_1, evento que confirmó la existencia del

1 Masa total del anillo: 0.1 $M_\oplus$.

cinturón de Kuiper hipotético y abrió la posibilidad de descubrir otros objetos transneptunianos. Este descubrimiento provocó preguntas acerca de si Plutón era realmente un planeta, dada su alta inclinación ($i = 17.2$) respecto de la eclíptica y su excentricidad ($e = 0.244$). A la fecha, se han detectado cerca de 1170 TNOs, según ha informado el Centro de Planetas Menores (Minor-Planet-Center, MPC) y Plutón es considerado como un miembro de una clase especial de estos objetos, los llamados PLANETAS ENANOS. El semieje mayor, excentricidades e inclinaciones de estos objetos se distribuyen en un amplio rango, como se muestra en la Fig. 0.1

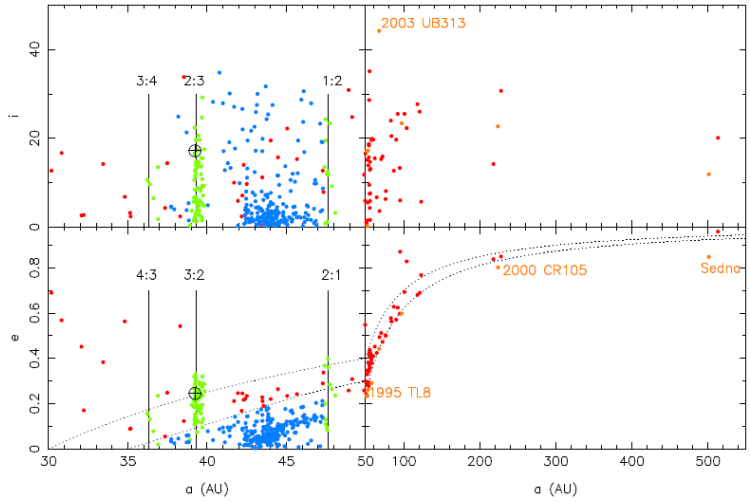

Figura 0.1: Distribución orbital de TNOs descubiertos hasta 2005. Panel inferior: gráfica de semi-eje mayor, a, contra excentricidad, e. Panel superior: inclinación orbital en grados, i, en función de a. Los SDOs se presentan en rojo, los objetos del disco dispersado extendido en naranja, los KBOs en azul y los objetos resonantes en verde. Las líneas punteadas en el panel izquierdo inferior indican, $q = 30$ y $q = 35$ UA, donde q es el perihelio; mientras que el panel derecho inferior $q = 30$ UA y $q = 38$ UA. Las líneas verticales marcan la ubicación de las resonancias 3:4, 2:3 (plutinos) y 2:1 con Neptuno. De Morbidelli (2005).

La población de objetos transneptunianos tienen una estructura orbital muy compleja, es por eso que se ha sugerido su división en subclases. Aún no hay un esquema de clasificación unificado, aunque algunos autores lo han intentado (Levison, 1996; Morbidelli, 2005; Gladman et~al., 2008). Las sub-poblaciones de TNOs aceptadas, con definición dependiente del autor, son la nube de Oort, el DISCO DISPERSADO[2] y el cinturon de Kuiper.

2 Gladman et~al. (2008) hace una breve discusión entre si el «disco dispersado» debe considerarse así o como «disco dispersante»

Disco dispersante/dispersado.

Morbidelli (2005) toma la disco dispersado, como la región de espacio orbital que puede ser visitado por cuerpos que tienen encuentros dentro del radio de Hill con Neptuno, al menos una vez desde la formación del Sistema Solar, para hacer esto, él asume que las orbitas de los planetas no han cambiado drásticamente. Los objetos que pertenecen a esta región en su clasificación, no parecen proveer ninguna información relevante acerca de la arquitectura primordial del sistema.

Dado que también existe una región bien poblada a la que se ha denominado como disco dispersado extendido o disco desprendido, no es completamente claro como se produjo el disco dispersado.

Después de reconocer que debe de haber una gran población de objetos en la parte externa del cinturón de Kuiper con pericentros desacoplados a Neptuno (Gladman et~al., 2002), fue definida una clase de *objetos transneptunianos desprendidos*, los límites de esta región se han ampliado a medida que se han ido descubriendo TNOs a distancias mayores del Sol.

Cinturón de Kuiper.

La región transneptuniana conocida como el cinturón de Kuiper es aquella que no puede ser visitada por objetos que tuvieron encuentros con Neptuno (Morbidelli, 2005). Los cuerpos de esta región son denominados objetos del cinturón de Kuiper con siglas en inglés KBOs.

El cinturón de Kuiper esta subdividido en dos: la población resonante y el cinturón clásico. Se espera que mientras que la excentricidad e inclinaciones de las orbitas de los objetos resonantes y dispersados deberían ser afectados por la interacción con Neptuno. No debería ocurrir lo mismo con los objetos de la población clásica.

La distribución de magnitud absoluta de KBOs puede ser determinada a partir de la función acumulada de luminosidad, que está dada por el número de detecciones que los censos reportan como función de su magnitud limitante, pesada por el inverso del área del cielo que los censos cubren. La pendiente de la distribución de tamaños resulta ser muy empinada, descrita por una ley de potencias con exponentes entre -3.5 y -3 para cuerpos con tamaños mayores de 100 km (Gladman et~al., 1998).

Stern (1995) encontró que los objetos que están actualmente en cinturón de Kuiper podrían no haberse formado en el ambiente presente. Sin embargo, las observaciones sugieren que cinturón de Kuiper primordial fue más masivo y dinámicamente frío, de tal manera que ocurrían más colisiones pero más suaves y por lo tanto había acreción de pequeños planetesimales.

Nube de Oort.

Se piensa que la nube de Oort es una población de planetesimales que fueron dispersados desde el disco planetario alrededor de 4.5 gigaños atrás. Esta población posee semi-ejes mayores entre $1000 \text{ UA} < a < 100,000 \text{ UA}$. Los modelos sugieren que estos objetos se formaron en la región de los planetas gigantes ($\sim 4 - 40$ UA) y que fueron perturbados por estos a orbitas con semiejes mayores más grandes, pero con el perihelio relativamente sin cambios. La influencia gravitacional de la marea galáctica, las estrellas pasajeras y las nubes moleculares masivas se vuelve importante para este tipo de objetos, dada su gran distancia con respecto al Sol.

IMPORTANCIA DEL ESTUDIO DE TNOS.

Los TNOs poseen huellas de los procesos de evolución y acreción que dieron forma al Sistema Solar externo actual, particularmente, proveen evidencia de cuales fueron los procesos físicos que ocurrieron ahí. Si queremos entender la evolución del Sistema Solar en la región externa, se necesita saber la masa total actual de esta población de objetos incluso si es insignificante con respecto a aquella de los planetas.

Hay dos características de la población de TNOs que nos dan una pista fundamental para revelar la historia del Sistema Solar: la distribución orbital y la de tamaños. Aunque ambas características son muy importantes, también hay otras, tal como sus propiedades físicas, que proveen información sobre los procesos físicos y químicos en la parte exterior del disco protoplanetario.

Aún perduran incertidumbres importantes en la distribución de tamaños y la masa total de los TNOs más pequeños, sobretodo de aquellos con tamaños menores a 10 km. Solucionar esta pieza del enigma de la formación del Sistema Solar es el objetivo del provecto TAOS.

Detección de objetos transneptunianos.

Los primeros censos del cinturón de Kuiper fueron conducidos con la suposición que los objetos descubiertos más allá de la órbita de Plutón no deberían de estar perturbados, siendo reliquias prístinas del proceso de la formación planetaria. Se esperaba también que sus orbitas fueran dinámicamente frías, circulares y de baja inclinación.

El primer objeto detectado con una orbita totalmente transneptuniana fue reportado por Dave Jewitt y Janet Luu en 1992 (Jewitt & Luu, 1993). Fue designado como 1992 QB_1. Hasta ahora se han detectado 1169 objetos transneptunianos y 439 centauros-SDOs, como reporta el Minor-Planet Center (2012). Su detección ha sido principalmente hecha por métodos de observación directa por telescopios en Tierra y espaciales.

Sesgos en la distribución orbital observada.

La determinación de la verdadera distribución orbital de los objetos transneptunianos no es fácil, una de las razones es que su detección y la determinación de los elementos orbitales de estos objetos esta altamente sesgado.

Kavelaars et~al. (2008) sugiere que los sesgos mas importantes presentes en los censos para la detección de TNOs son cuatro: el sesgo en flujo, el sesgo de apuntado, el sesgo de efemérides y sesgo de detección (ver Secc. 2.1). Señala, además, que los sesgos de flujo, apuntado y detección reflejan un problema intrínseco de observar objetos del Sistema Solar y que probablemente no puedan ser eliminados por estrategias de observación mas novedosas, pero que en cambio, el sesgo en efemérides puede ser reducido por un programa de observación bien planeado.

Método de observación directa de TNOs.

El método de observación directo consiste de tomar al menos 2 imágenes de un mismo con igual tiempo de exposición, separadas en tiempo 2 o mas horas. Después estas se comparan haciendo un parpadeo entre ellas buscando por un mo-

vimiento relativo entre alguno de los objetos. No todos los objetos que muestran un movimiento angular en ese lapso de tiempo son objetos transneptunianos, de hecho, un factor que determina si estos pertenecen o no a esta región es su baja velocidad, especialmente si esta es comparada con los cuerpos del cinturón de asteroides.

El movimiento angular paraláctico, al observar en oposición, brinda información directa sobre la distancia a la que los objetos detectados se encuentran. El valor típico del movimiento angular paraláctico de un objeto a 40 UA es de 3.19"/he y entre mas lejano sea el objeto este valor se reducirá.

Una de las debilidades de este método de observación es que si el albedo del TNO no es conocido, entonces no es posible calcular el tamaño del objeto.

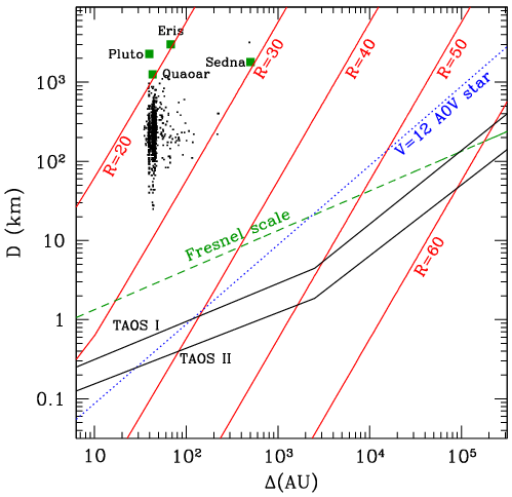

Figura 0.2: Diagrama de tamaño contra semieje mayor de los TNOs observados (puntos negros). La división entre la región donde ocurre solo óptica geométrica y aquella en donde hay un fuerte efecto de difracción se muestra en verde (Escala de Fresnel). En lineas rojas se muestra magnitud R constante de luz reflejada (con albedo 0.04). Adicionalmente se muestra la sensibilidad de los censos TAOS I y TAOS II en lineas negras.

MÉTODO DE OCULTACIÓN.

Esta técnica consiste en grabar, con una fotometría de alta velocidad ($f \sim 10 - 100$ Hz), el flujo estelar de una estrella cuando un objeto se acerca a la linea de visión de la estrella y después la oculta. Una ventaja general de esta técnica es que alcanza una alta resolución espacial de tal modo que se pueden detectar objetos de ~ 1 km.

La curva de luz que se esperaría de una estrella, sin ser esta una binaria, oscilaría alrededor de un valor constante de flujo (por el ruido de la señal). Sin embargo, la curva de una ocultación tiene una caída en el flujo cuando el objeto se encuentra total o parcialmente enfrente de la estrella sobre nuestra li-

nea de visión. Al estar utilizando ondas electromagnéticas para el estudio de estos objetos se debe tomar en cuenta que para algunos cocientes del tamaño del objeto ocultante y su distancia a la Tierra el efecto de la difracción sera predominante, tal como sucede para TNOs con tamaños del orden de 1-km. Por esto, se consideró en las simulaciones el efecto de la difracción.

PROYECTO TAOS.

TAOS I es el acrónimo en ingles para Taiwan-American Occultation Survey para la primera fase de este proyecto, su objetivo es buscar ocultaciones de estrellas distantes por objetos del Sistema Solar externo, principalmente TNOs. El conjunto de 4 telescopios, cada uno con 50 cm de apertura, del que se conforma el proyecto fueron diseñado para colectar imágenes a una cadencia de 5 Hz, frecuencia suficiente para detectar eventos de ocultación; además de encargarse de observar el número suficiente de estrellas (~ 1000) para una tasa de eventos significativa y que disminuya lo mas posible la tasa de falsos positivos. Esta etapa del proyecto se localiza en Taiwán, en el observatorio de la montaña de Lu-Lin. El sitio tiene un seeing medio de 1.3"(arcosegundos), con ~ 100 noches claras por año (Lehner et~al., 2007).

Su segunda fase (TAOS II) ha sido llamada Transneptunian Automated Occultation Survey, tiene el mismo propósito que el TAOS I, pero con varias diferencias técnicas importantes. Este poseerá 3 telescopios de 1.3 m y tendrá la capacidad de muestrear el flujo estelar a una frecuencia de 20 Hz. Adicionalmente, se planea que la señal a ruido se reduzca por el uso de CCDs diferentes. El objetivo principal de esta fase es tener una tasa de eventos mayor que TAOS I por un factor de 100. Esto se logrará con lo antes mencionado y al colocar los telescopios en un sitio con mayor número de noches claras por año (del orden de 250) como lo es el Observatorio Astronómico Nacional (OAN), localizado en San Pedro Martir (SPM) en México.

Recientemente se hizo una actualización en las cámaras del TAOS I, estas fueron cambiadas a CCDs frame-transfer, que permiten tomar mediciones fotométricas con una cadencia de 10 Hz, dos veces la pasada capacidad. El trabajo aquí realizado fue originalmente motivado por la necesidad de sacar el máximo provecho de estas nuevas capacidades.

Estadística de rangos.

La estadística de rangos es descrita a profundidad en la Secc. 2.4.1. Consiste básicamente en asignarle un rango a cada uno de los puntos en la curva de luz, donde el flujo de menor valor tiene asignado el valor 1 y el de mayor N_P, donde N_P es el número total de puntos en la curva. Esto se realiza con todas las curvas de luz de una misma corrida, es decir, las curvas que se observaron simultáneamente en distintos telescopios. Se tendrá una tupla de rangos r_{ij} donde i denota el telescopio usado y j el tiempo.

Después, se calcula el valor de probabilidad a partir del producto de rangos, y_j (Ec. 2.15). Este método para conocer la significancia estadística de un evento es descrita a profundidad por Lehner et~al. (2010).

La hipótesis que se planea rechazar con la estadística de rangos es la nula, es decir, la que señala que no ocurrirá ocultación alguna. El tiempo t_j donde la probabilidad sea mínima es la que nos interesa. Si este valor, además de ser mínimo, es menor al valor umbral (valor que cambia con el número de telescopios o pruebas independientes que se tengan) entonces el evento es estadísticamente significante y se puede considerar como recuperado o detectado. El valor de probabilidad ($valor - p$) umbral para $T = 3$ telescopios es de 10^{-11}.

Este calculo de la probabilidad es muy importante en este trabajo, ya que permite identificar si un evento puede considerarse como detectado dentro de la simulación.

Objetivos y justificación.

Este trabajo implicará la realización y el análisis de números simulaciones de curvas de luz de ocultaciones estelares por objetos del cinturón de Kuiper, en las cuales se considerará los efectos de difracción, todo con el fin de lograr los siguientes objetivos:

a) Cálculo de la probabilidad de detección de eventos de ocultación muestreando con una frecuencia de 10 Hz y considerando efectos de difracción dados los parámetros: parámetro de impacto, tiempo de compensación, magnitud y tipo espectral de la fuente, distancia y tamaño del objeto ocultante.

Los efectos de difracción en los eventos de ocultación dependen de varios parámetros, con el fin de determinar si un evento dado será detectado, teniendo en cuenta la cantidad de variables implicadas, necesitamos estimar un parámetro único que nos permitirá conocer esta información. Esto se logra mediante el cálculo de la probabilidad de un evento, por medio de la estadística de rango de cada punto de la curva de luz. Podemos discernir cuando un evento se produce si el valor de probabilidad ($valor - p$) de la prueba es mayor que el ruido.

b) Diseño y selección de filtros de señal para mejorar la probabilidad de detección.

Las curvas de luz de difracción toman diferentes formas dependiendo de los parámetros de los KBOs, en algunas de las curvas de luz la caída del flujo toma más de dos puntos contiguos, donde estos podrían tener el mismo rango. Por tal motivo, es necesario diseñar filtros de flujo para eliminar este efecto y mejorar así la probabilidad de detección. Entre los filtros diseñados se seleccionará aquel que maximice la probabilidad de detección.

c) Elaboración de una base de datos con las curvas de luz simuladas.

Esto es un subproducto natural del proceso de simulación y es de importancia ya que permite la comparación de éstas con las curvas de luz observadas para así obtener los parámetros principales correspondientes del TNO, es decir, su distancia a la Tierra y su tamaño.

Metodología.

El trabajo presentado en esta tesis se realizó en 2 etapas. La primera parte es principalmente descriptiva, consistió en la simulación de curvas de luz por ocultación con una variación sistemática de parámetros: compensación de tiempo, parámetro de impacto, magnitud estelar aparente y tipo espectral. El propósito de esta simulación fue evaluar el comportamiento del valor-p, en términos de los parámetros ya mencionados, y estimar crudamente qué valores resultan en un valor-p más significativo, y como secuencia, en una mayor recuperación de eventos de ocultación.

La segunda parte, se enfoca en el cálculo del ángulo sólido efectivo para varios tamaños de objetos situados a una distancia dada de la Tierra ($\Delta = 43$ UA). Fue necesario simular las detecciones aleatorias durante la observación de ocultaciones estelares KBOs, lo cual puede reflejarse al asignar valores aleatorios a algunos de los parámetros antes mencionados, tales como, el parámetro de impacto, el tiempo de compensación, la magnitud y tamaño angular aparente de la estrella. Sin embargo, establecimos valores fijos para los tamaños de objeto, su distancia a la Tierra e incorporamos la variación de su posición respecto a la oposición con la misma (ángulo de la oposición, ϕ).

En esta etapa, también, 8 filtros de señal se diseñaron e implementaron en las curvas de luz muestreadas con una cadencia de 10 Hz, estos filtros no son más que operaciones matemáticas entre mediciones consecutivas del flujo. Debido a la variación del tamaño de los objetos realizada, la pérdida de flujo toma en ocasiones más de 2 puntos consecutivos, lo cual reduce la importancia del evento, en otras ocasiones, la señal a ruido es muy baja y el evento suele confundirse con el ruido, es por ello que se realiza este filtrado, para evaluar si alguno de los filtros ayuda a incrementar la significancia estadística de un evento dado. La efectividad de los filtros se determina mediante la comparación del ángulo solido efectivo de los eventos recuperados con cada filtro con aquel obtenido al no usarlos.

Cómo simular las curvas de luz de ocultación.

El procedimiento básico para generar una curva de luz con muestreo finito es el que se enlista a continuación:

1. Generación de una tabla de difracción.

2. Generación de curva de luz de fuente puntual.
3. Establecimiento de la magnitud de la fuente de luz.
4. Generación de curva de luz de fuente con tamaño finito a partir de los 2 pasos anteriores.
5. Establecimiento del parámetro de impacto.
6. Conversión de la dependencia espacial a temporal usando la velocidad relativa del TNO.
7. Generación de curva de luz con tiempo de exposición finito.
8. Generación de curva de luz con muestreo finito de flujo.
9. Simulación e inclusión de ruido con determinado valor de señal-a-ruido, dependiente de la magnitud de la estrella.

Para una mejor descripción del mismo favor de revisar la Secc. 4.1.

	D	TIPO ESPECTRAL	b	t_{off}	M_*
Valores	0.6, 0.8, 1, 3, 5, 10, 20 y 30	F0V, G0V, K0III, K0V y M0III	$\triangle b = 0.05$	$\triangle t_{off} = 0.02$	$\Delta m = 1$
Rango	———	———	0 - 0.5	0 - 1	7 - 14
Unidades	km		H [km]	$1/f_{sam}$ [s]	mag

Tabla 0.1: Valores de los parámetros a usar para generar los diferentes patrones de difracción, donde D es el tamaño del TNO, b es el parámetro de impacto, t_{off} es la tiempo de desplazamiento con respecto al centro del patrón y M_* es la magnitud aparente de la fuente, que a su vez está relacionada con el tamaño angular de la estrella.

CÓDIGO DE RECUPERACIÓN DE EVENTO Y CÁLCULO DEL ÁNGULO SÓLIDO EFECTIVO.

Claramente, es conveniente conocer o estimar la cantidad que nos puede decir qué tan eficiente es un censo, como es el caso de la EFICIENCIA DE DETECCIÓN, ϵ_l, y EL ÁNGULO SÓLIDO EFECTIVO, Ω_e. Ambas cantidades están relacionadas, de alguna manera, con el número de eventos recuperados (o detectado), N_{rec}, y con el número total de eventos (simulado o añadido), N_{add}. La eficiencia de detección es la relación más simple entre estos dos cantidades, ya que es sólo el cociente

de ambas. Mientras que el Ω_e está «pesado» por las características de los eventos recuperados y no sólo su número.

Cobertura efectiva del cielo o ángulo solido efectivo.

La definición matemática del ángulo solido efectivo es:

$$\Omega_e(D,\Delta) = \frac{1}{\omega(D,\Delta)} \sum_{j=1}^{N_{rec}} \frac{v_{rel}(\Delta,\phi_j)}{\Delta} \frac{H_j(D,\Delta,\theta_*)}{\Delta} E_j \tag{0.1}$$

donde E_j es la duración en segundos de una serie de datos; H, es la sección transversal del evento (ver Equation 2.11c) y $\omega(D,\Delta)$ es el factor de peso para un objeto de tamaño D a una distancia Δ, i. e., la fracción de curvas de luz implantadas con ocultaciones por KBOs con un diámetro D a una distancia Δ de la Tierra. La suma es realizada únicamente sobre los valores de las curvas de luz con eventos recuperados. El factor de peso puede ser calculado en términos de la tasa de falsos positivos (0.25), el $valor-p$ umbral ($\mathbb{P}_{thr} = 10^{-11}$), el número total de mediciones de flujo (número total de puntos) en la curva ($N_P = 54000$) y el número total de curvas simuladas (N_{add}) (comunicación personal con Lehner y Zhang), está dada por:

$$\omega(D,\Delta) = \frac{N_{add}(D,\Delta)\, N_P\, \mathbb{P}_{thr}}{0.25} = 2.16 \times 10^{-6}\, N_{add}(D,\Delta) \tag{0.2}$$

	D	ϕ	b	t_{off}	M_*
Valores	0.4, 0.6, 0.5, 0.7, 0.8, 1, 2, 3, 8, 15 y 30	0, 45 y 60		Aleatorio	
Rango	———	———	0 - 0.5	0 - 1	7 - 14.2
Unidades	km	grados	H [km]	$1/f_{sam}$ [s]	mag

Tabla 0.2: Valores de los parámetros a usar para generar los diferentes patrones de difracción en la 2a fase de esta tesis (en el código `sim_rec.c`). Los valores de b, t_off, i_{in} y θ_* son aleatorios.

Hay un gran interés en determinar el ángulo sólido efectivo del proyecto TAOS I, sobre todo porque las cámaras fueron actualizadas y ahora tienen la capacidad de tomar imágenes a una velocidad de 10 Hz, Ω_e era desconocida antes de hacer este trabajo. Esta parte del trabajo se centra en su estimación.

La generación de las curvas de luz de ocultación siguió el procedimiento básico antes mencionado, esta vez, proporcionando valores aleatorios a los parámetros indicados en la Tabla 0.2. Además, para llevar a cabo la simulación, una selección

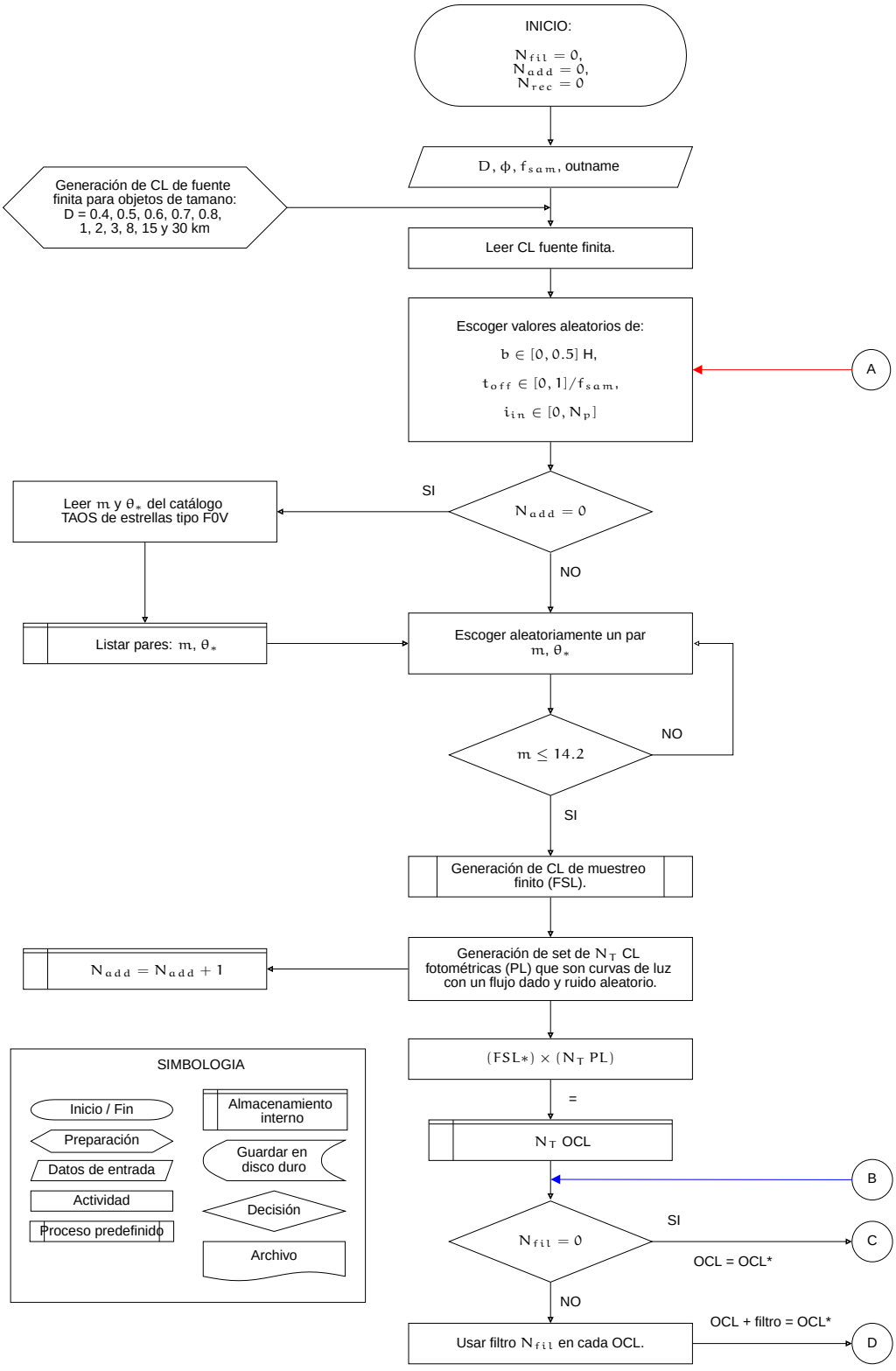

Figura 0.3: Esquema del código `sim_rec.c`. La definición de cada uno de los filtros se puede encontrar en 0.3 a 0.10.

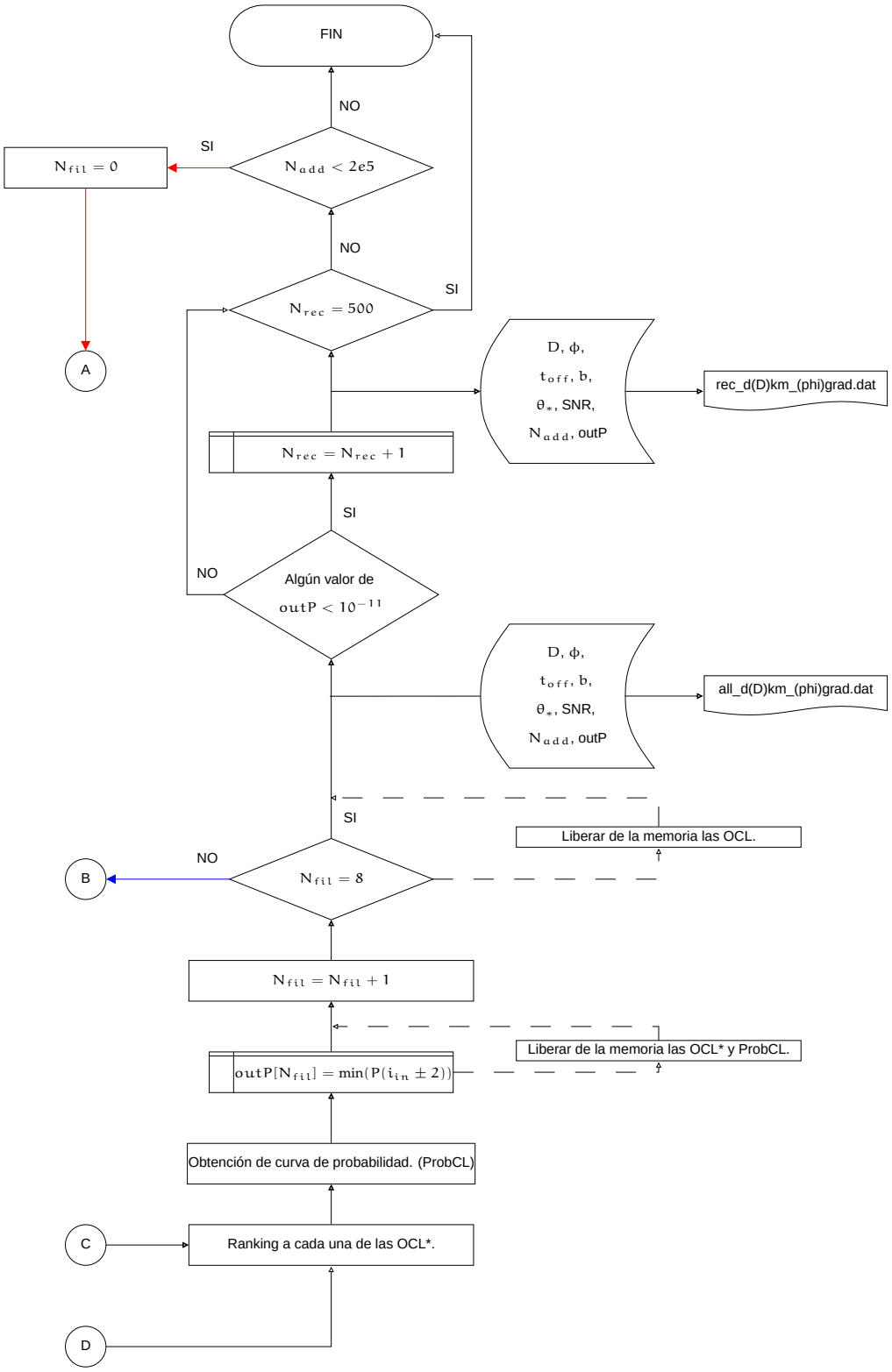

Figura 0.4: Esquema del código `sim_rec.c`. La definición de cada uno de los filtros se puede encontrar en 0.3 a 0.10.

aleatoria de tamaño angular estelar, θ_*, y la magnitud aparente, M_*, de un campo de estrellas de TAOS que se piensa observar (conteniendo información solo de estrellas F0V), se realizó con cada nuevo conjunto de curvas de luz. La magnitud varió desde 7 hasta 14.2 en longitud de onda roja, que implícitamente es una variación de la señal-a-ruido (SNR).

El código de recuperación, `sim_rec.c` es responsable, en términos generales, de crear las curvas de luz de difracción y fotométrica con los parámetros aleatorios mencionados en la Tabla 0.2, realizando la filtración del flujo con los filtros en la Secc. *Filtros usados*, calcular el $valor-p$ del evento simulado y determinar si es significativo y, si lo es, de guardar los valores de los parámetros de la curva de luz (especialmente los asignados al azar). Se tiene como entrada el tamaño del objeto en kilómetros, el ángulo de oposición deseada en grados y la frecuencia de muestreo (los valores concretos se pueden ver en la Tabla 0.2). Se utiliza como umbral para seleccionar qué evento se recupera el $valor-p$, $\mathbb{P}(Y \leqslant y) = 10^{-11}$. El algoritmo que `sim_rec.c` sigue se describe en las Fig. 0.3 y 0.4.

Como se puede observar, se producen 2 archivos de salida, que contienen los parámetros usados para producir N_{add} curvas de luz (`all*.dat`), de las cuales se recuperaron $N_{rec} \leqslant 500$ eventos. La información para los eventos recuperados se guarda en `rec*.dat`.

D	ϕ	t_{off}	b	θ_*	SNR	N_{add}	Valor-p mínimo para el filtro:								
							NF	F1	F2	F3	F4	F5	F6	F7	F8
							$j = i_{min} - i_{in}$ donde $\lvert j\rvert \leqslant 2$								
							NF	F1	F2	F3	F4	F5	F6	F7	F8

Tabla 0.3: Información contenida en los archivos de salida de `sim_rec.c`, donde F# hace referencia al filtro y su número, cuya descripción se encuentra en la Secc. *Filtros usados*, y NF significa No-Filtrado. El valor mínimo de la probabilidad fue es como se describe en la Fig. 0.4, donde j es el desplazamiento del mínimo del $valor-p$ con respecto al punto de inserción i_{in}; e. g., si el $valor-p$ mínimo se encuentra en el punto de inserción entonces $j = 0$, en cambio si éste está desplazado un lugar, entonces $j = 1$.

FILTROS USADOS.

Los filtros que se diseñaron y más tarde se aplicaron a las curvas fotométricas se describen en las Ec. 0.3 a 0.10. Para el diseño de los filtros se tomaron en cuenta operaciones matemáticas aplicadas a un número consecutivo de puntos sobre la

curva de luz; estos guardan cierta correspondencia con el número esperado de puntos que caracterizan la caída del flujo por la ocultación que depende tamaño del objeto. La ocultación por objetos de mayor tamaño conllevan eventos con mayor duración en tiempo, tal como la cantidad de puntos observados para una cadencia incrementa también para objetos mayores.

Tomando f_i como el valor del flujo a un tiempo i, los filtros que consideramos corresponden a las siguientes combinaciones de flujos:

$$F1_i = \frac{f_{i+1} + f_i}{2} \tag{0.3}$$

$$F2_i = f_{i+1} - |f_i - f_{i+2}| \tag{0.4}$$

$$F3_i = -|f_i - f_{i+1}| \tag{0.5}$$

$$F4_i = \frac{f_{i+1} + f_i + f_{i-1}}{3} \tag{0.6}$$

$$F5_i = \frac{f_{i+2} + f_{i+1} + f_i + f_{i-1} + f_{i-2}}{5} \tag{0.7}$$

$$F6_i = \frac{f_{i+3} + f_{i+2} + f_{i+1} + f_i + f_{i-1} + f_{i-2} + f_{i-3}}{7} \tag{0.8}$$

$$F7_i = \frac{f_{i+4} + f_{i+3} + f_{i+2} + f_{i+1} + f_{i-1} + f_{i-2} + f_{i-3} + f_{i-4}}{8} \tag{0.9}$$

$$F8_i = \frac{f_{i+4} + f_{i+4} + f_{i+3} + f_{i+2} + f_{i+1} + f_{i-1} + f_{i-2} + f_{i-3} + f_{i-4} + f_{i-5}}{10} \tag{0.10}$$

Dónde FX_i corresponde al valor del filtro X ($X = 1, ...8$) a un tiempo i. La mayoría de estas combinaciones pueden ser descritas como el promedio de un número determinado de mediciones consecutivas. El nivel de ruido es reducido en la señal filtrada y como resultado hay un incremento en el SNR y en la correspondiente probabilidad de detección.

Código que calcula el ángulo solido efectivo

Es esencial calcular, de una manera rápida y fiable, la Ω_e (Ec. 0.1) a partir de la información obtenida anteriormente. Así, un tercer código fue escrito, llamado `esolidang.c`. El cual lee el archivo de salida de `sim_rec.c` de los eventos recuperados y busca en las columnas con el $valor - p$ de los filtros si estos tienen un valor menor que el umbral y cuenta cada vez que esto sucede. Al final se obtiene el número de eventos recuperados por filtro, $N_{rec,F\#}$, y los parámetros con los cuales se puede recuperar el evento, el código entonces realiza la operación en la Ec. 0.1. De tal modo que se obtienen los valores de Ω_e para cada filtro.

Resultados.

Con la intensión de dar continuidad a lo descrito en la metodología (Capitulo 4), este capítulo se ha dividido en 2 partes.

comportamiento de la probabilidad para diferentes parámetros.

El número de curvas generadas en esta primera parte es de 140000, para analizar dicha información se tuvo que buscar una manera sencilla de interpretar ese número de curvas de luz. Se decidió crear isosuperficies del $valor - p$ en función de t_{off}, b, magnitud de la estrella y su tipo espectral. El $valor - p$ seleccionado es el mínimo en una ventana, ± 1, alrededor de aquel en donde sabemos que el evento fue insertado, i_{in}, y se observo como este valor se comportaba. El resultado son los mapas a color mostradas en la Fig. 0.5 (y mas adelante en las Fig. 5.2 y 5.3 de la Secc. 5).

La detección de un objeto dado puede ser realizada con menor dificultad si la fuente tiene una magnitud 7. Cuando el brillo estelar es reducido, es mas difícil detectar eventos (Fig. 5.1 a 5.3), particularmente de cuerpos pequeños. Hay una tendencia similar cuando el tamaño angular de la fuente es mayor, yendo desde tipos espectrales jóvenes a tardíos, dado que el efecto de difracción es más claro cuando la fuente tiene un tamaño puntual, especialmente la «profundidad» de la caída de la ocultación.

Como se puede observar en la Fig. 0.5, entre más pequeño sea el objeto, es más difícil observar la correspondiente reducción en flujo y por lo tanto su $valor - p$ tiene poca significancia. También se puede ver que para los objetos más grandes, como aquel de 30 km, el $valor - p$ no cambia con el tipo espectral ni con la magnitud. En todos los casos pareciera que éste tiene el mismo valor ($\mathbb{P} \sim 10^{-10}$). Este efecto se puede deber a que la duración de la ocultación, ya sea en tiempo o número de puntos muestreados, es muy amplia y el ruido en esta zona disminuye la significancia del evento (para más información consultar Secc. 6).

Figura 0.5: Mapa de color de probabilidad para estrellas de magnitud 7 y tipos espectrales: FoV, GoV, KoV, KoIII y MoIII. Se tomaron 3 tamaños diferentes para los objetos obstructores (KBOs), D = 0.6, 1, y 30 km. La barra de color muestra $\log_{10}(p)$, debe notarse que un valor menor de la probabilidad denota una mayor importancia en la detección del evento.

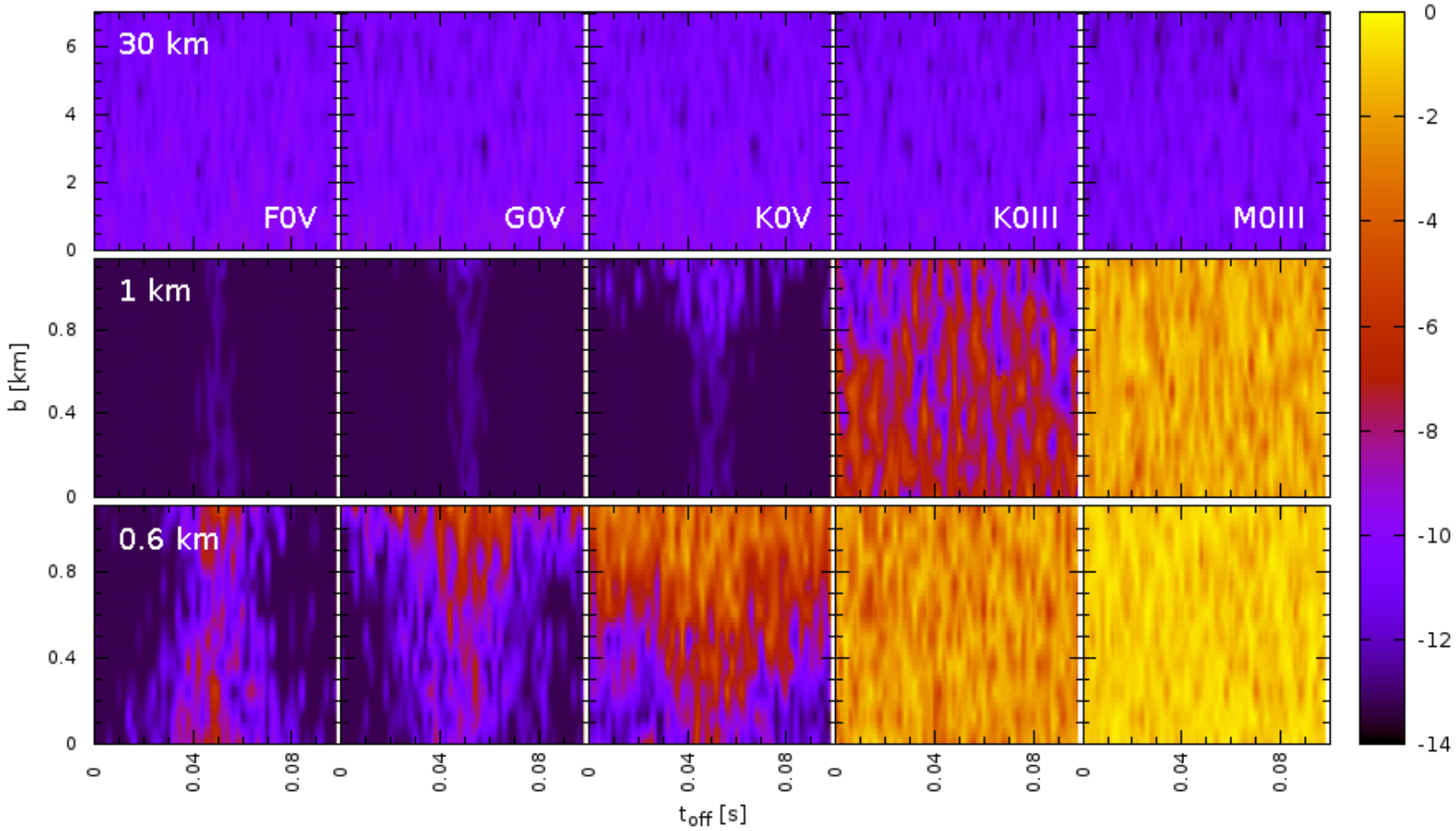

EFICIENCIA DE DETECCIÓN Y ÁNGULO SÓLIDO EFECTIVO.

La Tabla 0.5 muestra el número «crudo» de eventos recuperados, que significa que éste es el número de curvas con un evento detectado ya sea que fuese filtrado o no. De la tabla, uno puede calcular la eficiencia de detección del TAOS I a una frecuencia de 10 Hz. La eficiencia obtenida para cada uno de las tres ángulos de oposición estudiados en este trabajo son comparados con los resultados obtenidos por Bianco et~al. (2010) en la Fig. 5.4. Esta comparación exalta que se tiene una mejor detección de objetos del cinturón de Kuiper por el solo hecho de incrementar la frecuencia de 5 Hz a 10 Hz. Con estos resultados, uno esperaría que el ángulo solido efectivo también tuviera un valor mayor al obtenido por Bianco et~al. (2010) y Zhang et~al. (2008) que fueron calculados con una frecuencia de 5 Hz.

Los gráficos mostrados en las Fig. 5.5 a 5.8 ilustran los valores obtenidos para Ω_e para los diferentes filtros utilizados. Cada figura incluye la descripción del filtro y en todas ellas líneas grises que coinciden con los diferentes ángulos de oposición, la línea discontinua larga muestra a $\phi = 0$, la punteada corta a $\phi = 45$ y la discontinua larga-corta-corta a $\phi = 60$, para los valores de las curvas de luz que no fueron filtradas (NF, sin filtro utilizado).

De ser posible, es deseable un filtro único para todos los tamaños de objetos, si no, una alternativa es usar un filtro para objetos pequeños y otro para objetos grandes. En cualquier caso el filtro elegido para un tamaño en particular es aquel que tiene el ángulo sólido efectivo mayor. El filtro obtenido cuyo ángulo sólido efectivo es máximo se resume en la Tabla 0.4. El número de filtro que maximiza $\Omega_{e,D}(\phi)$ es dependiente de ϕ, por ejemplo, para el objeto de 1 km los filtros que maximizan $\Omega_{e,1}(\phi)$ son NF ($\phi = 0$) y F1 ($\phi = 45\,\&\,60$), mientras que para el objeto de 0,6 km son NF, F1 y F4. La dependencia anterior podría representar un problema si sólo se necesita un filtro para todos los ángulos de oposición dado un tamaño de objeto.

ϕ [°]\D [km]	0.4	0.5	0.6	0.7	0.8	1	2	3	8	15	30
0	NF	NF	NF	NF	NF	NF	NF	NF	NF	F2	F5 ó F6
45	F1	F1	F1	F1	F1	F1	F1	F1	F2	F4	F8
60	F4	F4	F4	F1	F1	F1	F1	F1	F4	F6	F8

Tabla 0.4: Filtros que maximizan a $\Omega_e(D, \phi)$.

D [km]	$\phi = 0^o$				$\phi = 45^o$				$\phi = 60^o$			
	$\overline{N}_{add}$	σ_{add}	$\overline{N}_{rec}$	σ_{rec}	$\overline{N}_{add}$	σ_{add}	$\overline{N}_{rec}$	σ_{rec}	$\overline{N}_{add}$	σ_{add}	$\overline{N}_{rec}$	σ_{rec}
0.4	200001.0	—	4.7	1.6	194268.6	18127.4	71.5	9.9	112544.0	3963.7	533.2	6.3
0.5	200000.0	—	230.0	9.4	60480.1	2601.4	602.3	11.7	14997.2	464.7	517.2	3.2
0.6	98377.6	2018.2	1152.5	25.0	15038.6	505.3	579.1	8.6	6502.2	293.9	514.9	4.5
0.7	23872.3	937.2	759.8	24.6	7431.6	248.5	559.3	7.9	3752.1	139.7	514.4	3.0
0.8	12397.6	350.5	683.5	16.5	4960.0	191.9	555.5	9.8	2583.4	123.9	513.8	2.4
1.0	5561.9	261.8	627.5	9.0	2650.1	127.2	548.5	6.6	1604.1	37.5	517.3	3.2
2.0	1507.4	61.6	552.4	10.3	1135.9	37.7	518.9	3.2	1014.8	33.2	502.8	2.6
3.0	976.5	19.5	527.1	4.3	860.4	26.3	514.5	3.9	802.9	17.3	502.6	1.5
8.0	618.2	6.9	512.1	3.0	594.2	3.4	506.6	1.7	582.6	14.3	501.0	0.8
15.0	541.6	7.2	504.3	1.8	538.0	4.1	501.8	1.9	541.5	5.8	504.6	1.5
30.0	515.2	3.0	500.8	1.2	518.9	4.1	503.0	1.6	799.0	14.5	525.8	7.0

Tabla 0.5: Valores promedio de N_{add} y N_{rec} por ángulo de oposición, ϕ, tomando en cuenta todos los filtros (ver explicación en el texto), y su respectiva desviación estándar, σ_{add} y σ_{rec}, después de haber corrido 10 veces el código `sim_rec.c`.

Ángulo sólido efectivo de combinación de filtros.

Esta sección puede ser considerada un producto del filtrado de las curvas de luz, se realizó para tener una comparación con los resultados de Zhang et~al. (2013), quien también uso filtros para mejorar la significancia de un evento candidato, además de combinaciones de los mismos (en pares). El producto de rangos descrito por Lehner et~al. (2010) tiene la desventaja de ser ineficiente al detectar eventos con duración larga (como ocurre con los cuerpos de mayor tamaño).

El programa, `fil_comb_rec.py`, escrito por la autora de este trabajo, realiza la combinación de pares de una muestra de los filtros, en ésta se excluyen los filtros F2 y F3. Lo anterior, posteriormente, deriva en el calculo de Ω_e para 21 combinaciones. Una vez determinada la combinación, el programa lee el archivo de salida de `sim_rec.c` con la información de todas las curvas simuladas y busca en las columnas correspondientes a cada uno de los filtros de la combinación con el propósito de encontrar el número de ocurrencias donde el $valor - p < 5 \times 10^{-12}$, y los parámetros de la curva respectiva (como se explica con mayor profundidad en la Secc. 5.2), sin discriminar si esto sucede en uno u otro filtro. El valor umbral de la probabilidad tuvo que ser considerado como la mitad de aquel considerado con un solo filtro, dado que cada filtro es una prueba independiente, y el falso positivo se hubiese duplicado de otra manera (Lehner et~al., 2010). En este punto se calcula $\Omega_{e,FF'}$, el subíndice FF' refiere a la combinación de dos filtros diferentes. El mismo procedimiento se repite para cada combinación, al igual que para cada tamaño y ángulo de oposición.

ϕ [°]\D [km]	1	30
		F1 y F6
0	NF y F1	F1 y F7
		F1 y F8
45	NF y F1	F1 y F8
60	F1 y F6	F6 y F8

Tabla 0.6: Par de filtros que maximizan $\Omega_e(D, \phi)$ para $D = 1$ y 30 km.

Nos concentramos en calcular el $\Omega_{e,FF'}$ para dos tamaños en particular, los objetos de 1 y 30 km. El ángulo solido efectivo calculado para estos objetos se puede encontrar en las Tablas 5.6 y 5.7. Mientras que el par de filtros que maximizan este valor se resumen en la Tabla 0.6.

Discusión y conclusiones.

Las simulaciones realizadas en esta tesis fueron divididas en dos etapas, las cuales tuvieron en común la distancia del KBO a la Tierra, $\Delta = 43$ UA. En la primera etapa, se consideraron variaciones sistemáticas de: tamaño del objeto, magnitud estelar, tipo espectral, parámetro de impacto y tiempo de desplazamiento; puede ser considerado un estudio descriptivo del comportamiento del $valor - p$, dados los parámetros antes mencionados. Este comportamiento puede ser observado en forma de mapas de color de la probabilidad (Fig. 5.1 a 5.3). La segunda parte es una estimación de la eficiencia de recuperación de eventos del censo, para el cual se usaron valores aleatorios de parámetro de impacto, tiempo de desplazamiento, magnitud y tamaño angular estelar. Se seleccionaron aquellos eventos cuyo $valor - p$ fue menor al umbral ($valor - p = 10^{-11}$) según Lehner et~al. (2010). De tal manera se obtiene la eficiencia de detección del censo y también el ángulo sólido efectivo, que mide el mejoramiento en el proyecto TAOS I dado el muestreo a 10 Hz en comparación con los resultados obtenidos para los datos a 5 Hz. En el cálculo del ángulo sólido efectivo, también se consideró el uso de filtros, combinaciones algebraicas de valores de flujos, con el propósito de evaluar si es posible que su uso incremente la eficiencia de detección para un evento dado.

Los mapas de color de probabilidad muestran las mejores condiciones para maximizar el número de detecciones por ocultación. En primer lugar, lo mejor es observar estrellas con una magnitud pequeña, i. e., con un tamaño angular que tienda a ser puntual. Objetos con tamaño mayor que la escala de Fresnel (para $\Delta = 43$ UA, $F = 1.39$ km) se detectan con facilidad en casi todos los casos, i. e., su detección es independiente de la luminosidad y el tamaño de la estrella. Si el tamaño del mismo $D \leqslant F$, su detección depende en gran medida de las características de la estrella observada. Cabe señalar que el tipo espectral en estos casos es sólo importante en la medida en que se relaciona con el brillo y el tamaño de la fuente, que a su vez corresponde a un tamaño angular determinado.

La eficiencia de detección, ϵ, como bien se mencionó, es el cociente entre el número de curvas de luz recuperadas y el total que se simuló, este valor es diferente para cada par de parámetros D y ϕ, y tiene una estrecha relación con el ángulo sólido efectivo, $\Omega_e(D)$. Comparando los resultados obtenidos en nuestra simulación a una cadencia de 10 Hz con el trabajo realizado por Zhang et~al. (2013); Bianco et~al. (2010); Zhang et~al. (2008) para el proyecto TAOS I, a una cadencia de 5 Hz,

y midiendo la mejora o falta de ésta mediante el cociente entre los ángulos solidos efectivos: $\triangle\Omega_e(D) = \Omega_e(10\,\mathrm{Hz},\, D)/\Omega_e(5\,\mathrm{Hz},\, D)$, obtuvimos que para objetos con $D = 30$, 1 y 0.5 km, sin considerar a ninguno de los filtros, existe un incremento: $\triangle\Omega_e(30) \sim 3$, $\triangle\Omega_e(1) \sim 13$ y $\triangle\Omega_e(0.5) \sim 200$. Mientras que, al tomar el valor máximo de Ω_e entre los 8 filtros: $\triangle\Omega_e(30) \sim 4$, $\triangle\Omega_e(1) \sim 15$ y $\triangle\Omega_e(0.5) \sim 700$.

Todos los filtros aquí diseñados mostraron ser útiles en incrementar la detección de eventos de ocultación a excepción de los filtros, F2 y F3, que involucran valores absolutos, como se muestra en las Fig. 5.9 y 5.10. Nuevamente, y como se esperaba, los valores de Ω_e dependen fuertemente del tamaño del objeto y de la oposición, lo cual repercute en que no exista un único filtro que incremente la detección de todos los tamaños de objeto en la misma medida. No solo eso, si consideramos un solo tamaño de objeto, el filtro que resulta en un valor mayor de Ω_e, no es el mismo para los 3 ángulos de oposición. Así, para cada tamaño se tendrá un trío de filtros que maximizan el valor de Ω_e, como se muestra en la Tabla 0.4.

Usando la información de los eventos recuperados por `sim_rec.c` para los diferentes filtros, se escribió un código que evalúa la detección conjunta de combinaciones a pares de los filtros, en tales combinaciones, los filtros F2 y F3 no fueron incluidos. Zhang et~al. (2013) realizó un estudio similar para una cadencia de 5 Hz y para diferentes filtros, en dicho trabajo se señaló que es necesario reducir el valor umbral de la probabilidad en función de cuantos filtros son combinados juntos. Para la presente, esto implicó la reducción del $valor - p$ umbral a la mitad, i. e., $valor - p = 5 \times 10^{-12}$. El correspondiente Ω_e fue calculado y graficado en las Fig. 5.17 a 5.21, en las cuales, Ω_e está normalizado al valor de la combinación Fo y F1, que de acuerdo con Zhang et~al. (2013) es el par de filtros cuya combinación maximiza Ω_e.

Estos resultados alientan la futura observación del proyecto TAOS I a una cadencia de 10 Hz, así como también el uso de filtros para incrementar la significancia estadística de los eventos. Es evidente que al aumentar la frecuencia de muestreo, el valor del ángulo sólido efectivo también incrementará, haciendo más sencilla la detección de objetos con $D < 1$ km, sin olvidar que la capacidad de la detección no solo depende del tamaño del objeto, sino también de la distancia de éste a la Tierra. Esto último se traduce como un fuerte aliciente para la implementación del proyecto TAOS II.

Part I

THE WHOLE WORK.

1

Introduction.

This thesis deals with the simulation of stellar lightcurves of occultations by KBOs such as would be observed in the TAOS project. The procedures and results described here are useful not only for KBOs, but also for any type of TNO, such as scattered disk objects (SDOs) and Oort cloud objects (OCOs).

1.1 Outline.

The introduction is divided in two chapters, the first will describe the general properties of TNOs, and in the second we expose the main methods to observe them. Section 1.2 describes the physical and dynamical properties of TNOs, what is believed to be (according to theory), their original evolution as well as a brief history of their study and observation. We also review how TNOs are classified, and why it is important to have more information about TNOs and their spatial and size distribution models.

In Chapter 2, we explain how these objects have been detected despite their distance and low surface brightness. We also review, the disadvantages and limitations of the current observing methods and the techniques proposed to overcome them. Additionally, we discuss the importance of the occultation method given its characteristics (Section 2.3). Included in the same chapter, is the definition of the several parameters that characterize an occultation light curve, emphasizing the ones that determine to the width and depth of the light curve.

The following chapters refer to the objectives of this thesis, the methodology, the results and the conclusions. The objectives of this thesis are described in Chapter 3. The methodology followed to simulate the lightcurves of occultations is described in Chapter 4. In Chapter 5 the results of our calculations are presented, while in Chapter 6 our conclusions and the corresponding discussion can be found.

1.2 TRANSNEPTUNIAN OBJECTS.

The transneptunian objects are those that belong to the Solar System and have an orbit with a semi-major axis greater than that of Neptune's orbit ($a > a_N \sim 30$ AU). The TNOs are considered to be mainly comet nuclei but as it will be seen, there are also dwarf planets that belong to these class of objects. The TNOs, as Morbidelli (2005) indicated, didn't have a consensual general nomenclature until recently. In his work, he considered as a TNO, any small object with semi-major axis (or equivalent orbital period) larger than Neptune.

The standard scenario for the formation of the Solar System begins with a protoplanetary disk, composed of gas and dust, out of which a large number of small planetesimals[1] (with sizes $D \lesssim 1$ km) that surround a protostar, evolves. The planetesimals collide with each other and many of them merge into bigger objects. In the outer Solar System[2], this evolves to the point where the gravity of such bodies is strong enough that begin to attract gaseous material until they become the current giant planets. The leftover planetesimals, by several mechanisms, are removed from the planetary region of the disk. Some are spewed to distant orbits by the giant planets. In this region, far enough from the planets, these small objects are unaffected by gravitational perturbations of these and can remain unaltered in the outskirts of the Solar system for its entire lifetime.

The observational knowledge of the transneptunian objects is recent, it began with the detection of Pluto by Clyde Tombaugh in 1930. This created a great commotion because it was not clear what kind of object Pluto was, was it the "Planet X" predicted by Lowell? if not, what was it?. Pluto was discovered following Lowell's interpretation of the small residual perturbations of Uranus as indicators of the presence of another distant planet (Tombaugh, 1946). In 1915, Lowell published "Memoir on a Trans-Neptunian Planet", where his solutions indicated that Planet X would have a mass of 1/50,000 $M_\odot$, or 7 times $M_\oplus$. Lowell started to search for the Planet X in 1905 and continued until his death in 1916.

Some authors, like Campbell (1916, 1919), Aitken (1926) and Leuschner (1927) had been speculating for many years about the possibility of transneptunian planets and the distribution of small bodies in the outer planetary system (cf. Leuschner, 1932; Öpik 1932), and had frequently considered comets in general to represent material that had been left over in the outskirts of the Solar System beyond the orbit of Neptune. Leuschner (1932) for example, was not certain that Pluto was a planet,

1 Strictly, the word PLANETESIMAL means an ultimately small fraction of a planet, this term is used mainly in planet formation theory, although it is also used to refer to small Solar System bodies.

2 The region where Jupiter, Saturn, Uranus and Neptune are believed to be formed.

instead, he thought it could be a large asteroid greatly disturbed in its orbit, or one of many long-period planetary system objects to be discovered or even a bright cometary object. Leonard (1930) pointed out that "... Now that a body of the evident dimensions and mass of Pluto has been revealed, is there any reason to suppose that there are not other probably similarly constituted, members revolving around the Sun outside the orbit of Neptune". Finally Pluto was considered the ninth planet of the Solar System, a status that changed after the discovery of 1992 QB_1.

Edgeworth developed the first quantitative investigation into the possibility of the existence of a great number of potential comets forming an annulus beyond the orbits of Neptune and Pluto (Edgeworth, 1943, 1949). He postulated a primordial disk of gas and small particles orbiting around the Sun, which depending of its density distribution could cause it to condense into various sub-regions, then merging to give birth to the major planets if the system is dense enough. In the region less dense of the Solar Nebula, like the vicinity beyond Neptune and Pluto, the condensation processes would not have sufficient time to fully operate resulting in an impossibility of forming any large planet. Meaning that the condensation, at great distances from the Sun, could only form large numbers of relatively small objects, that would be present there up to date (Edgeworth, 1943, 1949).

In "The evolution of the Solar System" Edgeworth, calculated an approximate number and size of the potential comet population beyond Neptune, considering total masses of the annulus between 0.1 $M_\oplus$ and 0.33 $M_\oplus$ and a semi-major axis distribution from 65 AU to 260 AU, then the annulus would be composed by about 200 million objects of individual masses about $2 \times 10^{-9}\, M_\oplus$ and 2000 million of $\sim 5 \times 10^{-11}\, M_\oplus$. Being Neptune the limiting case for the formation of a single large planet in the outer Solar System and apparently left to Pluto as an open problem (whether it was a planet or an escaped satellite of Neptune).

The next fundamental contribution to the research on the origins of the Solar System came from Kuiper who considered in his work (Kuiper, 1951a) the fate of a belt of nebular material beyond Neptune, extending from approximately 38 AU to 50 AU. Kuiper assumed that the temperature in this region, a relatively stable one, was low enough to condense water vapor, methane and ammonia to form tiny ices and subsequently form ices of a few tens of centimeters across[3]. He expected this "snowballs" would continue growing for about 1 gigayear up to 1 km or even 100 km, resisting in that way to the dissipation of the solar nebula.

3 "Snowballs"

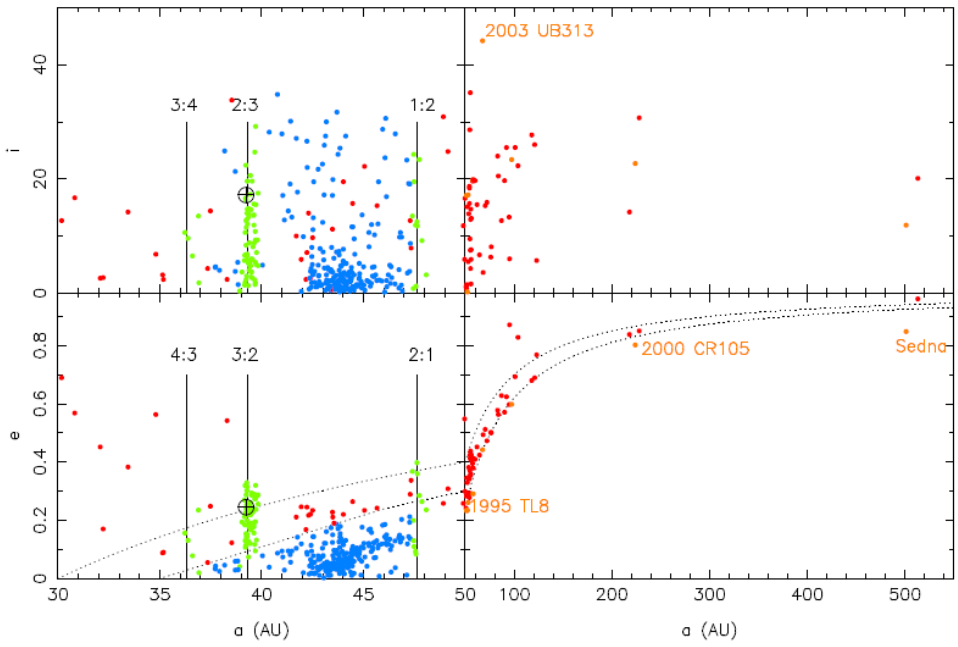

Figure 1.1: The orbital distribution of multi-opposition TNOs, as of Aug. 26, 2005. Lower panel: semi-major axis, a, is plotted versus eccentricity, e. Top panel: orbital inclination, i, in degrees as a function of a is shown. Scattered disk objects are presented in red, extended scattered disk bodies in orange, classical Kuiper belt in blue and resonant bodies in green. The dotted curves in the bottom left panel denote q = 30 AU and q = 35 AU, where q is the perihelion; those in the bottom right panel q = 30 AU and q = 38 AU. The vertical lines mark the location of the 3:4, 2:3 (plutinos) and 2:1 resonances with Neptune. From Morbidelli (2005).

Jewitt et al. (1992) discovered the first object having an orbit completely transneptunian named as 1992 QB_1, event that allowed the confirmation of the hypothesized Kuiper belt and opened the possibility to discover other transneptunian objects. The discovery of 1992 QB_1, resulted in the realization that Pluto maybe was not a planet, given its "high" inclination ($i = 17.2$) with respect to the ecliptic and its eccentricity ($e = 0.244$). Today, there have been detected about 1170 TNOs as reported by the Minor-Planet-Center (2012, Minor Planet Center) and Pluto is considered a member of a special class of these, the so called dwarf planets. The semi-major axis, eccentricities and inclinations of these objects are spread over a wide range as shown in Figure 1.1.

The transneptunian population has a very complex orbital structure so a division into subclasses is suggested. There is yet no unified classification scheme of the TNOs, although some authors have attempted to define one. Recent classifications

take relative stability of the body into account by using the Tisserand parameter [4] (Levison, 1996) to separate the Jupiter-family comets (JFCs) from the Centaur-like orbits. The JFCs have a short-period (< 20 yr), their current orbits are primarily determined by the gravitational influence of Jupiter and their semi-major axis is located within or not far from Jupiter's orbit. The JFCs' average inclination is about 18° from the ecliptic. Centaur-like objects are icy planetesimals with semi-major axis $5.2 < a < 30.2$ AU (between Jupiter and Neptune), their orbits are unstable because they cross the orbit of at least one giant planet and their dynamics is affected by the mutual interaction.

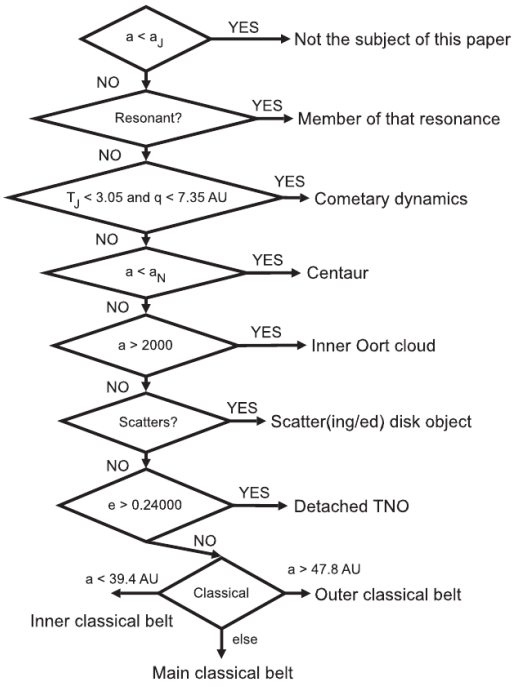

Figure 1.2: The classification scheme used by Gladman et al. (2008).

Other classification scenarios are based on the dynamics of the objects and their relevance for the reconstruction of the primordial evolution of the outer Solar System (Morbidelli, 2005). In contrast, Gladman et al. (2008) adopted a classification "philosophy" in which a TNO must be classified based upon its current short-term dynamics rather than a belief about either where it will go in the future or what it past history was, because TNOs might change class in the future.

The classification scheme followed by Gladman et al. (2008) is a process of elimination illustrated by Figure 1.2, based on either the object's current orbital elements and/or the results of a 10 My numerical integration of the object dynamics they made into the future. Gladman et al. (2008) have use the previous flowchart to classify the entire

4 The Tisserand parameter is an approximation of the Jacobi constant in the restricted, circular, three-body problem. The Tisserand parameter requires to be constant that the evolution of the comet is dominated only by a planet, and the comet must not be in a secular resonance or a close encounter with the planet (Morbidelli, 2005). The expression for the Tisserand parameter is:

$$T_P \equiv \frac{a_P}{a} + 2\sqrt{\frac{a}{a_P}\left(1 - e^2\right)}\cos i \tag{1.1}$$

where a, e and i are the semi-major axis, eccentricity and inclination of the small body. The sub-index P denotes the parameters for the planet.

three-opposition sample present in the IAU's Minor Planet Center (MPC) up until May 2006.

The following sections will briefly describe the properties of the scattered disk and Kuiper belt. We focus on the detailed characteristics of the Kuiper belt, as this thesis is mainly about the detection of objects that comprise it. Some of the features to be discussed are the distribution of principal orbital elements (a, e, i) of KBOs and the mass that the Kuiper belt is expected to have.

1.2.1 *Scattered/ing disk.*

Morbidelli (2005) takes as the scattered disk, the region of orbital space that can be visited by bodies that have encountered Neptune within a Hill's radius, at least once since the formation the Solar System, to do this he assumes that the orbits of the planets have not changed substantially. The objects that belong to this region in his classification do not provide any relevant information about the primordial architecture of the system.

Gladman et al. (2008) argues, that the term "scattered disk" was originally intended for TNOs scattered to high eccentric orbits with perihelion near Neptune. Even though the orbits in this "region" are not stable, because of the long orbital periods and sometimes near-resonant behavior with Neptune, some SDOs can survive ~ 4.5 Gy (Duncan & Levison, 1997).

Given that there is also a well-populated extended scattered/detached disk, it is not entirely clear how the scattered disk was produced. Gladman et al. (2008) suggests that the SDOs are those objects that are currently scattering actively off Neptune, rather than ascribing to this population any specific ideas about their origin.

Gladman et al. (2008) adapted a criterion similar to Morbidelli et al. (2004) to classify the scattered/ing-disk objects (SDOs): a change in semi-major axis $\triangle\, a \geqslant 1.5\mathrm{AU}$ during a 10 My integration, classifies the object as an SDO. Thus, SDOs in this definition are "scattering" objects rather than "scattered", even though the latter term is used without distinction in the literature.

After the recognition that there must be a large population of objects in the outer Kuiper belt with pericenters decoupled from Neptune (Gladman et al., 2002), a class of DETACHED TRANSNEPTUNIAN OBJECTS was defined, the boundaries of this region have expanded as more large-a TNOs are discovered. It is unclear if

this population was situated there by scattering.

1.2.1.1 *Extended scattered disk.*

There have been several TNOs discovered with $a > 50$ AU and highly eccentric orbits, according to Morbidelli (2005) these could not belong to the scattered disk. Some of them are 2000 CR_{105}[5], Sedna[6] and Eris[7]. Morbidelli (2005), following Gladman et al. (2002), considered them part of an EXTENDED SCATTERED-DISK for the following reasons:

1. They are very close to the scattered disk boundary.
2. The size of these three objects ranges from 300 to 2000 km and presumably where formed closer to the Sun, where the accretion time for solid bodies was short enough (Stern, 1996).
3. The lack of large objects ($D \gtrsim 300$ km) with $q > 41$ AU and $50 < a < 200$ AU should not be due to observational biases.

Taking into account the previous considerations, Morbidelli (2005) concludes that in the past the true scattered disk probably extended beyond its actual perihelion distance.

1.2.2 *Kuiper Belt.*

The transneptunian region known as the Kuiper belt is the one that can not be visited by bodies encountering Neptune (Morbidelli, 2005). In such a way that the non-negligible eccentricities and/or inclinations of KBOs can not been explained by the scattering action of Neptune in its actual orbit, instead they suggest the past existence of mechanism of excitation no longer operating.

The Kuiper belt population is subdivided in two: the RESONANT population and the CLASSICAL BELT. The resonant objects have a mean-motion resonance[8] with Neptune (especially the 3:4, 2:3 and 1:2 resonances) while the classical belt objects are not in any noticeable resonant configuration.

5 $a = 227.43$ AU; $q = 44.08$ AU; $i = 22.73^o$
6 $a = 536.7$ AU; $q = 76.34$ AU and $i = 11.92^o$
7 $a = 68.01$ AU; $q = 38.37$ AU and $i = 43.84^o$
8 A MEAN MOTION ORBITAL RESONANCE occurs when two bodies have an integer frequency of mean longitude, λ, respect to each other.

The mean motion resonances offer a protection mechanism against close encounters with the resonant planet, so that, the resonant population can even have Neptune-crossing orbits, with $q < 30$ AU (as Pluto). Bodies in 2:3 resonance with Neptune are called PLUTINOS on account of their Pluto-like orbits.

The classical belt is not confined between the 3:2 and 2:1 resonance, as it was once believed. Rather it also extends inward to the dynamically stable low-e region inside the 3:2 resonance (Gladman, 2002), and outward of the 2:1 resonance to the lightly populated low-e orbits (Figure 1.3).

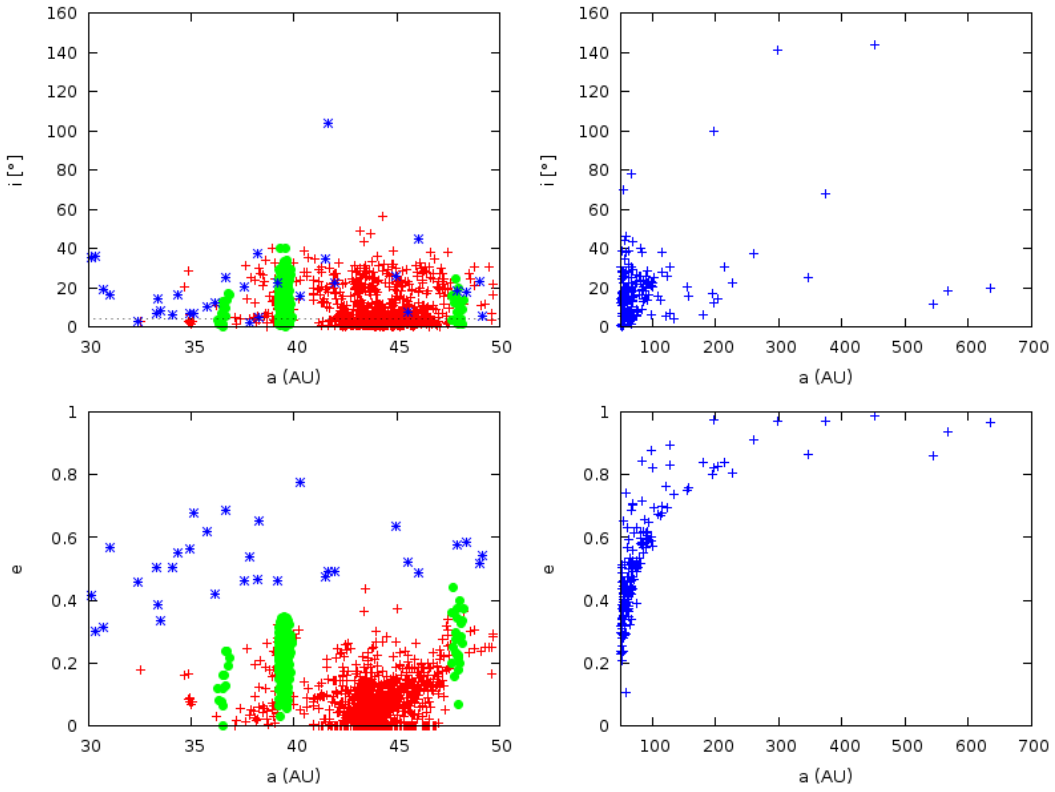

Figure 1.3: Similar plot to Figure 1.1 taking into account new TNOs discoveries since 2005 that show how the Kuiper belt is not limited by the 2:1 and 3:2 resonances. The green dots are the resonant population, the red plus sign can be interpreted as the classical population and the blue asterisks as the scattered disk population. The information was taken from Minor-Planet-Center (2012).

The gap present in the often-used low-i stability diagram of Duncan et al. (1995) is only present at low-i and is due to the ν_8 secular resonance[9]. The ν_8 is located at $a \simeq 41$ AU for low-i, but then moves to smaller a as i increases, rendering the $a = 39.4 - 42$ AU region stable for moderate and high inclinations.

Gladman et al. (2008) suggest that it could be useful to adopt a terminology to divide the classical belt into an INNER classical belt ($a < 39.4$ AU, non-resonant), an OUTER classical belt ($a > 48.4$ AU, non-resonant, and $e < 0.24$), and a MAIN classical belt (sometimes called cubewanos).

It is expected that while the eccentricities and inclinations of the resonant and scattered objects should have been affected by interactions with Neptune, those of the classical populations should not. However, the observed and confirmed classical belt objects have inclinations that range over 32 degrees (see Figure 1.4) and eccentricities that vary by 0.2, which does not agree with the values expected for a primordial low e and low i disk, even accounting for mutual gravitational perturbations (Morbidelli, 2005).

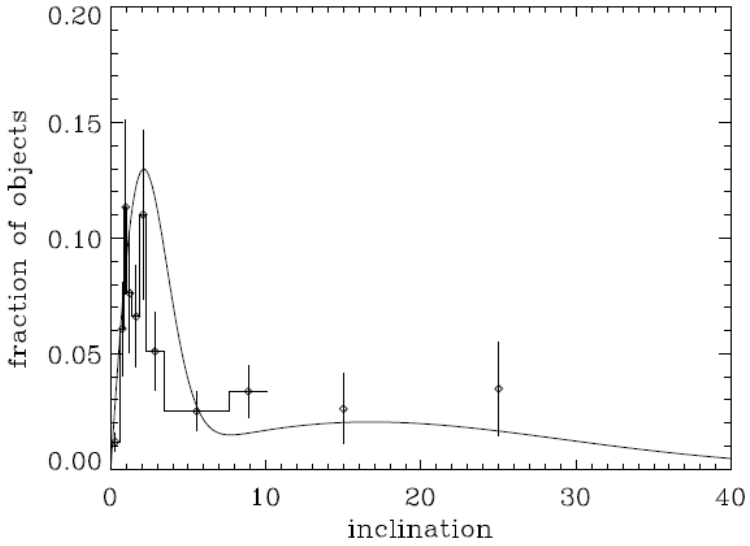

Figure 1.4: Inclination distribution, in degrees, of the classical Kuiper belt, from Morbidelli & Brown (2004). The points with error bars show the model-independent estimate constructed from a limited subset of confirmed classical belt bodies, while the smooth line shows the best fit two-population model extracted from Brown (2001).

9 A secular resonance is the synchronization of two (or more) orbits in their precession, which involves that the longitude of the perihelion, ϖ, and/or of the ascending node, Ω, is not constant in time. $\frac{d\varpi}{dt} = \frac{d\varpi'}{dt}$ or $\frac{d\Omega}{dt} = \frac{d\Omega'}{dt}$

The distribution of the observed parameters in the Kuiper belt, like eccentricity and inclination, is biased. Bodies with a high eccentricity approach closer to the Sun and they are easier to detect. In a similar way, the objects with high inclination spend little time at low latitudes at which most surveys take place. So, "what is the de-biased inclination distribution of the classical Kuiper belt look like?" Brown (2001) developed an answer to this question. The resulting de-biased inclination distribution, shown in Figure 1.4 with a smooth line, has a clear bi-modality with an important drop at 4^o, also, an almost flat distribution from 4^o to 30^o. Brown (2001) modeled the bi-modality as two Gaussian functions which suggest that the classical belt is conformed by a HOT ($i > 4^o$) and a COLD population ($i < 4^o$).

Gladman et al. (2008), in contrast, didn't felt necessary to use in their classification a division of the Kuiper Belt into a cold and hot population by its inclination, the authors argue that the distribution of KBOs is not yet sufficiently explored to draw an arbitrary division, especially since the plane to refer the inclinations is unclear.

After de-biasing the current TNO distribution as detected by several surveys[10], Kavelaars et al. (2008) concluded:

1. The "cold classical" component of Kuiper belt is delimited in semi-major axis $42.5 < a < 44.5$ AU and is low-inclination, low-eccentricity. This population represent $\sim$ 35% of the classical Kuiper belt population. As result, the models that suggest a cold belt with extension beyond 45 AU are rejected by observations.

2. The "hot classical" component of Kuiper belt represents about 65% of classical population. It contains objects with large eccentricities and a wide inclination distribution with a Gaussian peak at $i = 15^o$. This hot belt appears to uniformly fill the stable orbital phase-space between 35 and 47 AU and the detached objects may be the smooth extension of this population to larger a.

3. Many KBOs are in high-order mean motion resonances with Neptune, considered mistakenly as scattered disk objects.

Due to the origin that is attributed to the Kuiper belt, there are diverse expectations of what its properties should be. We have discussed already about the inclination and eccentricity distribution of the KBOs, what about its radial distribution? It is expected that the surface density of Kuiper belt object slowly decreases with heliocentric distance (Stern, 1996), considering this an extrapolation of the surface density as given by the minimum mass solar nebula (Hayashi, 1981). The lack of objects detected outward of around $a \sim$ 50 AU, led some authors (Jewitt

10 The biases that Kavelaars et al. (2008) considered are described in Section 2.1.

et al., 1998; Chiang & Brown, 1999) to suggest that a sharp drop-off in the number density of KBOs at such distances. Although there are arguments that suggest it could be an observational bias on account of the extreme faintness of these bodies, Allen et al. (2001, 2002) showed that the number of objects with $a < 50$ AU was greater than the number at $a > 50$ AU for a fixed absolute magnitude distribution, thus, some decline in the density should exist.

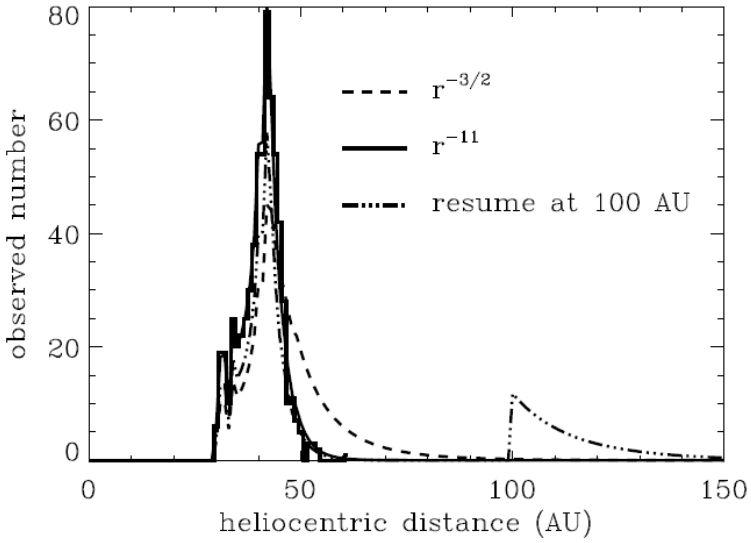

Figure 1.5: The observed radial distribution of KBOs (solid histogram) compared to radial distributions expected for models; (a) where the surface density of KBOs decreases as $r^{-3/2}$ beyond 42 AU (dashed curve), (b) where the surface density decreases r^{-11} beyond 42 AU (solid curve), and (c) where the surface density at 100 AU increases by a factor of 100 with respect to the value expected from an extrapolation for the minimum mass solar nebula (dashed-dotted curve) (Morbidelli & Brown, 2004).

Trujillo & Brown (2002) developed a method to use all the detected objects to make an estimation of the Kuiper belt radial distribution. They also compare a hypothetical radial distributions with observations (Figure 1.5). The drop-off beyond 42 AU is not consistent with the expected smooth decline of the surface density as $r^{-3/2}$, but can be fitted to a power law $r^{-11\pm4}$ (a much steeper one). More detections are necessary to rule out the previous distribution or even the one suggested by Stern (1996), who speculated that beyond some range of Neptune's influence, the number density of KBOs could increase back up to the level expected for the minimum mass solar nebula (Hayashi, 1981).

The slope of the cumulative size distribution can be obtained from the absolute magnitude distribution Figure 1.6, assuming an albedo distribution of KBOs inde-

pendent of their size (Morbidelli, 2005) [11] . The absolute magnitude distribution of KBOs is determined from the CUMULATIVE LUMINOSITY FUNCTION ($n(H)$), which is the amount of recorded detections of a survey in function of its limiting magnitude[12], weighted by the inverse of its covered sky area (Morbidelli, 2005). The size distribution turns out to be very steep, with an exponent of the cumulative power law between -3.5 and -3 for bodies larger in diameter than $\sim$ 100 km (Gladman et al., 1998). Actually, the size distribution is slightly shallower for the hot population of KBOs than for the cold population, as shown in Figure 1.6.

The slope of the size distribution below 100 km remains uncertain because of small number statistics. Given the previous uncertainties, as well as in the mean albedo of KBOs and their density, the total mass of the Kuiper belt is not yet determined. The uncertainty ranges an order of magnitude, with estimates ranging from 0.01 $M_\oplus$ (Bernstein et al., 2004) to 0.1 $M_\oplus$ (Gladman et al., 1998).

The surface density in the minimum mass solar nebula inferred from the total planetary mass (plus lost volatiles, Hayashi, 1981), is expected to decline smoothly outward from the orbit of Jupiter to the orbit of Neptune. The extrapolation and the integration of this surface density distribution predicts the total mass of solids originally in the 30 - 50 AU region (assuming a 100:1 gas/dust ratio) should have been $\sim$ 30 $M_\oplus$. Additionally, Stern (1995) found that the objects currently in the Kuiper belt could not have formed in the present environment: collisions are so

11 The absolute magnitude H (visual magnitude of an object in the hypothetical situation of being located simultaneously at 1 AU from Earth and Sun in opposition) is related to the size, D, and geometric albedo, p, of an object by:

$$H(D,p) = H_0 - 5\log D - 2.5\log p$$
$$H_0 - H = 5\log D + 2.5\log p$$
$$Z = X + Y$$

where $Z = H_0 - H$, $X = 5\log D$ and $Y = 2.5\log p$. H_0 is a constant that depends on the magnitude system.
Assuming that: 1) the objects are spherical, 2) the size, shape and albedo is independent of their orbital parameters and 3) the geometric albedos have discrete values ($f(p) \propto \sum_j^m p_j$), we can determine the size distribution from the absolute value distribution by:

$$n(X) = \frac{1}{2\pi}\int dk \frac{\int dZ\, n(Z)\, e^{-ikZ}}{\int dY\, f(Y)\, e^{-ikY}}\, e^{ikX}$$
$$n(X) \leftrightarrow n(D)$$
$$n(D) = \left|\frac{\partial X}{\partial D}\right|_D n(X(D))$$

where $f(p)$ is the is the probability density of geometric albedos. (Muinonen et al., 1995)

12 The limiting magnitude is the faintest apparent magnitude of a celestial body that is detectable or detected by a given instrument or survey.

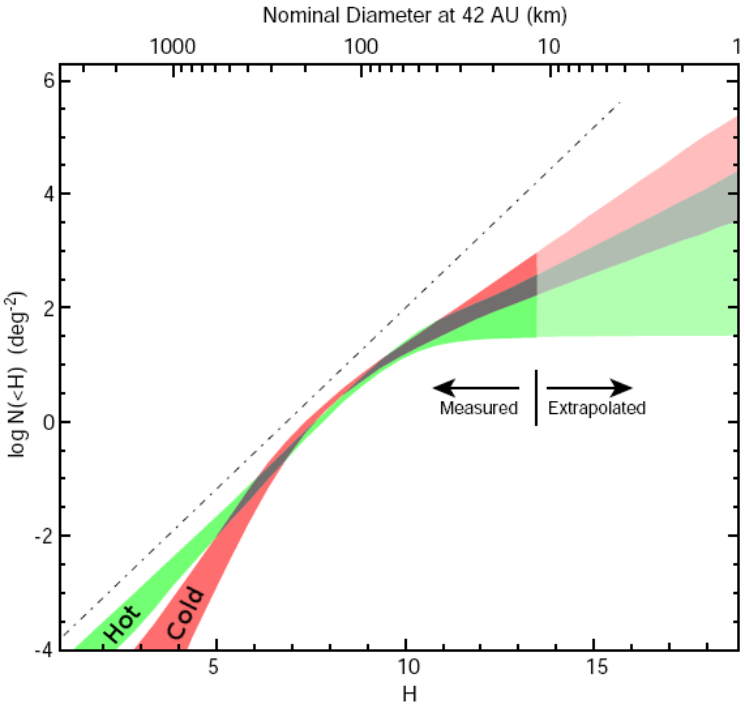

Figure 1.6: H and size distribution in the Kuiper belt at 42 AU (albedo of 4%), adapted of Bernstein et al. (2004) by Morbidelli (2005).

infrequent that 100 km objects cannot be built by paired accretion of the current population over the age of the Solar System. Due to the high eccentricities and inclinations of the KBOs (leading to high velocity encounters) the collisions that occurred were probably erosive instead of accretional. This suggests that the primordial Kuiper belt was both more massive and dynamically colder than the present one, so that, more collisions but gentler one, took place, leading to the accretion of small planetesimals.

1.2.3 *Oort Cloud.*

New comet

A NEW COMET is the one that initially has a semi-major axis, a, $\sim 10^4$ AU and that passes through the giant planets region, phenomenon that either decreases its semi-major axis one order of magnitude or changes its orbit to a hyperbolic. It is thought that the Oort cloud is a population of planetesimals from where the new comets came from. This hypothesis was proposed by Oort (1950) given the relative large quantity of LPCs[13] observed with $1/a \lesssim 10^{-4}$ in Figure 1.7 (Wiegert

13 The LPCs are those comets that have a period: $P > 200$ y. While the short period comets (SPCs) are those with $P < 200$ y.

& Tremaine, 1999). Oort's idea suggested that this region was a reservoir of long period comets with an quasi-spherical symmetry given the isotropic distribution of the orbital elements: inclination, i, argument of perigee, ω, and longitude of the ascending node, ω.

The gravitational force of the Sun over the Oort cloud objects (OCOs) (with $a \gtrsim 10^4$ AU) is not so strong as in the planetary region and the dynamics of these objects is been affected by the gravitational field of the Galaxy (galactic tide), the passing stars and the giant molecular clouds (GMCs). The galactic tide is mostly from the disc (the z component if we think it in cylindrical coordinates, which would be perpendicular to the galactic plane) (Heisler & Tremaine, 1986).

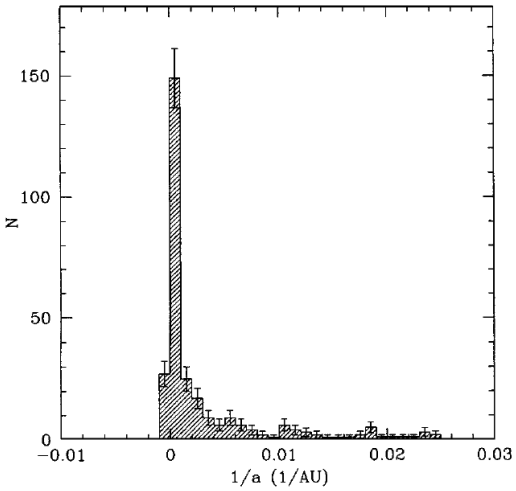

Figure 1.7: Distribution of LPCs as a function of the inverse of the semi-major axis. Now days we know the spike of this distribution as the OORT SPIKE. (Image taken from: Wiegert & Tremaine, 1999)

The high inclination OCOs with respect to the galactic plane, $\tilde{\imath}$, are removed of the Oort cloud under the effect of galactic tide by incrementing its eccentricity, e, and therefore decreasing its perihelion ($q = 10 \rightarrow 3$ AU) [14], q, becoming a PLANET-CROSSER comet. If these change in perihelion is realized in less than the corresponding orbital period, P, the object becomes in a new comet. The planets, specially the giant ones, additionally cause that these "crossers" change their a to lower values and leave to belong to the Oort cloud. This depletion of objects with high $\tilde{\imath}$ is somehow counteracted by the gravitational effect of passing stars or the GMCs, given that randomize the distribution of OCOs.

Simulations made by Wiegert & Tremaine (1999), reproduce the Oort peak in Figure 1.7 as shown in Figure 1.8. There is a significant drop in the distribution $1/a \sim 5 \times 10^{-5}$ related to the Jupiter-barrier which does not allow to the comets to reach the inner Solar System and instead of that have encounters with Jupiter or

14 The perihelion is given by:

$$q = a(1 - e)$$

Saturn, being more likely to get ejected from the Solar System. The new comets we can observe come, apparently, from $a > 20000$ AU, in the other hand, the information we know about the OCOs with $a < 20000$ AU is derived from the formation models of the Oort cloud.

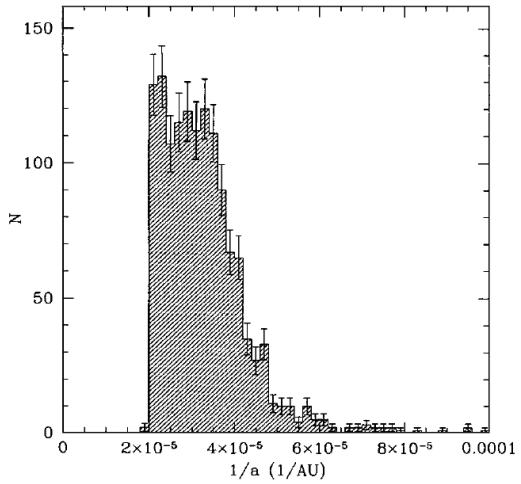

Figure 1.8: Distribution of $1/a$ of the comets at their first appearance ($q < 3$ AU) from the Oort cloud. (Image taken from: Wiegert & Tremaine, 1999)

The Oort cloud is thought to be formed by objects that were scattered from the planetary disk about 4.5 Gyr ago, this population have semi-major axes ranging between 1000 AU $< a <$ 100,000 AU. Models suggest that these objects were formed in the region of the giant planets ($\sim 4 - 40$ AU) and were perturbed by these to orbits with larger semi-major axes but with relatively unchanged perihelia. The influence of the galactic tide over this population became more important for those objects with $a \sim 10000$ AU and this modified their orbits within a time $< P$. For some of these, the eccentricity decreased in such way that the perihelion increased and were released from the planetary influence and from future scatterings (Kuiper, 1951b).

Dones et al. (2004) simulated the previous scenario, considering a planetesimals initially distributed inside the zone $a = 4 - 40$ AU and with low eccentricities and inclination. Also took into account the action of the planets over the planetesimals, the both galactic tides (disc and radial) and the transit of stars (but not the migration of the planets). At first, the action of the galactic tide is periodic over the perihelion of the particles, until a star passes nearby which brakes the periodicity, and the perihelia does not return to its origin value anymore.

The objects that are affected by the gravity of Jupiter and Saturn where expelled from the Solar System (as previously said), while those influenced by a distant interaction with Saturn are moved to further semi-major axes and faster than the interactions with Neptune.

The simulations of Dones et al. (2004) resulted on the final conservation of 5-9 % and 2% of the planetesimals that were initially neighbors of Uranus-Neptune and

Jupiter-Saturn respectively. As it can be seen in Figure 1.9, the outer Oort cloud ($a > 20000$ AU) was formed faster than the inner part, but also eroded quickly given the weak force of attraction from the Sun that these objects experience.

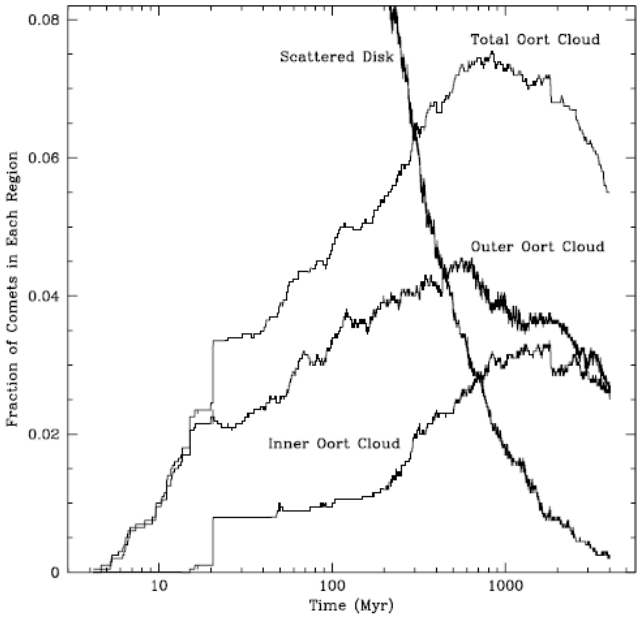

Figure 1.9: Results of Dones et al. (2004) simulations, shows that the outer Oort cloud formed faster than de inner part. (Image taken from: Dones et al., 2004, Fig. 11)

1.3 IMPORTANCE OF THE STUDY OF TNOS.

TNOs bear the marks of the accretion and evolution processes that shaped the current outer Solar System, in particular, provide evidence about what were the Physical processes that occurred there. If we want to understand the evolution of the Solar System, particularly in the outer region, we need to know the total mass of this population of objects even though it may be insignificant with respect to that of the planets at present.

Two characteristics of the TNO population are crucial to reveal the history of the Solar System: the size and orbital distribution. Although these two features are very important, there are also others, such as their physical properties, that provide information on the physical and chemical processes in the outer proto-planetary disk.

The determination of the size and spatial distribution of TNOs has been difficult, as explained in detail in Section 2.1, due to their low brightness and the complications associated with tracking them for several months to determine their orbit, among other things. One example of the intrinsic slow orbit motion would be that of Pluto, at $a \simeq 40$ AU, which has moved only $\sim 45\%$ of its orbit around the Sun since its discovery in 1930 (Barucci et al., 2008a).

Today, the uncertainty in the size distribution of TNOs prevents a precise determination of the total mass of this population. The mass estimation ranges from hundredths to tenths of Earth mass (Barucci et al., 2008a). Specifically, great uncertainties remain in the size distribution and total mass of the smaller objects of the TNO population, those with $D \lesssim 10$ km. Only weak upper bounds exist for this, more numerous class of objects. To solve this important piece of the Solar System formation puzzle, is the objective of the TAOS project.

2

Detection of Transneptunian Objects.

Initial surveys of the Kuiper belt were conducted with the assumption that objects discovered beyond Pluto would be undisturbed, pristine relics of the process of planet formation. Dynamically cold, circular and low-inclination orbits were expected.

The first object detected having an orbit completely transneptunian was reported by Dave Jewitt & Janet Luu in 1992. It was designated as 1922 QB$_1$ (Jewitt et al., 1992). At the time its orbit was completely indeterminate, the estimated distance from Earth ranged between 37 AU (for a parabolic orbit) to 59 AU (for a retrograde parabolic orbit). It was determined that if 1992 QB$_1$ was in a circular orbit then it was at 41 AU and had an inclination of 2° (Marsden, 1992).

Observations over an arc of four months made it possible to assure that 1992 QB$_1$ was the first discovery of an object beyond Neptune (Marsden, 1992). The availability of observations at opposition, the orbital shape and size helped to refine the estimated perihelion distance 41 AU and mean distance 44 AU. The discovery was described in detail by Jewitt & Luu (1993), the object is now numbered as 15760 in the IAU Minor Planet Center catalog.

1993 FW, with similar orbit (perihelion and mean distances 42 AU and 44 AU, inclination 8°) was reported by Luu et al. (1993). Four more discoveries were made in 1993, 1993 RO and 1993 RP by Jewitt et al. (1993a,b), and, 1993 SB and 1993 SC by Williams et al. (1993); the four of them with orbits much closer to Neptune (semi-major axis of 32 - 36 AU).

So far 1169 transneptunian objects and 439 Centaurs and SDOs have been detected, as reported by the Minor-Planet-Center (2012, Minor Planet Center)[1]. Its detection have been mainly done by direct observation methods, both space and ground-based telescopes.

From the previous chapter, we know that the current number of observed objects beyond Neptune does not agree with the number of objects expected to exist. This can be explained by an observational bias and/or because the models proposed

1 Up to date May 28, 2013 (http://www.minorplanetcenter.net).

so far do not reproduce fully or properly the mechanisms that gave origin to the small bodies in the Solar System.

The question then becomes, how much are we missing by observational and technological limitations? and, how well are we modeling reality? There are ways to estimate the effects of observational bias on the detection and counting of small bodies. It is necessary to know what is involved in this bias, i. e., how it originates (Section 2.1).

2.1 BIASES IN THE OBSERVED ORBIT DISTRIBUTION.

The determination of the orbit distribution of transneptunian objects is complex, mainly by biases in the detection and orbit determination for individual objects. Kavelaars et al. (2008) examine the most important of these biases, below described, that are present in any survey of KBOs and other TNOs. The latter reference conclude that the flux, pointing, and detection biases reflect an intrinsic problem of observing Solar System objects and empathizes that the ephemeris bias can be reduced by a planned observing program.

2.1.1 *Flux bias.*

Kuiper belt objects are discovered in the optical via reflected sunlight, so that the radiation flux from an object with radius R observed on Earth scales as $F \propto 1/\Delta^2$. The geometry of the problem is shown in Figure 2.1. We know that the flux in function of the distance from the source, r, is given by:

$$F = \frac{L}{4\pi r^2}$$

considering that the object has a cross section of $\sigma = \pi R^2$ and that $L = L_\odot$, then the luminosity on the object is:

$$L_{in} = \sigma F = \frac{L_\odot}{4}\frac{R^2}{r^2}$$

The reflected radiation, in first approach, is isotropic and reduced by a factor A (Bond albedo [2]), then the luminosity is $L_{out} = A\, L_{in}$, which flux observed from Earth would be:

$$F = \frac{L_{out}}{4\pi\Delta^2} \propto \frac{D^2}{\Delta^2 r^2} \tag{2.1}$$

2 Bond albedo: ratio of emergent flux to the incident flux ($0 < A < 1$). Only part of the luminosity is reflected, the rest is absorbed and converted into heat.

where D is the object's diameter and Δ is the distance between Earth and the KBO. It is considered that $r \approx \Delta$, giving as result an observed flux that depends on the distance to the object as $F \propto 1/\Delta^4$.

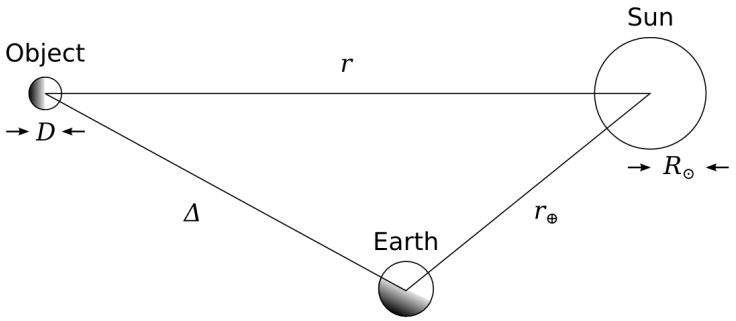

Figure 2.1: Geometry and symbols used in the flux calculation, observed from Earth, of the reflected solar light of a distant object.

The strong dependence of the observed brightness on the KBOs diameter and distance implies that small or distant objects are very difficult to observe. There is a need of stronger information about TNOs with $D < 10$ km and greater knowledge of objects at $\Delta > 50$ UA, as can be inferred from Figure 2.3, where the TNOs discovered up to date are plotted in function of their distance to Earth, Δ, and size, D.

2.1.2 *Pointing bias.*

Depends on the ecliptic latitude and longitude of the survey in such a way that given these two parameters would improve the fraction of detection of certain orbital class of TNO, evidently if a survey sampling in the vicinity of the ecliptic plane is more efficient detecting low inclination objects than high inclination ones.

2.1.3 *Ephemeris bias.*

While the survey for Solar System objects is done, the initial detection, the discovery, provides a first estimate of the orbital parameters of the body. Depending on its semi-major axis, the observational arc (related to the passed time since the first observation) could provide information robust enough to verify the object's orbit, in this way, it could be observed again later. E. g., the orbit of the asteroid-belt objects could be corrected with an observational arc of a week.

Contrary to the main asteroid belt, for distant objects as the KBOs, an arc of a week can at most be used to estimate the current distance and the orbital inclination to within 10 - 30% of reliability. Strong assumptions about the orbit have to be made in order to predict the later positions of any TNOs, the most common one is taking as an approximation the orbit is circular. This assumption, although (usually) incorrect, is accurate up-to ~ 60 arcsec a few months after discovery (Kavelaars et al., 2008).

If the recently discovered KBO is not observed again within a few months and the assumptions made do not match with the real orbital parameters, then the respective object will be lost together with the orbital parameter space it represented. This leaking of objects is what is known as EPHEMERIS BIAS. Given the assumptions made, the ephemeris bias keeps the observed orbital distribution with parameters like those of the assumed distribution instead of the real one.

A simple approach, as Kavelaars et al. (2008) suggested, to eliminate ephemeris bias is to follow the targets more frequently during the discovery opposition and to avoid targeted followup observation in favor of repeatedly observing the same large area of sky. The slow motion of KBOs ensures that they can be re-observed within a few degrees of their discovery location over the course of many months and even years.

2.1.4 *Detection bias.*

Observational surveys for KBOs (as discussed in Section 2.2) proceed via comparing images or comparing source catalogs constructed at different epochs. The time between epochs is kept short enough (~ 1 h) to minimize the possible confusion of a KBO with an asteroid. At 75 AU, the Kuiper belt objects move at ~ 2 arcsec per hour. It is not surprising that objects beyond 75 AU are rarely found, given that, they have even smaller sky motions and their detection is more problematic (Kavelaars et al., 2008).

Given the flux, pointing, ephemeris, and detection biases, it is no wonder that 500-m-diameter objects on high inclination orbit with $q > 50$ AU are rarely detected.

2.2 DIRECT OBSERVATION METHODS OF TNOS.

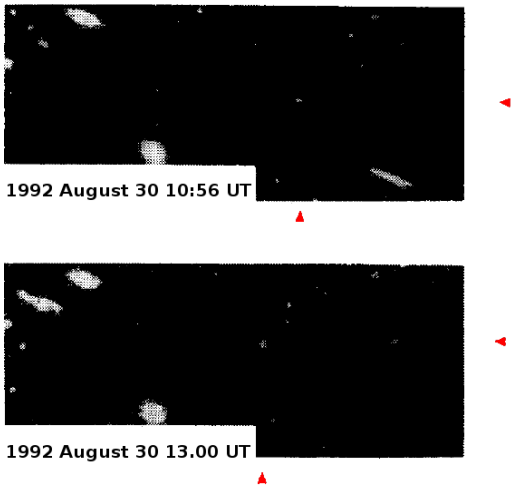

Figure 2.2: Discovery of 1992 QB_1 (marked with arrows), Jewitt & Luu (taken from 1993, Fig. 1). The elongated object to the lower right in the top image is a main-belt asteroid: it appears in the top left of the bottom image and demonstrates the slow motion of 1992 QB_1. The field shown is ~ 90 arcsec in width.

The first discovery, after Pluto's, of a TNO shows how the direct observation of this kind of objects is done. The small-bodies in the outer Solar System are considered by their motion as slowly moving objects (SMOs), i. e., it is expected that objects with large semi-mayor axis have longer periods, and consequently a smaller orbital velocity[3]. Most of the already known TNOs were discovered by direct observation in different surveys, as partially summarized in Table 2.1 (Kavelaars et al., 2008).

A deep-imaging survey of the vicinity of the ecliptic was carried out by Jewitt & Luu (1993), in which they discovered an SMO whose assigned name was 1992 QR_1. The survey consisted in obtaining a set of images per field, with a long total time-base (2 or more hours and the expected arc velocity was $\sim 1-2''/h$). In this way, the general method to detect a SMO is to take more than 2 images from the same field of stars with a difference of timebase of more than 2 hours and then analyze them by blinking the images among them to detect any relative movement.

The image limiting magnitude of Jewitt & Luu (1993) was $m_R \sim 25$ covering (at that moment) 0.7 square degrees of imaging at this depth. Their observations where confined to the opposition direction, where the angular motion of distant objects is retrograde. The distance to 1992 QR_1 could be calculated given that at opposition, the apparent angular motion of the objects is due to the Earth's motion (parallactic angular motion), $\dot{\theta}$ [4], is given by $\dot{\theta} = 148\left[(1-R^{-0.5})/(R-1)\right]$ (Luu & Jewitt, 1988), where R (AU) is the object's heliocentric distance. Thus, a measurement of $\dot{\theta}$ yields R directly (circular orbits were assumed).

3 The objects, planets included, that belongs to the Solar System have a Keplerian velocity.
4 Given in arcseconds per hour.

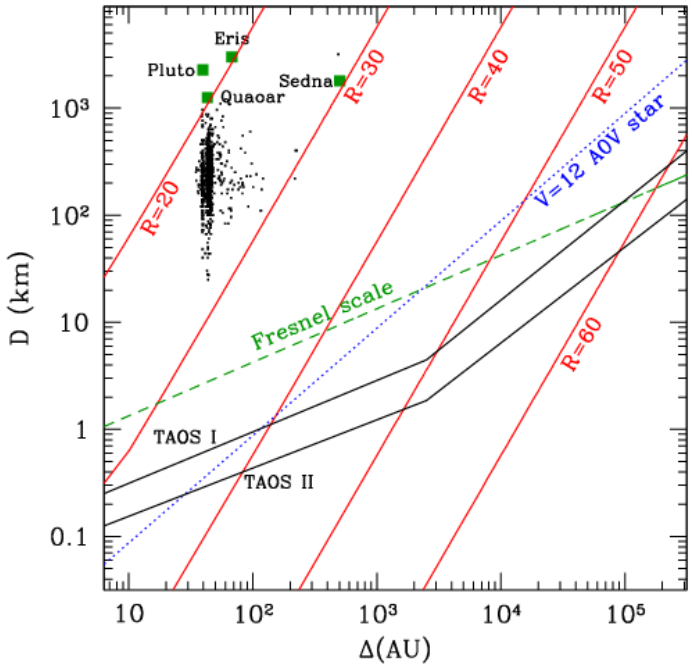

Figure 2.3: Diameter of object vs. semi-major axis. Known KBOs are plotted as dots, and some larger objects are shown as solid green squares. The division between geometric optics and strong diffraction is shown in green (Fresnel scale). Lines of constant R magnitude in reflected light are shown in red (albedo 0.04). The contour where projected size of a $R = 12$ A0V star is equal to the size of the object is also shown in blue, and the sensitivity limits on the TAOS I and TAOS II surveys are shown with the black lines.

Once an SMO is considered a TNO candidate it is necessary to follow-up its orbit in later observations to try to measure its distance to Earth, which is used to calculate the SMO orbital parameters (i. e., semi-mayor axis, a; eccentricity, e; inclination, i; orbital period, P; perihelion date, T; perihelion distance, q; aphelion distance, Q).

Usually, the albedo of the TNO is not known, which is one of the weaknesses of the direct methods of observation. Making reference to Section 2.1.1, we can conclude that is not possible to calculate the object size without knowing the albedo. The size of the objects is a datum that must be determined, especially to get more information about the size distribution of the objects on the transneptunian region.

The progress in the direct observation of TNOs is challenging as that the objects are small and the brightness in reflected sunlight declines $F \propto r^{-4}$ (see Equation 2.1). Presently, the occultation surveys are the only proposed method to detect objects that are fainter than $R \sim 30$. The objects seen in the direct surveys are larger than any of the observed short period comet, a census of TNOs with sizes compara-

ble to the known short period comets is an essential test of the theory of the origin for short period comets.

Figure 2.3 shows a plot of the TNOs already discovered as a function of their size, D, and their distance to Earth, Δ. This highlights the limitations of direct observation, restricted to a size of objects ranging from a few kilometers to hundreds of kilometers, and a maximum distance of 300 AU. Also shown is the relationship between the distance and size of the objects that results in diffraction effects being important (dashed green line). Stellar occultation surveys such as the TAOS I project and proposed TAOS II (lower limits in solid black lines) are in principle not affected by the distance and size, designed to exploit the natural diffraction effect on the observed light curve and thus will be able to obtain information on both, object size and its relative distance to the Earth.

SURVEY	AREA [DEG^2]	DEPTH [MAG]	DETEC.	SECURE	REFERENCE
CEPS	321	23.5 - 24.4	196	169	Petit et al. (2011)
DES	550	22	486	217	Elliot et al. (2005)
Caltech	19389	20.5	71	54	Trujillo and Brown (2003)*
Allen1	1.5	25.5	24	6	Allen et al. (2001)
KPNO-Large	164	21.1	4	4	Trujillo et al. (2001a)
CFH/12	0.31	25.93	17	2	Gladman et al. (2001)
CFHT	73	23.7	86	59	Trujillo et al. (2001b)
Spacewatch	1483.5	21.5	39	36	Larsen et al. (2001)
Baker-Nunn	1428	18.8	1	1	Sheppard et al. (2000)
JL Deep	0.3	26.3	6	1	Luu and Jewitt (1998)
G98a	0.35	24.6	1	1	Gladman et al. (1998)
G98b	0.049	25.6	4	1	Gladman et al. (1998)
JLT	51.5	23.4	13	12	Jewitt et al. (1998)
Pluto-Express	2.2	23.5	4	3	Trujillo and Jewitt (1998)
MKCT	3.9	24.2	14	10	Jewitt et al. (1996)
MKCT	4.4	23.2	3	1	Jewitt et al. (1996)
ITZ	0.7	23.5	2	2	Irwin et al. (1995)
MEAN MAGNITUDE DEPTH.	23.6 $\pm$ 2.2				

Table 2.1: List of TNOs surveys with secured detections. (Fragment of Table 1 of Kavelaars et al. (2008))

2.3 OCCULTATION METHOD.

The observation of stellar occultations by Solar System objects is an efficient method to study both the occulting object and the occulted star. This technique consists in recording (at high photometric sampling rate) of the stellar flux, waiting for an object that passes in front of the line-of-sight and blocks a brief time the light of the star. A general advantage of this technique is the high spatial resolution it reaches, allowing the detection of ~ 1 km objects, which would represent the discovery of material difficult to detect otherwise by ground-observations (Roques et al., 1987).

In any observation is important to know whether the phenomenon of diffraction is predominant. The diffraction is a function of the size of the obstructive object, D, the distance of the latter to the observer's plane, Δ, and the observing wavelength, λ, as the Fresnel number, N_F, reflects. The Fresnel number (Equation 2.2) is a dimensionless quantity that indicates whether the expected pattern is dominated by Fraunhofer (far-field) diffraction ($N_F \ll 1$), Fresnel (near-field) diffraction ($N_F \gtrsim 1$) or geometric optics ($N_F \gg 1$), it is defined as:

Fresnel number.

$$N_F \equiv \frac{\alpha^2}{\lambda \Delta} \tag{2.2}$$

where $\alpha = 0.5D$ is the radius of the obstruction. The Fresnel number for an object of size $D = 4$ km ($\alpha = 0.5D = 2$ km), at a distance $\Delta = 43$ AU from Earth and observed at $\lambda \approx 600$ is $N_F = 1.04$, which is in the Fresnel regimen, while an object of $D = 0.5$ km may be considered as being near the Fraunhofer regime, in contrast, and an object of $D = 30$ km is almost in the geometrical optics region.

Fresnel diffraction is the phenomena observed at a finite distance considering the Huygens-Fresnel principle. Huygens proposed that each point of a wave-front may be considered as the center of a secondary disturbance that results in spherical wavelets, the envelope of these wavelets is the wave-front at a later instant. Fresnel contributed with this principle by adding that these wavelets mutually interfere. The diffraction occurs when a wave is blocked by an obstacle and can occur for any wavelength, not only in the visible range. The Huygens-Fresnel principle leads to the Fresnel-Kirchhoff diffraction formula (Born & Wolf, 1980, p. 380) which approximates the complex amplitude of the diffracted wave-front by a surface $\mathcal{S}$, $a_{\mathcal{S}}(P)$, as:

Huygens-Fresnel principle approximated by the Fresnel-Kirchhoff diffraction formula.

$$a_{\mathcal{S}}(P) = -\frac{i}{2\lambda} \frac{e^{ikr_0}}{r_0} \iint_W \frac{e^{iks}}{s} (1 + \cos\chi)\, d\mathcal{S} \tag{2.3}$$

where r_0 is the radius of curvature of the wave, s is the distance $\overline{QP}$, χ is the angle between r_0 and s (see Figure 2.4) and k is the wave number.

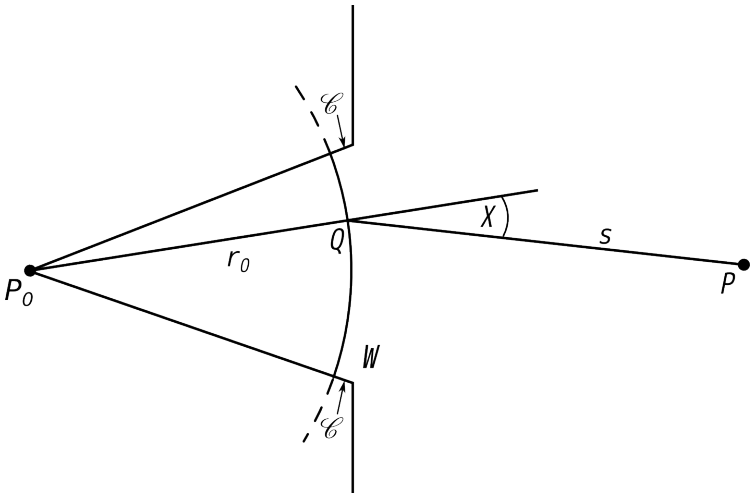

Figure 2.4: Illustration to understand the Huygens-Fresnel principle in terms of the Fresnel-Kirchhoff diffraction formula. W is the wave-front section that goes through the aperture of radii α, r_0 is the wave-front curvature and s is the distance from Q to P (the observation point). When r_0 is large enough the contribution from $\mathcal{C}$ can be discarded and the wave-front is "more planar". (Image taken from: Born & Wolf, 1980, Fig. 8.4).

In 1987, Roques et al. developed a theoretical model from the Fresnel-Kirchhoff diffraction theory of occultation events caused by opaque elliptical disks. Also Roques et al. (1987), discusses the theoretical implications of the diffraction during the stellar occultations. The authors regarded the object as an opaque flat surface, $\mathcal{S}$, with a circular cross section of diameter D, located at a distance Δ from the observer. The plane of the observer (denoted by xy) is parallel to the object's plane ($\xi\eta$) as shown in Figure 2.5. The incident plane wave-front of monochromatic wavelength λ is obstructed by $\mathcal{S}$, which results in a diffracted wave-front described by Equation 2.3. In this study the typical value of size for the obstructive body (TNOs) is $D < 10$ km, which is many orders of magnitude larger than the observed wavelength ($\lambda \approx 600$ nm) and smaller than the distance from the obstruction to the observer ($\Delta \geqslant 30$ AU).

Considering the geometry of an occultation event as proposed by Roques et al. (1987) (Figure 2.5) and replacing $r_0 = -D$, $s = \sqrt{r^2 + \rho^2 - 2r\rho\cos(\phi - \theta) + D^2}$ and $k = 2\pi/\lambda$ into Equation 2.3, were both r_0 and s are in polar coordinates [5], we

5 In object's plane (ρ, ϕ).
In observer's plane: (r, θ).

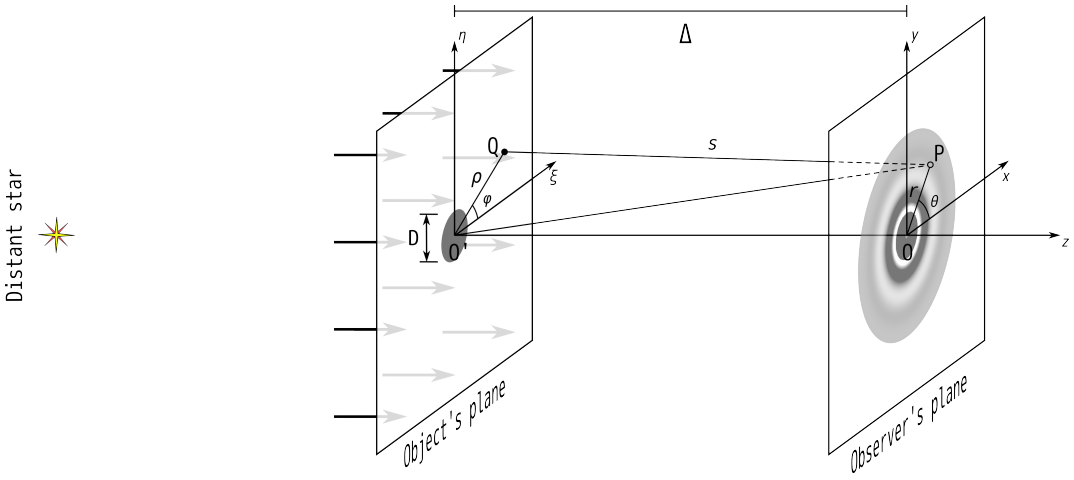

Figure 2.5: Geometry of an occultation event: A plane wave-front of light, from a distant star, is blocked by an opaque flat obstacle of surface $\mathcal{S}$, and size D. The object's plane $(\xi\eta)$ is located at a distance Δ from observer's plane (xy), who is placed at point P. The angle between the normal of the wave-front and s is χ, where s is $\overline{QP}$.

obtain the Eq. (1) of Roques et al. which in polar coordinates (Equation 2.4), can be written as:

$$a_{\mathcal{S}}(P) = -N\,\frac{e^{-i\frac{2\pi}{\lambda}D}}{D}\iint_{\xi\eta-\mathcal{S}}\frac{e^{\left[i\frac{2\pi}{\lambda}\sqrt{r^2+\rho^2-2r\rho\cos(\phi-\theta)+D^2}\right]}}{\sqrt{r^2+\rho^2-2r\rho\cos(\phi-\theta)+D^2}}\,(1+\cos\chi)\,\rho\,d\rho\,d\phi \tag{2.4}$$

It has to be noticed that, strictly, the in Roques et al. (1987) θ[6] and our χ are not equal, but as it will be demonstrated later, the multiplying term $(1+\cos\chi)$ vanishes given the dimensions of the system studied.

Equation 2.4 is the complex diffracted amplitude on which the results of Roques et al. (1987) are based. These authors take into consideration that in our problem of interest there is an obstruction rather than an opening, as usually done in textbooks. Therefore, the integration of Equation 2.3 must be carried out on the complement $(\xi\eta - \mathcal{S})$ of what would be an opening the same size as the obstruction. That is why the authors included the complex normalizing parameter N, that ensures $a_{\mathcal{S}}(P) = 1$ when there is no obstruction $(N = -i/2\lambda)$. As mentioned before, $\mathcal{S}$, $\rho \ll D$, which implies that $\sqrt{r^2+\rho^2-2r\rho\cos(\phi-\theta)+D^2} - D \approx r^2+\rho^2-$

6 The angle between the line-of-sight ($\overline{QP}$) and the line $\overline{O'P}$.

$2r\rho\cos(\phi-\theta)$ in the exponential, $(r^2+\rho^2-2r\rho\cos(\phi-\theta)+D^2)^{-1/2}\approx D^{-1}$ and $\chi\sim 0$, consequently $\cos\chi\approx 1$ and $1+\cos\chi\approx 2$, leading to:

$$a_S \approx (P)1 + \frac{i\,e^{i\frac{\pi}{\lambda D}r^2}}{\lambda D^2}\int_0^{\alpha} e^{i\frac{\pi}{\lambda D}\rho^2}\int_0^{2\pi} e^{-i\frac{2\pi}{\lambda D}r\rho\cos(\phi-\theta)}\,d\phi\,\rho d\rho \tag{2.5}$$

To carry out the integration over ϕ, we use the definition of J_n, the n-th order Bessel function, given by:

$$J_n(z) = \frac{i^{-n}}{2\pi}\int_0^{2\pi} e^{-in\phi}e^{iz\cos(\phi)}\,d\phi$$

for the case $n = 0$. Finally, the property $J_n(-z) = (-1)^n J_n(z)$, is also used to obtain Eq. (9) of Roques et al. (1987):

$$a_\alpha(P) = 1 + \frac{2\pi i\,e^{i\frac{\pi}{\lambda D}r^2}}{\lambda D^2}\int_0^{\alpha}\rho\,J_0\left(\frac{2\pi}{\lambda D}r\rho\right)e^{i\frac{\pi}{\lambda D}\rho^2}\,d\rho \tag{2.6}$$

According to Roques et al. (1987), the solution to Equation 2.6 can be expressed in terms of the Lommel functions [7], so that the occultation diffraction pattern of a distant star by a foreground circular cross section is described by U_n, which is redefined as:

$$U_n(\alpha', r') = \sum_{k=0}^{\infty}(-1)^k\left(\frac{\alpha'}{r'}\right)^{n+2k} J_{n+2k}(\pi\alpha' r') \tag{2.7}$$

where $\alpha/F = \alpha'$ and $r/F = r'$ are dimensionless quantities, where F is a normalization factor, denominated the FRESNEL SCALE (perhaps by its resemblance to N_F) defined as:

Fresnel scale.

$$F \equiv \sqrt{\frac{\lambda\Delta}{2}} \qquad \text{In Nihei et al. (2007) } \Delta = a \text{ is assumed.} \tag{2.8}$$

Note that in Equation 2.7, a change in the order of the variables ($(\alpha', r') \rightarrow (r', \alpha')$) in the arguments of U_n, results in the other function Lommel, V_n. Comparing this definition with that given by Born & Wolf (1980) we conclude that the second argument of $U_n(u, v)$ and $V_n(u, v)$ is equivalent to:

$$v = \frac{2\pi}{\lambda}\left(\frac{\alpha}{\Delta}\right)r = \pi\alpha' r'$$

7 As explained in Born & Wolf (1980, p. 435), Lommel was the first to express the Huygens-Fresnel principle in terms of a convergent series of Bessel functions of first order, J_n. The Lommel functions commonly designated, U_n and V_n, have several representations. The one used in this work is the same used by Born & Wolf (1980, p. 438):

$$U_n(u, v) = \sum_{m=0}^{\infty}(-1)^m\left(\frac{u}{v}\right)^{n+2m} J_{n+2m}(v)$$

$$V_n(u, v) = \sum_{m=0}^{\infty}(-1)^m\left(\frac{v}{u}\right)^{n+2m} J_{n+2m}(v)$$

The use of either of these depends in the convergence of the ratio u/v.

Integrating Equation 2.6 by parts (with r and α normalized to F) and using the following recurrence relations (see Born & Wolf, 1980, pp. 437-439):

$$\frac{d}{dx}\left[x^{-n}\,J_n(x)\right] = -x^{-n}\,J_{n+1}(x) \qquad \text{when } r' \leqslant \alpha'$$
$$\frac{d}{dx}\left[x^{n+1}\,J_{n+1}(x)\right] = x^{n+1}\,J_n(x) \qquad \text{when } r' \geqslant \alpha'$$

the complex diffracted amplitude in terms of the Lommel function Equation 2.7 is obtained (Equation 2.9). Two regions where evaluated separately depending on the convergence of $a_{\alpha'}(r')$, otherwise the evaluation of $a_{\alpha'}$ would be indeterminate, although both are equivalent (Born & Wolf, 1980). The one that is INSIDE the shadow of the object converges when $\alpha' \geqslant r'$, and the one OUTSIDE the shadow converges when $r' \to \infty$.

$$a_{\alpha'}(r') = \begin{cases} e^{i\pi(r'^2+\alpha'^2)/2}\left[U_0(r',\alpha') - iU_1(r',\alpha')\right] & r' \leqslant \alpha' \\ 1 + e^{i\pi(r'^2+\alpha'^2)/2}\left[U_2(\alpha',r') + iU_1(\alpha',r')\right] & r' \geqslant \alpha' \end{cases} \tag{2.9}$$

Intensity of a observed star considering an occultation by an object of radius α'.

The measured intensity, $I_{\alpha'}(r')$, is given by the modulus of $a_{\alpha'}(r')$ [8] which is also divided into two regions:

$$I_{\alpha'}(r') = \begin{cases} U_0^2(r',\alpha') + U_1^2(r',\alpha') & r' \leqslant \alpha' \\ 1 + U_1^2(\alpha',r') + U_2^2(\alpha',r') & \\ -2U_1(\alpha',r')\sin\frac{\pi}{2}\left(\alpha'^2 + r'^2\right) & r' \geqslant \alpha' \\ +2U_2(\alpha',r')\cos\frac{\pi}{2}\left(\alpha'^2 + r'^2\right) & \end{cases} \tag{2.10}$$

The amplitude and intensity of the diffraction pattern for the occultation depend solely on the obstacle radii in units of the Fresnel scale, α'.

Recently, Nihei et al. (2007) worked on the simulation of stellar occultations, accounting for diffraction effects, finite source size, finite bandwidths, stellar spectra, sampling frequency, and signal-to-noise ratio. The diffraction intensity (Equation 2.10) estimated by Roques et al. (1987) is used in Nihei's work, the notation used therein is $\rho = \alpha'$, $\eta = r'$, $a = \Delta$ and $r = \alpha$. The theoretical occultation pattern for $\rho = 1$ projected on Earth is shown in Figure 2.7a,also in the same figure, they show four trajectories through the occultation pattern at four different values of the impact parameter b, given in terms of the diameter of the first Airy ring, which

8 $I_{\alpha'} = |a_{\alpha'}|^2$

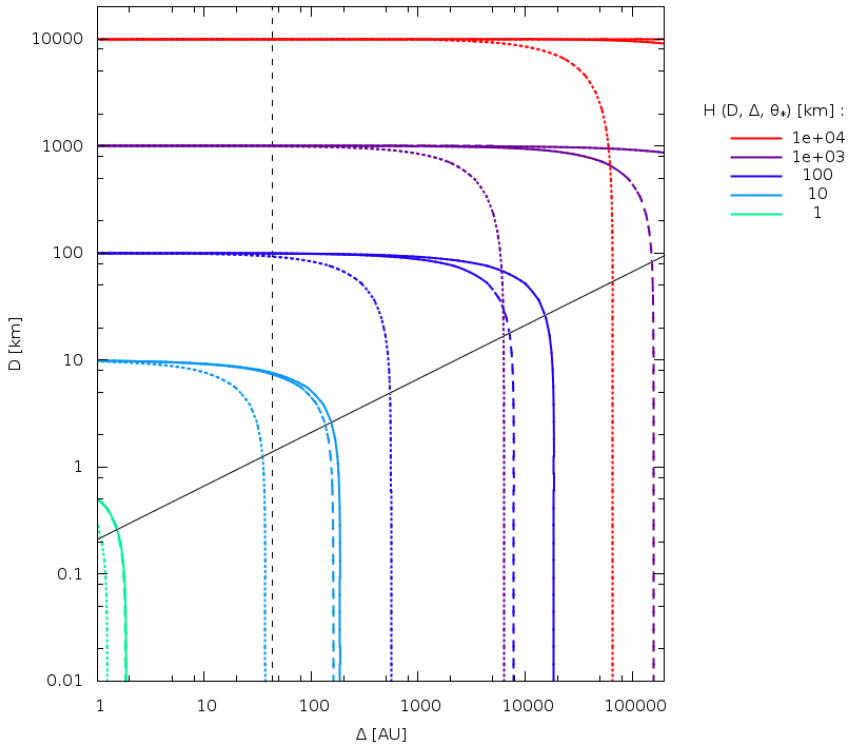

Figure 2.6: Contours of event cross section, $H(D, \Delta, \theta_*)$ as given by Equation 2.11c. Equal values of H have the same color, while the different line types denote diverse θ_* values (the solid line is $\theta_* = 0$, the long-dashed line is $\theta_* = 3 \times 10^{-11}$ and the short-dashed line is $\theta_* = 10^{-9}$). Also shown is the Fresnel scale, F, (black solid line) as a function of Δ for $\lambda = 600$ nm. The black vertical dashed line indicates $\Delta = 43$ AU.

Nihei et al. (2007) denominated Ω (defined by Equation 2.11a), which is used in the figures below. In the notation of Zhang et al. (2008) we have:

Event cross section or Diameter of the first Airy ring.

$$\Omega_{\text{Nihei}} \approx 2\left[\left(\sqrt{3}\right)^{3/2} + \rho^{3/2}\right]^{2/3} \quad \Leftarrow \text{Dimensionless.} \tag{2.11a}$$

$$W_{\text{Nihei}} \approx 2\left[\left(\sqrt{3}F\right)^{3/2} + r^{3/2}\right]^{2/3} \tag{2.11b}$$

$$H(D, \Delta, \theta_*) = \left[\left(2\sqrt{3}F\right)^{3/2} + D^{3/2}\right]^{2/3} + \theta_*\Delta \tag{2.11c}$$

We can observe in Figure 2.7a that the "shadow" of an object crossing in front of a source with a finite impact parameter, b, or out of the optical axis by a factor b, leads to several possible intensity curves for a given occultation pattern. For $b \geqslant 0.5\,\Omega$ the occultation depth is small, and the events are very difficult to detect, thus it is possible to define an OCCULTATION EVENT as an object crossing the

Occultation event

line of sight to a star with an impact parameter $b \leqslant 0.5\,\Omega$. This does not mean that there will not be events with $b > 0.5\Omega$, but we will not be able to determine whether there is or not an occultation event such values of b.

Empirical occultation depth.

The occultation depth, Δ_{Nihei}, as defined by Nihei et al. (2007), is the maximum flux (or intensity) drop of an occultation pattern (Equation 2.12), as shown in Figure 2.7b.

$$\Delta_{Nihei} = \left[1 + \left(3\rho^2\right)^{-3/2}\right]^{-2/3} \tag{2.12}$$

As Figure 2.7 demonstrates, the occultation light curves exhibit a wide range of morphologies. This happens also with the occultation pattern, which depend on the stellar type and brightness, as well as the distance and size of the occulting object, as illustrated in Figure 2.9a. A source angular size, θ_*, can be inferred from the stellar type and brightness. In the object plane $r_* = \theta_* \Delta$ (Figure 2.8) relative to the Fresnel scale, $\rho_* = r_*/F$. The morphologies could be categorized into five regions: A, B, C, D and E (Figure 2.9a). The regions A and D lie in the range where the projected source radius $\rho_* < 1$ ($a \lesssim 2000$ AU). The regions B and C, in the opposite, lie in the distance range where $\rho_* > 1$. Region E lies near the critical value of ρ_*, $\rho_* \sim 1$.

When $\rho \gg 1$, the occultation pattern for a point source can be approximated by a geometric shadow (Nihei et al., 2007, Fig. 3). Following this, the A and B regions represent the areas where the parameters result in geometric occultation patterns. The difference between the two regions is the source size ρ_* value. In region B, $\rho_* \gtrsim 1$, notice that $\rho_* \propto \Delta$, the details of the diffraction pattern are removed given a significant smoothing by the stellar source disk, this includes the Poisson spot[9]. In contrast in region A, the diffraction features remain pattern when $\rho_* \lesssim 1$.

Occultation patterns with parameters as those in regions C and D (Figure 2.9a), are within the diffraction regimes ($\rho \lesssim 1$). Both regions exhibit less profound occultation depths, the occultation will display a level of broadening and smoothing depending on the source size ρ_*. The Fresnel scale is smaller than the projected source size in region C, and therefore the occultation pattern will be dominated by Fresnel diffraction, these events are wide but with superficial depths. Occultation patterns in region D tend to accomplish with the condition of Fraunhofer diffraction ($r_* \ll F$). Finally, patterns in region E, where $\rho_* \sim 1$ and $\rho \sim 1$, show a significant depth without complete extinction of the source and are devoid of significant diffraction features.

9 Poisson spot is a bright point that appears at the center of a circular object's shadow due to Fresnel diffraction, it has the same intensity as if no obstruction were present.

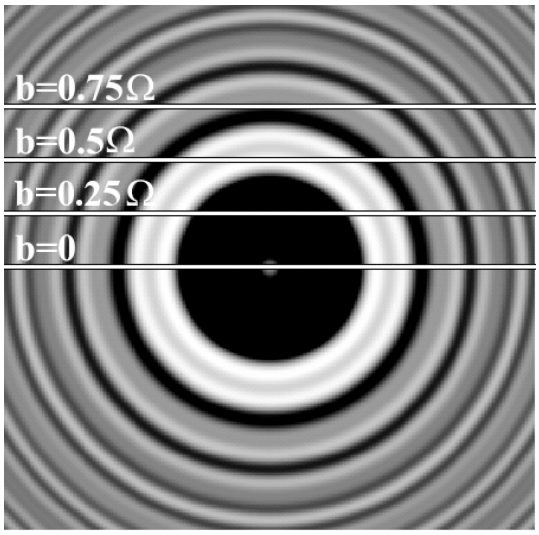

(a)

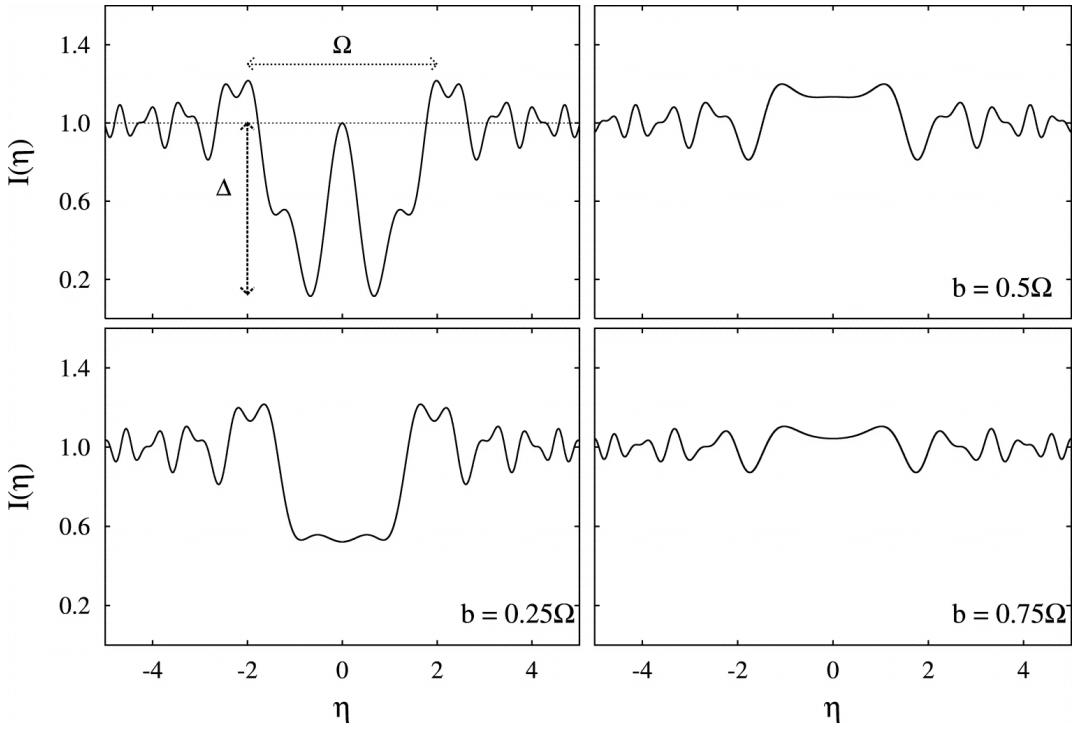

(b)

Figure 2.7: In (a), we shown the diffraction pattern projected on the observer's plane for $\rho = 1$. The impact parameter (white horizontal lines), b, is given in terms of Ω_{Nihei}. (b) The corresponding intensity profiles of the different impact parameter sections in (a). (Images taken from Nihei et al. (2007, Fig. 1 & 2))

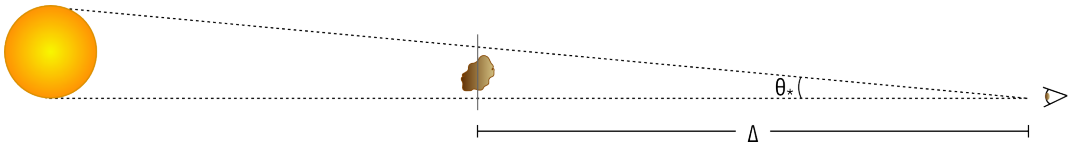

Figure 2.8: Projected size of the star in the plane of the studied object.

Diffraction effects dilute the depth of the occultation events, but also sets a minimum event width, given by $2\sqrt{3\,F}$ (Nihei et al., 2007). As described before, the diffraction effects on the light curve depend on the size and distance of the occulting objects, if the produced fringes can be measured, Δ and D can be estimated. Hence, the occultation method of observation can be helpful in the estimation of the spatial and size distribution of TNOs.

2.4 TAOS-I PROJECT.

TAOS is the acronym for Taiwan American Occultation Survey as the first phase of this project was called. Its objective, like the name suggests, is to search for occultations of distant stars by outer Solar System objects. The system was designed to collect images at a high enough cadence (5 Hz) to detect occultation events, to follow enough stars ($\sim$ 1000) for a significant event rate, and to give a low false positive rate. To accomplish its purpose four robotic telescopes[10] where installed at Lu-Lin Mountain Observatory in the Yu Shan area of Taiwan. The site has a median seeing of 1.3" (arcsec), with $\sim$ 100 clear nights per year (Lehner et al., 2007).

The fast readout (high sampling rate) is achieved using what has been called shutterless zipper mode, which allows a 5 Hz sampling with at expense of a decreased signal-to-noise ratio (Lehner et al., 2006). The design goal was to be able to measure a rate of stellar occultations by KBOs of 1 per 1000 stars per year of observing time.

False detections could arise from any number of sources, such as birds, airplanes, instrument noise, and atmospheric scintillation. False positives from these sources are ruled out by requiring joint detection in an array of four independent tele-

10 Aperture of 50 cm.
Cassegrain focus at f/1.9.
Field of view of 3 square degrees.
Backside-illuminated Marconi CCD chip.

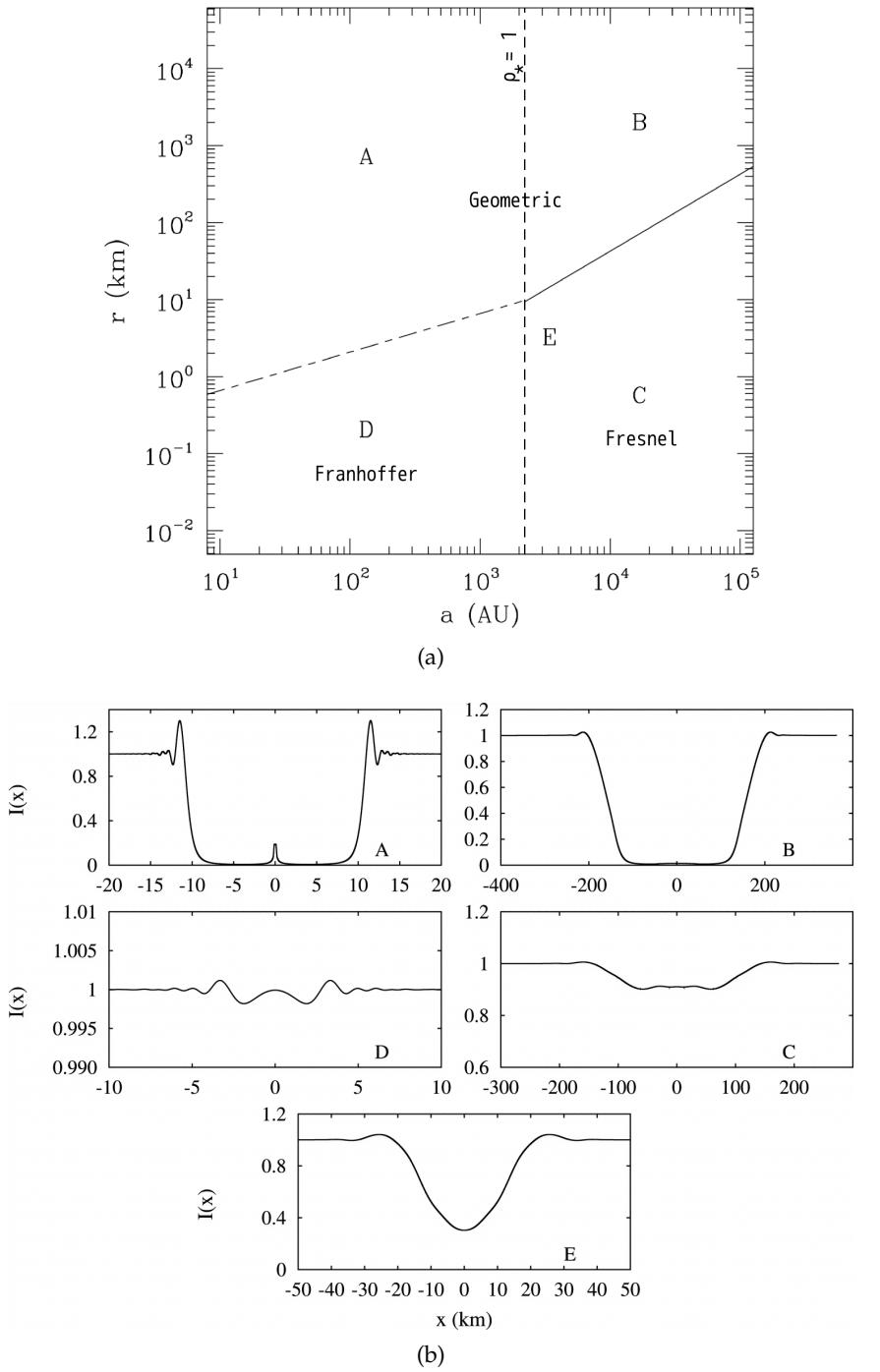

Figure 2.9: Characteristic curve shapes depend on stellar disk radius r_* and the Fresnel scale. (a) Summary of the resulting light curve classes for object radii r and distances $a \leftrightarrow \Delta$ passing in front of a $V = 12$ A0V star. (b) Example light curves for each of 5 classes in (a), labeled with its adequate region. (Images taken from Nihei et al. (2007, Fig. 12 & 13))

scopes. The telescopes have separations ranging from 6 meters to 60 meters.

There are two main limitations to this survey. First, the expected event rate is very low. Second, very title information on any object detected can be deduced from the available information in the lightcurves. This is mainly due to the low sampling rate which smooths-out the diffraction features in an occultation lightcurve, but even with high temporal sampling, this information is limited due to degeneracies in the lightcurve shape parameters of interest such as object size and distance.

Figure 2.10: Lulin Observatory panoramic view, location of the TAOS I Project.

There are several papers related to the results obtained by TAOS I. Zhang et al. (2008); Bianco et al. (2010); Zhang et al. (2013) presented the results from the first 2, 3.75 and 7 years of data of TAOS I, respectively, neither of them found any significant event, this allowed them to estimate an upper limit to the size distribution of KBOs with diameters between 0.5 km and 30 km. Wang et al. (2009) tried to find objects with Sedna-like orbits by the occultation method at distances between 100 and 1000 AU from the TAOS I, the authors did not detect any event, again, allowing them to set upper limits on the number density as function of size and distance of objects in Sedna-like objects. Among other results obtained of the TAOS I data are those related with the stellar variability (Kim et al., 2010) and close binary star resolved from occultation (Lin et al., 2009).

Recently, an important upgrade has been made to the TAOS I cameras, which will allow taking photometric measurements at a cadence of 10 Hz, twice the current capacity. The work described in this thesis was originally motivated by the necessity to take full advantage of this newly added capabilities.

2.4.1 *Rank statistics.*

The statistical analysis of the data in the TAOS project was done using rank statistics (Lehner et al., 2010), which will be reviewed briefly here. The goals of the

TAOS statistical analysis were to find as many events as possible, to minimize the false positive rate, and to provide a method to estimate the statistical significance of any candidate event.

The noise distribution is unknown for each of the lightcurves, additionally, some uncertainties are introduced in the flux measurements given the duration of the observations per field of stars ($\sim$ 1.5 h), time where there are changes in the atmospheric transparency and airmass. The TAOS team overcame these problems by assigning a rank to each flux in the lightcurves, this also helped to make a matching between the lightcurves of different telescopes without making any kind of calibration.

In statistics, the "ranking" is the transformation of data from a numeric value to its corresponding rank, e. g., consider the sequence of 6 numbers: 1.5, 45.4, 0.4, 63, 9.45 and 3, the rank will be: 2, 5, 1, 6, 4 and 3. The same idea is applied to time series (t_j) of flux measurements $f_1, ..., f_{N_p}$ that belong to a determined lightcurve of one of the TAOS telescopes. N_p is the total number of points in the lightcurve, as we can conclude from the previous example, the rank values, r_j, will range from 1 to N_p. The total number of points will depend on the total time that a star field is observed and the cadence used, considering a cadence of 10 Hz, the total number of points would be $N_p = 54000$.

Considering the simultaneous observation of T telescopes, as occurs in the TAOS project ($T = 3, 4$), the rank statistics has to be applied in each one, resulting in a set of T rank time series r_{ij}, where i denotes the telescope used. For each time point t_j, we have a RANK TUPLE r_{Tj}. *Rank tuple*

Fisher (1925) developed an statistical method which can test combined probability. It is mainly used when there is a collection of independent statistical tests pretending to reject the same null hypothesis. The Fisher's method involves the probability values ($p-values$ or $\mathbb{P}$) of each of the independent test, i, and combine them into a unique test using the formula:

$$\chi^2 = -2\sum_{i=1}^{k} \ln\left(\mathbb{P}_i\right)$$

which, making some algebra is equal to:

$$\chi^2 = -2\ln\left(\prod_{i=1}^{k} \mathbb{P}_i\right) \tag{2.13}$$

Each of the lightcurves obtained from the simultaneous observation of the T telescopes, constituting the TAOS I project, are considered independent studies to

reject the null hypothesis of no occultation. This allowed Lehner et al. (2010) use a statistical test based on Fisher's method where the $p-value$ of each measurement on the lightcurve is the ratio between the rank, r_{ij}, and the number of points.

Probability value ($p-value$) for the TAOS data.

$$\mathbb{P}(R \leqslant r_{ij}) = \frac{r_{ij}}{N_p} \tag{2.14}$$

The tuple of $p-values$ at time t_j is used to calculate a single test of significance, z_j. The product of $p-values$ is reduced to the product of the rank tuple, y_j, over the T telescopes:

Rank product statistics.

$$\begin{aligned} z_j &= -\ln\left(\prod_{i=1}^{T}\frac{r_{ij}}{N_p}\right) \\ &= -\ln\left(\frac{y_j}{N_p^T}\right) \end{aligned} \tag{2.15}$$

z_j is what Lehner et al. (2010) defines as the RANK PRODUCT STATISTICS which resembles to Equation 2.13 [11].

The probability distribution, $p(z_j)$, of z_j under the continuous interval $[0, 1]$ is a Γ distribution:

$$p(z_j) = \frac{1}{\Gamma(T)} z_j^{T-1} e^{-z_j}$$

However, the actual distribution of $p-values$ is not continuous, but discrete with an interval $\{1/N_p, 2/N_p, ..., 1\}$. According to Lehner et al. (2010), the rank product distribution is given by the function $K(n; T, N_p)$ (Equation 2.16), defined as

> the number of ways to get a product of n by multiplying T integers (number of telescopes) between 1 and N_p (number of points in the lightcurves).

11 Taking Equation 2.14 and realizing the product of probabilities:

$$\begin{aligned} \prod_{i=1}^{T}\mathbb{P} &= \prod_{i=1}^{T}\frac{r_{ij}}{N_p} = \frac{1}{N_p^T}\prod_{i=1}^{T} r_{ij} \\ &= \frac{1}{N_p^T} y_j \end{aligned}$$

which demonstrates that z_j (Equation 2.15) is similar to χ^2 (Equation 2.13), with the difference of a factor of 2.

The K function is independent of N_p if $n \leqslant N_p$ and is a result of combinatorics. The d_i numbers, in Equation 2.16, are the powers of the prime numbers, p_i, in which n can be decomposed and m is the total number of p_i [12].

$$K(n; T, N_P) = \prod_{i=1}^{m} \binom{d_i + T - 1}{T - 1} = \prod_{i=1}^{m} \frac{(d_i + T - 1)!}{(T-1)!\, d_i!} \tag{2.16}$$

The discrete probability distribution (Lehner et al., 2010), in terms of K and y, is:

$$p(y) = \frac{1}{N_p^T} K(y; T, N_p)$$

and the $p - value$ of any candidate event can be calculated as:

$$\mathbb{P}(Y \leqslant y) = \frac{1}{N_p^T} \sum_{j=1}^{y} K(j; T, N_p) \tag{2.17}$$

The difference between the continuous and discrete probability distribution can be observed in Figure 2.11, there is an evident discrepancy in the tail of both distributions. The discrete distribution is limited by the more significant rank product $y_j = 1$ where $z = 32.7$ for $T = 3$ and $z = 43.6$ for $T = 4$.

12 I. e.: $n = p_1^{d_1} \times p_2^{d_2} \times \cdots \times p_m^{d_m}$. E. g.: if we take $n = 18$, then: $18 = 3^2 \times 2$; so $m = 2$ and $d_1 = 2$ and $d_2 = 1$

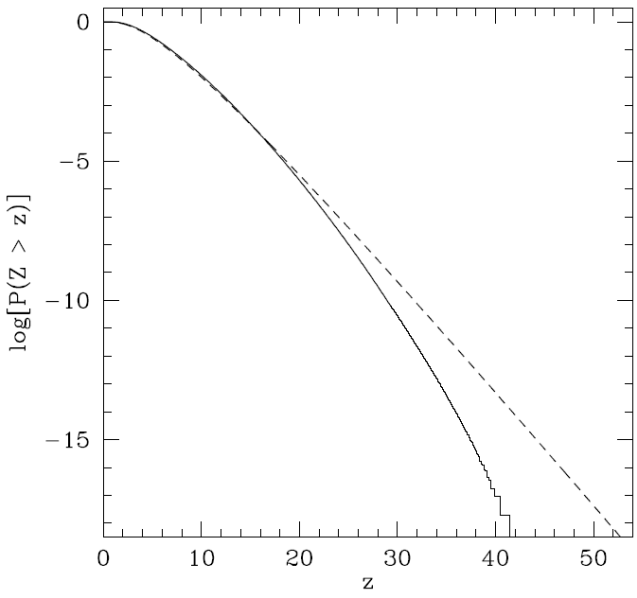

Figure 2.11: Comparison between the continuous and discrete probability distributions. The continuous, Γ, approximation is the dashed line while the actual (discrete) distribution is a solid line. The assumed values for both distributions where $N_P = 27000$ and $T = 4$. In the graph z is the rank product statistics in Equation 2.15. (Image taken from Lehner et al., 2010, Fig. 4.)

2.5 TAOS-II PROJECT.

Although TAOS I can provide strong upper limits for the KBO size distribution at the faint end, which can help to constrain some model parameters, a larger event rate is needed in order to discriminate between the size distribution models. A larger survey that is capable of detection 10's to 1,000's of events is needed to definitively probe the faint end of the Kuiper Belt size distribution.

The TAOS II was designed with one scientific objective: increase the event rate over the TAOS I survey by a factor of 100. This goal is achieved by a combination of a better site, larger aperture telescopes, and higher signal-to-noise photometric measurements. Accordingly, the name of the project was changed to Transneptunian Automated Occultation Survey, leaving the acronym unchanged. The OAN, located in SPM in the state of Baja California in Mexico, was selected as the new site where the TAOS II will be built. This site has ~ 250 observable nights per year and a median seeing of 0.59" Michel et al. (2003), this achieving the goal of a better site.

DESIGN	TAOS I	TAOS II
OBSERVABLE NIGHTS	50/year	250/year
APERTURE	0.5 m	1.3 m
BACKGROUND	16 e^-	2 e^-
EXPOSURE TIME	105 ms	50 ms
FIELD OF VIEW	3 $\square^o$	2.3 $\square^o$

Table 2.2: Comparison of design parameters of TAOS I and TAOS II. (Lehner et al., 2007; TAOS-II, 2012)

This new stage of the TAOS project will have 3 telescopes with the design parameters shown in the Table 2.2. Also, the project aims to enhance the detectable event rate by increasing the number of stars being monitored and the sampling frequency of the photometry. A simple estimate shows that simultaneous monitoring of 10,000 stars is needed to achieve the goal of increasing the detection efficiency by a factor of 100. However, conventional astronomical CCD chips could only operate below 3 MHz to provide reasonable noise level and flawless charge transfer efficiency. The basic specifications of the new camera could be summarized as:

1. Provide sky background limited performance. The readout noise should be < 2 electrons.
2. Provide a reasonable PSF sampling. The camera will consist of about 70 M pixels. Buttable device is needed for a mosaic in the focal plane.
3. Operate at 20 Hz without the zipper mode operation. Total pixel rate should be higher than 1.4 Gpx/s unless programmable partial readout is provided.
4. Higher than 90 % sampling duty cycles. Non destructive readout or a readout buffer is needed.

Just as its predecessor TAOS I, once in operation the TAOS II project will be the only instrument capable of confidently detecting sub-kilometer KBOs and possibly Sedna-like and Oort Cloud objects.

The results to be derived in this thesis will be very useful in the analysis of TAOS I data, with the upgraded 10 Hz cameras, as well as future TAOS II data.

3

Objectives and Justification.

This work will involve carrying out and analyzing numerous simulations of stellar occultation lightcurves taking into account diffraction effects in order to accomplish the following objectives:

a) calculation of the detection probability of occultation events at 10 Hz sampling rate with diffraction effects for different: impact parameter, time offset, magnitude and spectral type of the source, distance and size of the occulting object.

Diffraction effects in occultation events depend on several parameters, in order to determine if a certain event will be detected, taking into account the quantity of variables involved, we need to estimate a unique parameter that will let us know this information. This is accomplished by calculating the event probability, by means of rank statistics, of each point of the light curve. We can discern when an event occurs if the p-value of the event is greater than the noise.

b) design and selection of signal filters to improve the detection probability.

The diffraction lightcurves take different shapes depending on the KBO parameters, some of these lightcurves have more than one drop that could take the same rank value. For such reason, we need to design filters to eliminate this effect and improve the detection probability. Among the filters designed we will select the one that more certainly improves the detection probability.

c) elaborate a database with the simulated diffraction lightcurves.

This is a natural byproduct of the simulation process and is of importance because it allows the comparison of these with the observed light curves in order to obtain the main parameters for the TNO, i. e., its distance to Earth and its size.

4

Methodology.

The simulation of the occultation lightcurves was performed in two stages, both with a sampling rate of 10 Hz and a fixed distance to Earth, meanwhile controlling the object size in a range of 0.4 to 30 km. The first part (Section 4.1) is mainly descriptive, consisted in simulating lightcurves with a systematic variation of parameters: time offset, impact parameter, apparent stellar magnitude and spectral type. The purpose of such simulation was to observe the behavior of the $p-value$, in terms of the parameters mentioned above, and crudely estimate what values result in a more significant $p-value$, and as a consequence, greater occultation event recovery.

The second part (Section 4.2) focuses on the calculation of the effective solid angle (shortly defined in Section 4.2) of several object sizes located at a given distance from Earth ($\Delta = 43$ AU). It was necessary to simulate, for this purpose, the random detections during observation of stellar occultations by KBOs, which can be reflected by assigning random values to some of the before mentioned parameters, such as, the impact parameter, time offset, the apparent magnitude and angular size of the star. We incorporated a variation of their position relative to the opposition with Earth (opposition angle) from 0 to 60 degrees.

Signal filters, eight of them (Section 4.2.1), were designed and implemented on the lightcurves simulated in the second part, these filters are mathematical operations between consecutive measurements of flux. In the simulation of the first part we noticed that due to the varying size of the objects, the drop in flux takes sometimes more than 2 consecutive points, which reduces the significance of the event, while in other circumstances, the signal to noise ratio is very low and the event is often confused with noise. The filtering was performed to assess whether any of the filters helps to increase the statistical significance of a given event. The effectiveness of each filter is determined by comparing the value of the effective solid angle of each filter with that obtained by not using them.

4.1 HOW TO SIMULATE THE OCCULTATION LIGHTCURVES.

In order to simulate the occultation lightcurves, it is necessary to consider diffraction effects. The diffraction effects depend mainly on the object size, D, the object distance to Earth, Δ, and the source size, θ_* (i. e., the apparent stellar angular size), which means that the source has a finite size instead of being a point source and that the wave front is not plane. In this initial part, the object distance considered is $\Delta = 42$ AU, which is a representative distance of the Kuiper belt.

The generation of the diffraction patterns follows the procedure illustrated in Figure 4.1, which I automatized within the code `generate_b-off.c` that uses the subroutines made by the TAOS Project team based on Nihei et al. (2007) work. Each step done in `generate_b-off.c` take in account the values shown on the Table 4.1.

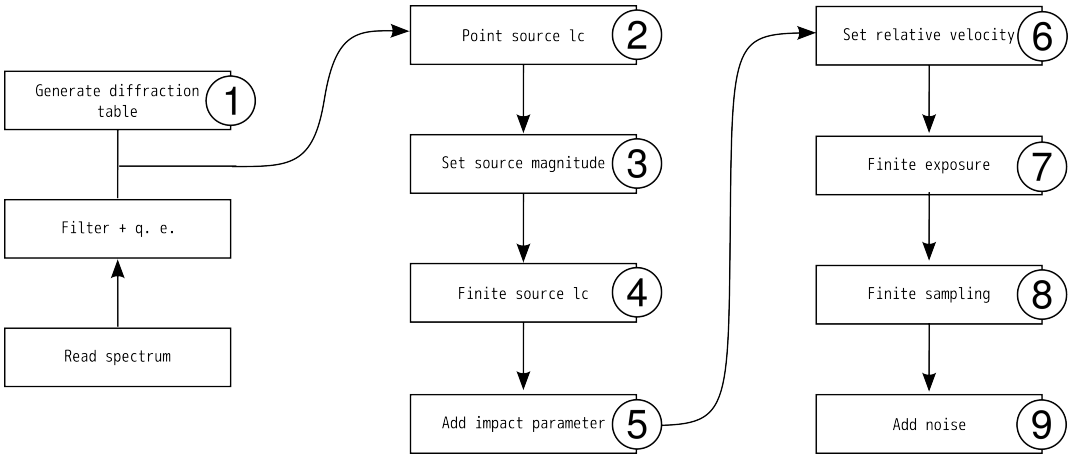

Figure 4.1: Scheme of the steps to follow to generate the diffraction patterns by stellar occultation by the transit of a TNO of determined size, observed with a b impact parameter and t_{off} time offset.

1) DIFFRACTION TABLE. A diffraction table is generated, that is a file with intensities as function of $r_F = r/F$[1] and $x_F = x/F$[2] normalized by the Fresnel scale, F, which is loaded to memory at the same time that the stellar spectra is read and filtered by the band-width of the system to simulate, in this case, the filter used by the TAOS instruments, and the quantum efficiency of the camera. In addition to the stellar spectra, one needs to know the minimum and maximum radii of the ob-

1 Where r is the radius of the object.
2 x is the distance from the line of sight.

jects (normalized by the Fresnel scale), this indirectly involves setting the distance of the objects to Earth, and the mean wavelength of the filter, $\bar{\lambda}$, to calculate the Fresnel scale $F \sim 1.4$ km, given by Equation 2.8, taking $\bar{\lambda} \approx 600$ nm and $\Delta = 42$ and 43 AU.

2) POINT SOURCE LIGHT-CURVE. At this stage a diffraction pattern in which the light source is a point is generated. It is weighted by the filtered spectrum. The light curve is a function of two parameters, the distance ($\Delta = 42$ AU is used throughout our study) and the object size.

3) SOURCE MAGNITUDE. The magnitude of the source is established, this sets the photon flux and the apparent stellar radius for a given spectral type.

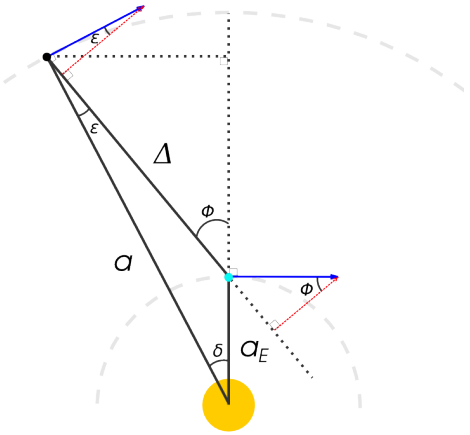

Figure 4.2: Diagram helpful to deduce the relative transverse velocity, v_{rel}. The transverse velocity is the perpendicular component (red vectors) of the orbital velocity (blue vectors) to the vector that joins the two bodies. In the diagram, the angle of opposition, ϕ, can be seen, this in conjunction with the KBO's distance to Earth, Δ, are the parameters we know.

4) FINITE SOURCE LIGHT-CURVE. Next comes the generation of a finite source light-curve, integrating the point source light curve over the stellar surface.

5) IMPACT PARAMETER. The impact parameter, b, is determined setting the distance of nearest approximation of the line of sight to the center of the diffraction pattern in the program. It is introduced in the program in fractions of the EVENT CROSS SECTION given by Equation 2.11c.

6) TNO RELATIVE VELOCITY. Up to this point everything is function of the distance to the center of the pattern. To obtain the information about the time evolution of the signal we have to calculate the transverse velocity (red vectors in Figure 4.2) of the TNO relative to Earth , v_{rel}, that is a function of the opposition angle of the occulting object, ϕ, and its distance to Earth, Δ, according to:

Object's relative transverse velocity.

$$v_{rel}(\Delta, \phi) = v_E \left[\cos\phi - \sqrt{\frac{\Delta_E}{\Delta}\left(1 - \frac{\Delta_E^2}{\Delta^2}\sin^2\phi\right)} \right] \tag{4.1}$$

where the subindex "E" indicates the terrestrial values, distance to the Sun $\Delta_E = 1$ AU and velocity $v_E = 29.8$ km s^{-1}. The relative transverse velocity between the Earth and the TNO can be deduced using the Figure 4.2, taking into account that the only angle known is ϕ and that the approximation $\Delta \simeq a$ can be done. For an object with a $\phi = 0$ and at a distance $\Delta \sim 43$ AU, the relative velocity $v_{rel} \approx 25.25$ km s^{-1}. Having this information, the occultation duration, $\mathcal{T}$, is given by:

Occultation duration.

$$\mathcal{T} = \frac{H}{v_{rel}} \tag{4.2}$$

Using Equation 4.2 and Equation 2.11c for an object of $D = 1$ km at $\Delta = 43$ AU, results in an occultation duration of $\mathcal{T} \approx 0.2$ s.

7) FINITE EXPOSURE LIGHTCURVE. It is generated by the integration over the time exposure for each point of the continuous lightcurve.

8) FINITE SAMPLING LIGHTCURVE. Finally, one obtains a lightcurve that is like the one measured in the telescope in absence of the noise and that has a given sampling frequency, in our case of $f_{sam} = 10$ Hz. At this point the information about time offset, t_{off}, is included. The time offset is the temporal dephasing between the observation and the center of the diffraction pattern, i. e., the Poisson point. The resulting light curve includes the variation of each one of the important parameters that are desired to study along this work.

	D	SPECTRAL TYPE	b	t_{off}	M_*
VALUES	0.6, 0.8, 1, 3, 5, 10, 20 & 30	F0V, G0V, K0III, K0V & M0III	$\triangle b = 0.05$	$\triangle t_{off} = 0.02$	$\Delta m = 1$
RANGE	———	———	0 - 0.5	0 - 1	7 - 14
UNITS	km		H [km]	$1/f_{sam}$ [s]	mag

Table 4.1: Values of the parameters to be used to generate the different diffraction patterns, where D is the size of the TNO, b is the impact parameter, t_{off} is the time offset and M_* is the magnitude of the source, that is also related with stellar angular size.

9) NOISE. It is necessary to incorporate the expected noise of an observed lightcurve to make a realistic simulation, thus, a set of T PHOTOMETRIC lightcurves is created. A photometric lightcurve is a series of random points with specific average flux (given by the source magnitude) and signal-to-noise ratio, SNR, as standard deviation. The SNR definition is expressed in (Equation 4.3).

$$\frac{S}{N} = \frac{\sum \text{Sources of signal}}{\sqrt{\sum \text{Sources of noise}}} \tag{4.3}$$

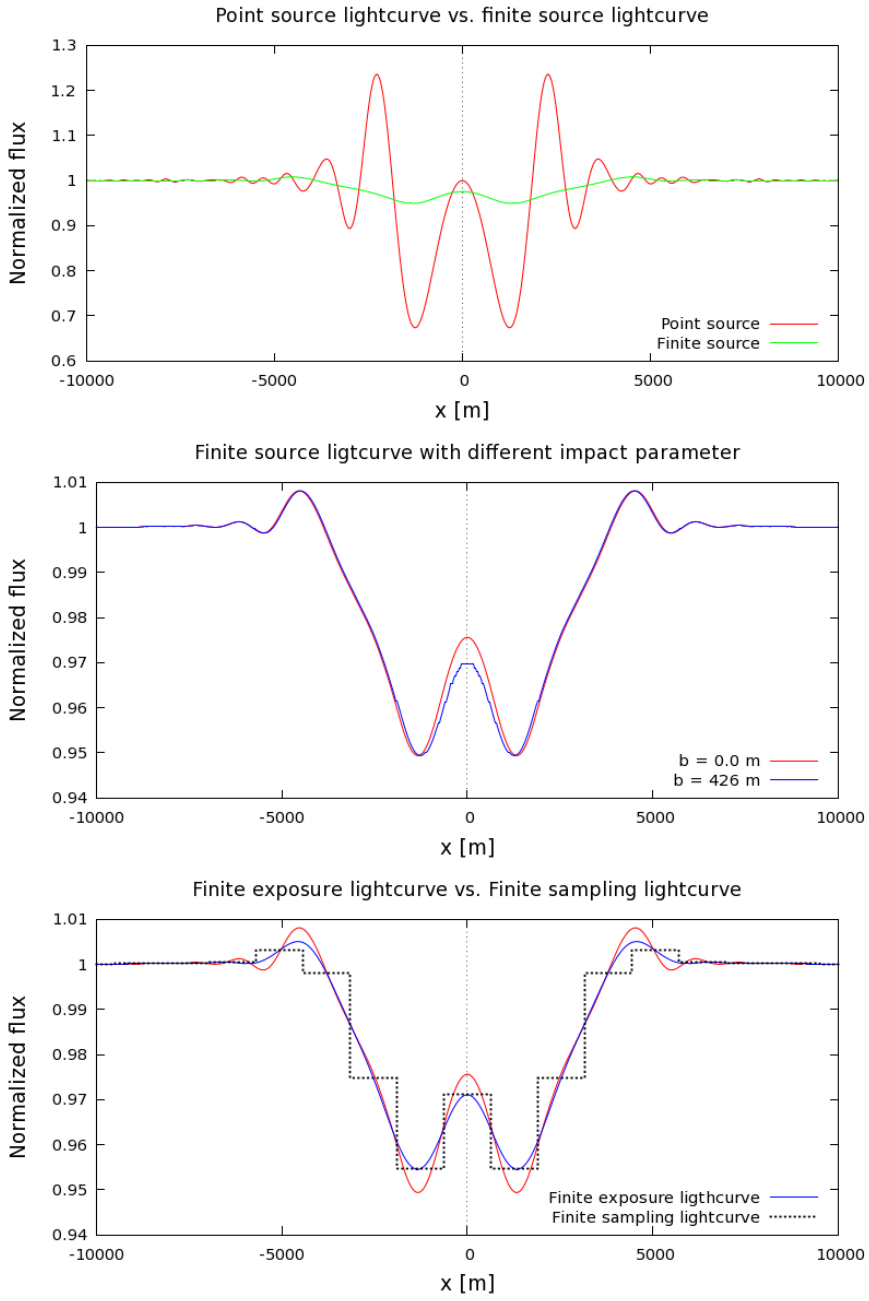

Figure 4.3: Comparison between the steps of the generation of the diffraction lightcurve for an object of $D = 1$ km, at $\Delta = 42$ AU and a F0V star of magnitude $m = 7$ with `generate_b-off.c` code. Each lightcurve has been already normalized only to exalt the differences between each other. Top panel: shows the difference between the point-source and finite source lightcurves (steps 2 to 4). Middle panel: incorporation of impact parameter, b, to the finite source lightcurve (step 5) where $b \neq 0$ m (blue line). Bottom panel: comparison between a finite source lightcurve, its finite exposure (step 7) and sampled lightcurve (step 8) with $f_{sam} = 20$ Hz, it can be seen that the difference among this last two is that the first is infinitely sampled.

The expected noise in the flux measurement of a bright object comes not only from the source (the star), but also from the background flux. An always present noise source is the one that is originated in the process of image reading, the READ NOISE R, which depends exclusively on the detector used and consists in the repeatability on the conversion of an analog signal (number of electrons in a pixel) to a digital number, and of the intrinsic electronic noise related to the spurious electrons introduced in the entire procedure (more information in Howell, 2006, section 3.2). Particularly for the TAOS project, is important to consider the SCINTILLATION NOISE (Equation 4.5) given the combination of the high sampling frequency and the small aperture size (50 cm) of the telescopes. Taking into account the previous considerations, the total noise, N, is:

$$N = \sqrt{\frac{\mathcal{F}}{G} + A^2\left(\frac{\mathcal{F}_{sky}}{G} + R^2\right) + (\mathcal{F} \times N_{sci})^2} \tag{4.4}$$

which is function of the source flux, $\mathcal{F}$, in ADU; the sky flux, $\mathcal{F}_{sky}$, in ADU; the CCD gain, $G = 2e^-/\text{ADU}$; the size in pixels of the source, $A = 3$; the readout noise ($R = 5.5$) in ADUs, and the scintillation noise, N_{sci}, given by (Young, 1967, 1974):

Scintillation noise.

$$N_{sci} = S_0\, \mathcal{D}^{-2/3}\, X^{7/4}\, e^{-h/h_0} \sqrt{\frac{f}{2}} \tag{4.5}$$

where $\mathcal{D}$ is the telescope aperture in centimeters; S_0 is the scintillation constant that depends of the site, typically $S_0 = 0.09$ (if working with $[\mathcal{D}] = \text{cm}$) but in this case $S_0 = 0.11$; X is the airmass; $h = 2880$ m is site height over sea level; $h_0 = 8000$ m is the atmospheric scale height and f is the sampling frequency in Hz (Young, 1967). The sampling frequency used throughout this work is $f = 10$ Hz.

Afterwards, the diffraction lightcurve is normalized according to its constant segment, i. e., the value of the constant section must be 1 after normalization, and then "inserted" on a given position, i_{in}, inside the photometric lightcurve. This "insertion" is the multiplication of the fluxes of the normalized diffraction lightcurve with the ones in a "window" of its same size (centered in i_{in}) of the photometric lightcurve. The sizes of the diffraction and photometric lightcurves differ, the photometric lightcurve size was set to have 54000 points of random flux while the size of the diffraction lightcurve is less than 100 points of flux, thus, the flux window has this same size. The insertion procedure is realized in each lightcurve in the set, resulting in a set with the same implanted occultation event but with different noise distribution. The i_{in} of the event implanted is the same for the T lightcurves, it is the center of the diffraction pattern and has greater chance to be significant, meaning that, it is the place where we are interested to inspect[3] in each of the

3 This is done also with the two neighbors backwards and forward.

simulations.

In order to know what is the statistical significance of the event, the correspondent rank is assigned to each point of the lightcurve, this applies to every member of the set. We proceeded with the rank statistics as previously described (Section 2.4.1), so the rank product over the T lightcurves was done and then the calculation of the $p-value$ as explained by Lehner et al. (2010). If the $p-value$ of in the event, with a position $i_{in} \pm 1$, is $\mathbb{P}(Y \leqslant y) < 10^{-11}$ the event is considered as statistical significant and therefore recovered.

4.2 EVENT RECOVERY CODE AND EFFECTIVE SOLID ANGLE CALCULATION.

Clearly, it is desirable to calculate or estimate a quantity which can tell us how efficient a survey is at detecting a given object, as its the case of the DETECTION EFFICIENCY, ϵ_l, and THE EFFECTIVE SOLID ANGLE, Ω_e. In our simulations, both quantities are related to the number of events recovered (or detected), N_{rec}, from a given number of simulated events (added to our sample), N_{add}. The detection efficiency is the simplest relationship between these two numbers, since it is only the ratio between them (Equation 4.6). While, as will be seen below, the effective solid angle is "weighed" by the characteristics of the retrieved events and not just their number.

The detection efficiency can be expressed as a function of the object size, D, and its distance to Earth, Δ, such that the fraction of events happening at given Δ with a size D, is given by:

Detection efficiency.

$$\epsilon(D,\Delta) = \frac{N_{rec}(D,\Delta)}{N_{add}(D,\Delta)} \tag{4.6}$$

As discussed in Wang et al. (2009), the number of expected occultation events, N_{exp}, to be seen for a given star during the entire data set of an occultation survey (Equation 4.7) depends on two factors, a model-dependent factor, n, related to the real space and size distribution of KBOs, and a survey-dependent factor Ω_e, related to the object a given survey could detect.

Number of expected occultation events per size per distance to Earth.

$$\frac{d^2 N_{exp}(D,\Delta)}{dD\, d\Delta} = \frac{d^2\, n(D,\Delta)}{dD\, d\Delta}\, \Omega_e(D,\Delta) \tag{4.7}$$

The number of events detected during the observations, in a survey and the value of Ω_e, determined by simulations, can constrain $n(D,\Delta)$ and therefore help establish what theoretical models are acceptable according to the observations, hence

the importance of its calculation.

The $\Omega_e(D,\Delta)$ factor is what Zhang et al. (2008) defines as the EFFECTIVE SOLID ANGLE[4] (also called EFFECTIVE SKY COVERAGE by Bianco et al. (2010)), which is the solid angle where the survey is capable of counting every KBO of diameter D with 100% efficiency.

There is a great interest in determining the effective solid angle of the TAOS I project because the cameras were updated and have the capacity of taking images at a rate of 10 Hz (twice the cadence of previous capabilities). This quantity was unknown before this work carried out. The second stage of this thesis focuses on its estimation.

The calculation of $\Omega_e(D)$ can be done, based on Equation 4.8, with data extracted from simulations of occultation lightcurves whose parameters have values similar to those of the observational lightcurves. This implies that some parameters will have random values. In the ideal case, all the parameters would have to be random, however it is necessary have some control over the simulations.

Effective sky coverage or effective solid angle.

The mathematical definition of the effective solid angle is:

$$\Omega_e(D,\Delta) = \frac{1}{\omega(D,\Delta)} \sum_{j=1}^{N_{rec}} \frac{v_{rel}(\Delta,\phi_j)}{\Delta} \frac{H_j(D,\Delta,\theta_*)}{\Delta} E_j \tag{4.8}$$

where E_j is the duration of the data run in seconds; H, is the cross section of the event (see Equation 2.11c); $v_{rel}(\Delta,\phi_j)$, is the transverse relative velocity between the TNO and the Earth, and $\omega(D,\Delta)$ is a weight factor for a diameter D and distance Δ, corresponding to the fraction of lightcurves implanted with occultations by KBOs of diameter D at a distance Δ. The sum is carried out only over the lightcurves where events were recovered. The weighting factor can be calculated by means of the false positive rate (0.25), the $p-value$ threshold ($\mathbb{P}_{thr} = 10^{-11}$), the total number of flux measurements (points) in the lightcurve ($N_P = 54000$) and the number of total simulated lightcurves (N_{add}) (Lehner and Zhang personal communication), and is given by:

$$\omega(D,\Delta) = \frac{N_{add}(D,\Delta)\, N_P\, \mathbb{P}_{thr}}{0.25} \approx 2.16 \times 10^{-6}\, N_{add}(D,\Delta) \tag{4.9}$$

The generation of the occultation lightcurves followed the basic procedure in Section 4.1 but we provided random values to the parameters indicated in Table 4.2. Also, to perform the simulation, a random selection of stellar angular size, θ_*, and

4 Zhang et al. (2008) expresses $\Omega_e(D,\Delta)$ as $\Omega_e(D)$ because the authors considered Δ as a constant in the paper.

apparent magnitude, M_*, from a targeted TAOS star field, containing only information of F0V stars, was realized with every new lightcurve set. The magnitude ranged from 7 to 14.2 in the red wavelength, which implicity is a variation of the signal-to-noise ratio.

	D	ϕ	b	t_{off}	M_*
VALUES	0.4, 0.6, 0.5, 0.7, 0.8, 1, 2, 3, 8, 15 & 30	0, 45 & 60		Random	
RANGE	———	———	0 - 0.5	0 - 1	7 - 14.2
UNITS	km	deg	H [km]	$1/f_{sam}$ [s]	mag

Table 4.2: Values of the parameters to be used to generate the different diffraction patterns for the 2nd stage of this thesis. The values for b, t_off, i_{in} and θ_* are random, this last one is somehow related to the M_*

Two important differences between the calculation carried out in this and the previous stage of the thesis, as previously stated, are the filtering of the set of photometric lightcurves before doing the rank statistics and the implementation of the event recovery code that gives as output, among other things, necessary information to calculate the effective solid angle, as well as the number of simulated lightcurves needed, N_{add}, to recover certain number of events, N_{rec}.

The recovery code, `sim_rec.c` is responsible, broadly speaking, for creating the diffraction and photometric lightcurves with the randomized parameters on Table 4.2, carrying-out the filtering of the flux with the filters in Section 4.2.1, calculating the $p-value$ of the simulated event and determining whether it is significant and, if it is, of saving the values of the parameters of the lightcurve (specially the randomized ones). It has as input the size of the object in kilometers, the assumed opposition angle in degrees and the sampling frequency (the precise values used can be seen in Table 4.2). It uses as threshold to select which event is recovered the $p-value$ $\mathbb{P}(Y \leqslant y) = 10^{-11}$. The algorithm that `sim_rec.c` follows is as described:

1. Read the finite source lightcurve[5]. Each lightcurve is stored in a file which has a defined location and automatic name.

2. Choose a random value of $b \in [0, 0.5\,H]$, $t_{off} \in [0, 1/f_{sam}]$ with $f_{sam} = 10$ Hz and $i_{in} \in [0, N_p]$ with $N_p = 54000$.

5 Step 4 of Section 4.1

3. Read the magnitude and angular size of stars F0V from the TAOS-I field catalog and select randomly a corresponding pair of values, limiting the magnitude to $m \leqslant 14.2$.

4. Complete the procedure going from finite source lightcurve[5] to finite sampling lightcurve[6] and the creation of the photometric set. At the same time, the counter of added lightcurves is increased by 1 ($N_{add} = N_{add} + 1$).

5. The filters are applied to each lightcurve of the set. The description of the filters will be presented in Section 4.2.1. A loop is initialized over the filters and the photometric set is saved to use it with the next filter.

6. Ranking of the resulting filtered flux is carried out.

7. The probability values are calculated as in the previous section (Section 4.1).

8. Inspection of the $p-values$ in a window surrounding i_{in} of $\triangle i_{in} = \pm 2$, in a way that $\mathbb{P}(j) < 10^{-11}$ where $j \in [i_{in} - 2, i_{in} + 2]$. If this happens at any of the points for any of the filters, then the event is considered to be recovered and the respective counter increase by 1 ($N_{rec} = N_{rec} + 1$).

9. If the previous step is true, the values indicated in Table 4.3 are stored in a single line for each recovered event in an output file. The output file will have 500 lines of information, which is the maximum number of events retrieved we consider.
   The parameters whose values are strictly needed to calculate the effective solid angle are the first seven located on the left side of Table 4.3.

D	ϕ	t_0	b	θ_*	SNR	N_{add}	$\mathbb{P}_{min,F\#}[i_{in} \pm 2]$							
							NF	F1	F2	F3	F4	F5	F6	F7	F8
							$j = i_{min} - i_{in}$ where $\lvert j \rvert \leqslant 2$								
							NF	F1	F2	F3	F4	F5	F6	F7	F8

Table 4.3: Information of the lightcurves stored as output by `sim_rec.c`. The F# makes reference to the filter number, which description is at Section 4.2.1, and where NF means no filter used. The minimum $p-value$ per filter within a window i_{in}, $\mathbb{P}_{min,F\#}[i_{in} \pm 2]$, where i_{in} is the insertion point, and the displaced position of the minimum $p-value$ from the insertion point, j, are saved as well.

10. The values in Table 4.3 are saved for each of the simulated sets of lightcurves in a file properly marked. This file can be considered as a backup of the

6 Step 8 of Section 4.1

information of the complete simulation that could be used for additional or complementary purposes without having to re-run the simulation.

11. If N_{rec} equals the desired limit ($N_{rec} = 500$) or N_{add} reaches a defined limit ($N_{add} = 2 \times 10^5$), the procedure is stopped. Otherwise e go to step 2.

4.2.1 *Filters used.*

The filters used are described in Equations 4.10 to 4.17. The selection of filters take into account different number of consecutive points corresponding to the expected number of points that characterize some flux drops depending on the object size. Occultations by objects with greater size lead to events with a greater duration in time, such that the quantity of points observed at a certain cadence increases also for bigger objects.

Taking f_i as the value of the flux at time i, the filters we consider correspond to the following combinations of flux measurements:

$$F1_i = \frac{f_{i+1} + f_i}{2} \tag{4.10}$$

$$F2_i = f_{i+1} - |f_i - f_{i+2}| \tag{4.11}$$

$$F3_i = -|f_i - f_{i+1}| \tag{4.12}$$

$$F4_i = \frac{f_{i+1} + f_i + f_{i-1}}{3} \tag{4.13}$$

$$F5_i = \frac{f_{i+2} + f_{i+1} + f_i + f_{i-1} + f_{i-2}}{5} \tag{4.14}$$

$$F6_i = \frac{f_{i+3} + f_{i+2} + f_{i+1} + f_i + f_{i-1} + f_{i-2} + f_{i-3}}{7} \tag{4.15}$$

$$F7_i = \frac{f_{i+4} + f_{i+3} + f_{i+2} + f_{i+1} + f_{i-1} + f_{i-2} + f_{i-3} + f_{i-4}}{8} \tag{4.16}$$

$$F8_i = \frac{f_{i+4} + f_{i+4} + f_{i+3} + f_{i+2} + f_{i+1} + f_{i-1} + f_{i-2} + f_{i-3} + f_{i-4} + f_{i-5}}{10} \tag{4.17}$$

Where FX_i corresponds to the value of filter X ($X = 1...8$) at time i. Almost all of these combinations can be described as the average of certain number of consecutive points. The noise level is thus reduced in the filtered signal and as result there is an increase of the SNR and the corresponding detection probability as measured by the $p - value$.

4.2.2 *Code that computes the effective solid angle*

It is essential to calculate Ω_e from the information obtained above (filtered signals) in a fast and reliable way. Thus a third code was written, named as `esolidang.c`, which reads the output file of `sim_rec.c` of the retrieved events and seeks in the correspondent columns for each filter if they possess a $p - value$ less than the

threshold and counts every time this happens. At the end we have the number of recovered events per filter, $N_{rec,F\#}$.

The input data of `esolidang.c` is a list of names of output files from `sim_rec.c` "listrec" (with different D and ϕ), the output name, where the $\Omega_{e,F\#}(D, \Delta, \phi)$ per file in the previous list will be written, the total number of filters to consider, and the total number of points in the lightcurves.

As can be noticed, from the definition (Equation 4.8) Ω_e not only depends on D and Δ, but also of the opposition angle ϕ, while the quantities E and Δ (in Equation 4.8) remain constant[7], having values $E = 5400$ s and $\Delta = 43$ AU. Expressing Δ and E as constants in Equation 4.8, the effective sky coverage can be written as:

$$\Omega_e(D, \Delta, \phi) = \frac{E}{\omega(D, \Delta)} \frac{\nu_{rel}(\Delta, \phi)}{\Delta^2} \sum_{j=1}^{N_{rec}} H_j(D, \Delta, \theta_*) \tag{4.18}$$

The output file has the same number of lines as names in "listrec", and each line has the information in Table 4.4.

D	ϕ	ν_{rel}	N_{add}	$N_{rec,F\#}$								
				NF	F1	F2	F3	F4	F5	F6	F7	F8
				$\Omega_{e,F\#}$								
				NF	F1	F2	F3	F4	F5	F6	F7	F8

Table 4.4: Information stored as output by `esolidang.c`. The F# refers to the filter number, described in Section 4.2.1, and NF means that no filter was used.

7 Meaning that $E_0 = E_1 = E_j = E$ and the same for Δ.

5

Results.

With the intention of giving some continuity to the methodology chapter (Chapter 4), this chapter is presented into 2 parts.

5.1 Behavior of the probability for different parameters.

The quantity of lightcurves generated in Section 4.1 is as large as 140000. To analyze these information, we had to find a way to easily interpret the 140000 lightcurves. We choose to took only the $p-value$ of the occultation event in its insertion point ($i_{in} \pm 1$) within the photometric light curve, and see how it behaved given the set of parameters in Table 4.1. Having the relation among $\mathbb{P}[i_{in} \pm 1]$, b, t_{off} and M_*, we constructed probability color-maps against the time offset, t_{off}, and impact parameter, b. Every graph is specific for an object size, a spectral type and magnitude of the source star, as shown in Figure 5.1 to 5.3, there was not any filtering at this stage. Dark blue regions in such plots correspond to observing parameter combinations for which a detection is likely. The corresponding D and stellar spectral type is labeled in each of the three figures.

From the $p-value$ color-maps, we observed that the detection of a given object could be less hardly accomplished if the source star has a magnitude of 7 (Figure 5.1). When the stellar brightness is reduced, is more difficult to detect events, (Figure 5.2 & 5.3), particularly of small bodies. There is a similar trend when the angular size of the source increases, going form early to later stellar spectral type, since the diffraction effect is clearer when the source of light tends to be punctual, specially the "depth" of the drop of the occultation.

The smaller the object, the harder is to observe the related flux reduction in the lightcurve. We noticed that for larger objects, like the 30 km bodies, the $p-value$ does not change significantly with the angular size of the source or with the magnitude. In all cases the value seems to be the same ($\mathbb{P} \sim 10^{-10}$). This effect could be attributed to the duration of the occultation either in time or number of sampling points and the random noise (as it will be discussed in Chapter 6).

Figure 5.1: Probability color maps of occulting KBOs, with sizes D = 30, 1 and 0.6 km at $\Delta = 42$ AU, that crosses infront of stars of indicated spectral type and magnitude 7. The color-bar indicates the $\log_{10}(\mathbb{P})$, the least the value of the $p-value$ the greater the certainty of detection. The stellar angular size, θ_*, increases from F0V to M0III for a given magnitude.

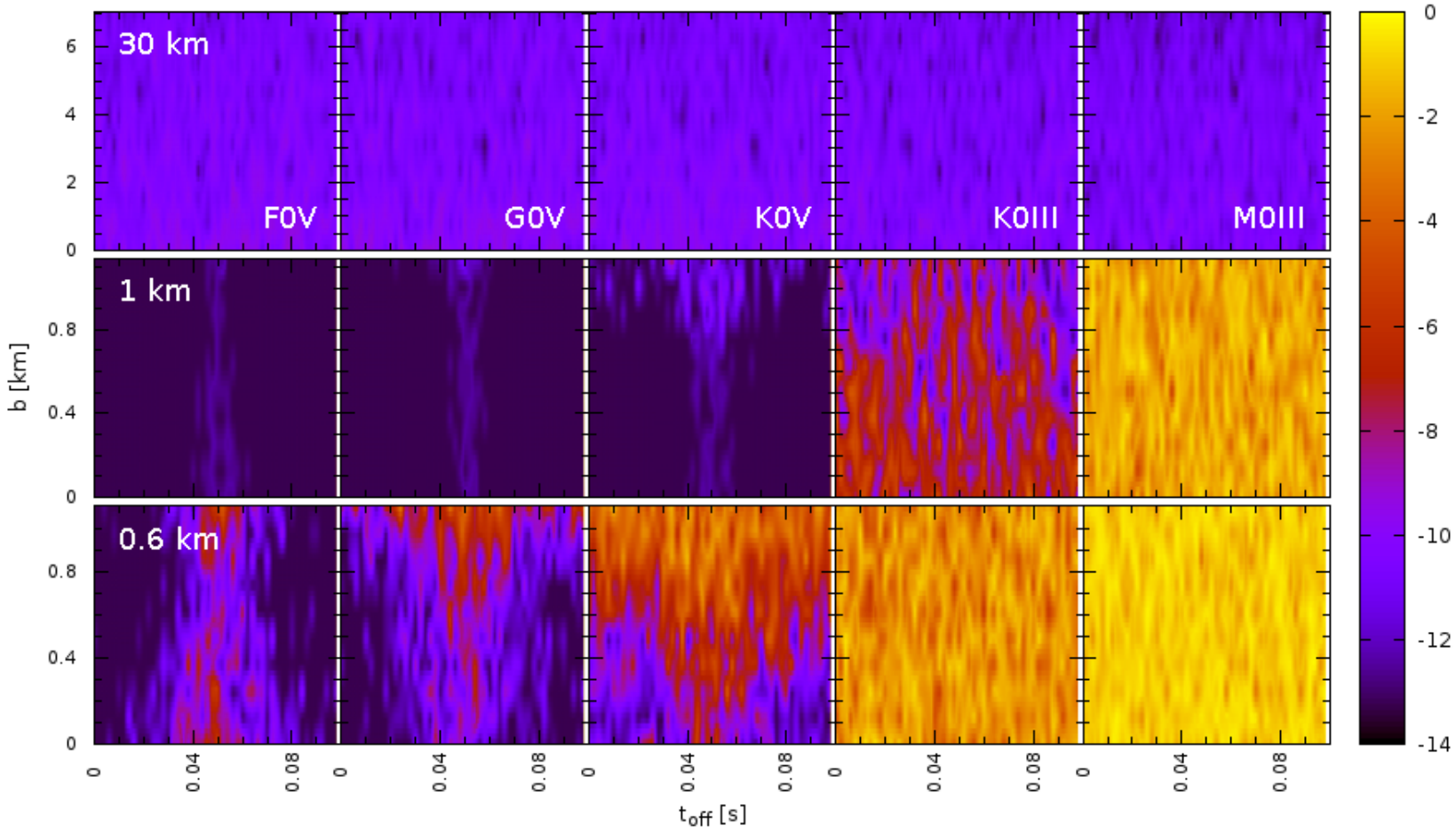

Figure 5.2: The same as Figure 5.1 but for stars of mag 11.

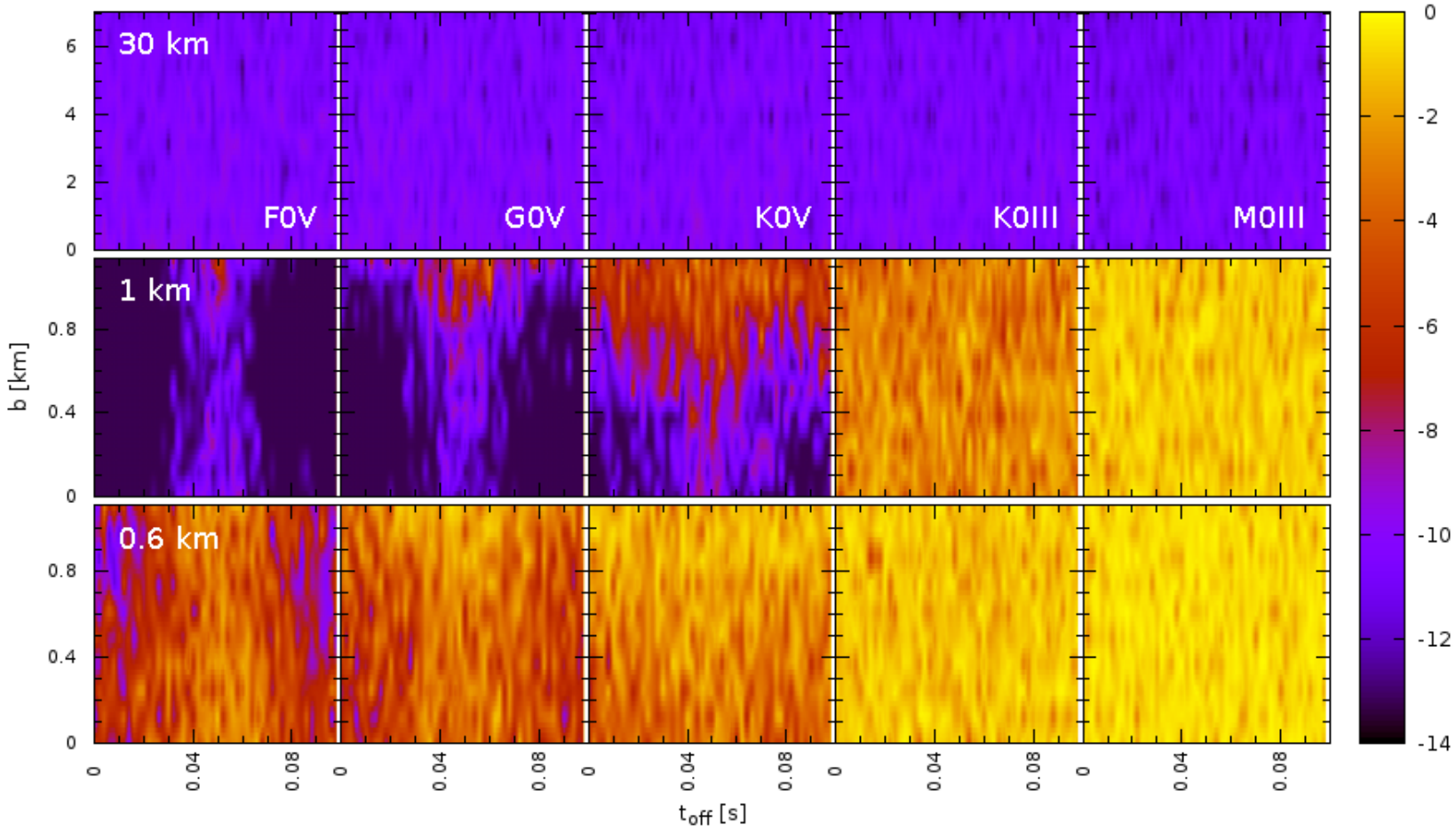

Figure 5.3: The same as Figure 5.1 but for stars of mag14.

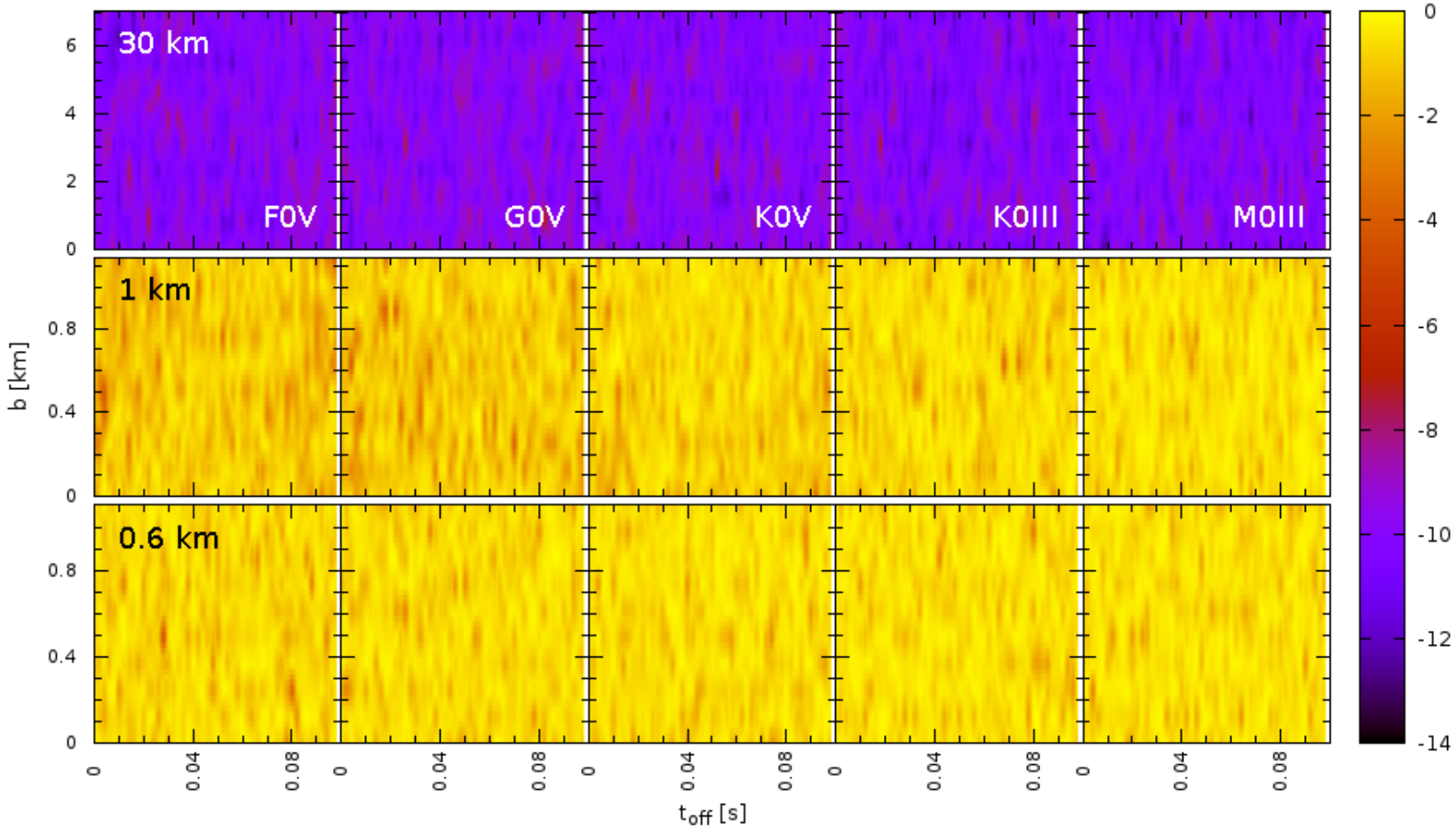

5.2 DETECTION EFFICIENCY AND EFFECTIVE SOLID ANGLE.

The code `sim_rec.c` was configured to retrieve a maximum of 500 detected events ($N_{rec} = 500$) as long as the total number of added lightcurves, N_{add}, was less or equal than 2×10^5. Each lightcurve, as described in Section 4.2, has a random value of impact parameter, time offset, stellar angular size and stellar magnitude. The code was executed 10 times for each combination of object size and opposition angle in Table 4.2 with a different realization of the random numbers. Afterwards, the average value of $N_{add}(D, \phi)$ and $N_{rec}(D, \phi)$ was calculated, as well as its respective standard deviation. The corresponding values are presented in Table 5.1.

As shown in Table 5.1, for most parameter combinations, the number of events retrieved exceeds 500. During the analysis of the data obtained searching for the 500 recovered events, we found that these included only those recovered after applying any of the filters, but not those which met the p-value threshold without any filter applied. In other words, a bias in the number of unfiltered recovered events was found, in the worse case the total number of recovered events would be greater than 500 without needing to re-execute the simulator of lightcurves. To eliminate this bias, an additional code (`checkNrec.py`) was written and executed to analyze the file containing the information of all the lightcurves made for p-values $\leqslant 10^{-11}$ in the corresponding unfiltered column.

The Table 5.1 shows the "raw" number of recovered events which means the number of lightcurves with an event detected whether these were filtered or not. From the table, one can compute the TAOS I detection efficiency (Equation 4.6) sampling with a rate of 10 Hz. The efficiency obtained for each of the 3 opposition angles studied in this thesis, are compared with the results obtained by Bianco et al. (2010) in Figure 5.4. This comparison exalts the improvement in the detection of KBOs by only increasing the sampling frequency from 5 Hz to 10 Hz. As it can be observed, there is an increase in the detection efficiency by a factor of 3, 65 and 1700, for objects of 30, 1 and 0.5 km, respectively.

Interpreting Figure 5.4, one would expect also an improvement in the value of the effective solid angle, Ω_e, with respect to the results of Bianco et al. (2010) and Zhang et al. (2008) which were derived with a sampling frequency of 5 Hz.

D [km]	$\phi = 0^o$				$\phi = 45^o$				$\phi = 60^o$			
	$\overline{N}_{add}$	σ_{add}	$\overline{N}_{rec}$	σ_{rec}	$\overline{N}_{add}$	σ_{add}	$\overline{N}_{rec}$	σ_{rec}	$\overline{N}_{add}$	σ_{add}	$\overline{N}_{rec}$	σ_{rec}
0.4	200001.0	—	4.7	1.6	194268.6	18127.4	71.5	9.9	112544.0	3963.7	533.2	6.3
0.5	200000.0	—	230.0	9.4	60480.1	2601.4	602.3	11.7	14997.2	464.7	517.2	3.2
0.6	98377.6	2018.2	1152.5	25.0	15038.6	505.3	579.1	8.6	6502.2	293.9	514.9	4.5
0.7	23872.3	937.2	759.8	24.6	7431.6	248.5	559.3	7.9	3752.1	139.7	514.4	3.0
0.8	12397.6	350.5	683.5	16.5	4960.0	191.9	555.5	9.8	2583.4	123.9	513.8	2.4
1.0	5561.9	261.8	627.5	9.0	2650.1	127.2	548.5	6.6	1604.1	37.5	517.3	3.2
2.0	1507.4	61.6	552.4	10.3	1135.9	37.7	518.9	3.2	1014.8	33.2	502.8	2.6
3.0	976.5	19.5	527.1	4.3	860.4	26.3	514.5	3.9	802.9	17.3	502.6	1.5
8.0	618.2	6.9	512.1	3.0	594.2	3.4	506.6	1.7	582.6	14.3	501.0	0.8
15.0	541.6	7.2	504.3	1.8	538.0	4.1	501.8	1.9	541.5	5.8	504.6	1.5
30.0	515.2	3.0	500.8	1.2	518.9	4.1	503.0	1.6	799.0	14.5	525.8	7.0

Table 5.1: Mean values of N_{add} and N_{rec} per opposition angle, ϕ, taking into account all filters (see explanation in the text), and its respective standard deviation, σ_{add} & σ_{rec}, after running 10 times the code that recovers the events.

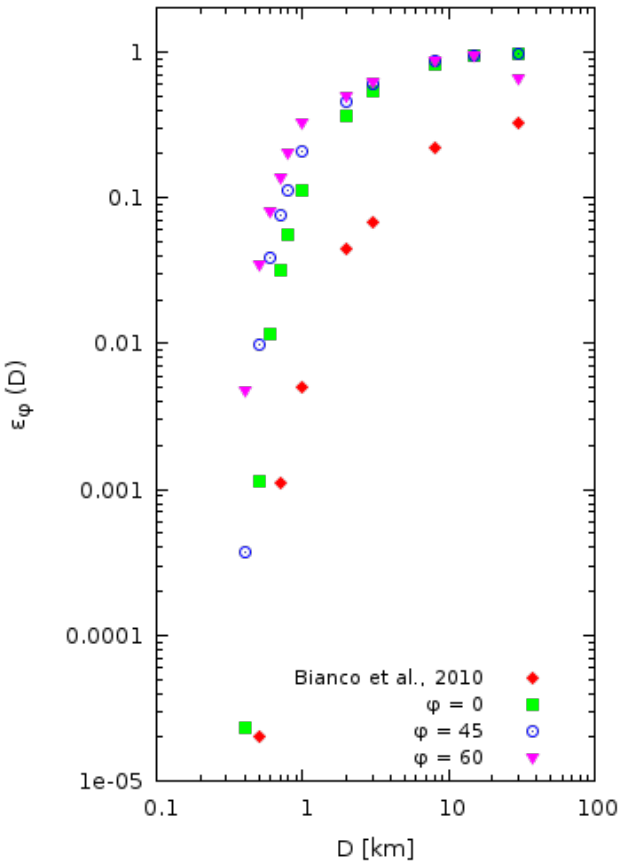

Figure 5.4: Global detection efficiency, $\epsilon_\phi(D)$, compared to the one obtained by Bianco et al. (2010) (red diamonds).

The information obtained from the recovered lightcurves such as object size, opposition angle and stellar angular size, were used to estimate the effective solid angle, Ω_e of the survey, following Equation 4.18 in Section 4.2. As mentioned before, the distance from Earth to the KBO was set at $\Delta = 43$ AU which, taking also into account the opposition angle, gave velocities[1] of $v_{rel}(43, \phi = 0) = 29.8$ km s^{-1}, $v_{rel}(43, \phi = 45) = 21.1$ km s^{-1} and $v_{rel}(43, \phi = 60) = 14.9$ km s^{-1}.

The graphs shown in Figure 5.5 to 5.8 illustrate the values obtained for Ω_e for the different filters used. Each figure includes the description of the filter and in every figure there are matching gray lines for the different opposition angles, long dashed line for $\phi = 0$, short dashed line for $\phi = 45$ and long-short-short dashed line for $\phi = 60$, for the values of lightcurves that were not filtered (NF, No Filter used).

Comparing the effective solid angle obtained from filtering and its absence is important because for some object sizes, some particular filter could be useful or not. Briefly, if the effective solid angle of a filter is greater than that without filter ($\Omega_{e,F}(D, \phi) > \Omega_{e,NF}(D, \phi)$) then it is considered as a possible option, otherwise, the filter is discarded as an option for that particular object size.

If possible, a unique filter for all object sizes is desirable, if not, an alternative is to use one filter for small objects and another one for large objects. Ideally the chosen filter for a particular size is the one with the higher effective solid angle.

1 Equation 4.1

The Figures 5.9 to 5.12, contain the same information as figures 5.5 to 5.8 just that $\Omega_{e,F}$ is normalized with $\Omega_{e,NF}$ in such a way that it is easier to determine if there is an improvement in the KBOs detection ($\Omega_{e,F}/\Omega_{e,NF} > 1$). Each of the figures is outlined with the filter used.

Apparently the absolute value filters, F2 & F3, are not very useful for any of the sizes considered, specially F3. The F2 filter recovers only objects with $D > 1$ km with an opposition angle $\phi = 60^o$. The rest of the filters retrieve objects of different sizes for more than one opposition angle (Figure 5.9, 5.10, 5.11 and 5.12). The filters that involve a greater number of points recover better larger objects, especially those with $D > 8$ km. In contrast, those filters involving two or three points (F1, F2 & F4) recover better the small objects ($D \leqslant 3$ km). The objects with sizes $3 < D < 8$ km are recovered easily without applying any filter.

As explained before, the chosen filter for a determined object size and opposition angle is the one that maximizes Ω_e. The effective solid angle obtained for each filter is resumed in Table 5.2. The number of filter that maximizes $\Omega_{e,D}(\phi)$ is dependent of ϕ, e. g., for the 1-km object the filters maximizing $\Omega_{e,1}(\phi)$ are NF ($\phi = 0$) and F1 ($\phi = 45\,\&\,60$), while for the 0.6-km object are NF, F1 and F4. The previous dependence could represent a problem if only one filter is needed for all of the opposition angles for a given size.

We could need to select one of the three filters that conform the triplet for a given object size. The selected filter must minimize the error in the estimation of the effective solid angle among the 3 filters at the same time. With this purpose we propose to consider the calculation an evalutaion of what we called, DEVIATION TO MAXIMUM δ_{max}, which consists in finding the maximum value of $\Omega_{e,D}$ between filters and subtracting each $\Omega_{e,D,F}$ at a time, the difference is then divided by the maximum and multiplied by 100 (Equation 5.1), to express it as a percentage. This is done for each of the sizes and opposition angle, the wanted value is the average over ϕ (Equation 5.2).

$$\delta_{max,D}(\phi) = \frac{\max(\Omega_{e,D,F}(\phi)) - \Omega_{e,D,F}(\phi)}{\max(\Omega_{e,D,F}(\phi))} * 100 \tag{5.1}$$

$$\delta_{max,D} = \langle \delta_{max,D}(\phi) \rangle \tag{5.2}$$

Having the values of $\delta_{max,D}$, it is necessary to establish a tolerance limit error, usually a 10% of tolerance is acceptable. In this way an unique filter can be chosen for every D "independently" of its ϕ (see the last row of Table 5.2). The objects sizes ($D \leqslant 0.7$ km) for which δ_{max} is greater than the tolerance, have values between $10 < \delta_{max} < 35\%$ for the F1 filter. The deviation is too big for these objects to consider using only 1 filter even if δ_{max} for this filter gives the minimum possi-

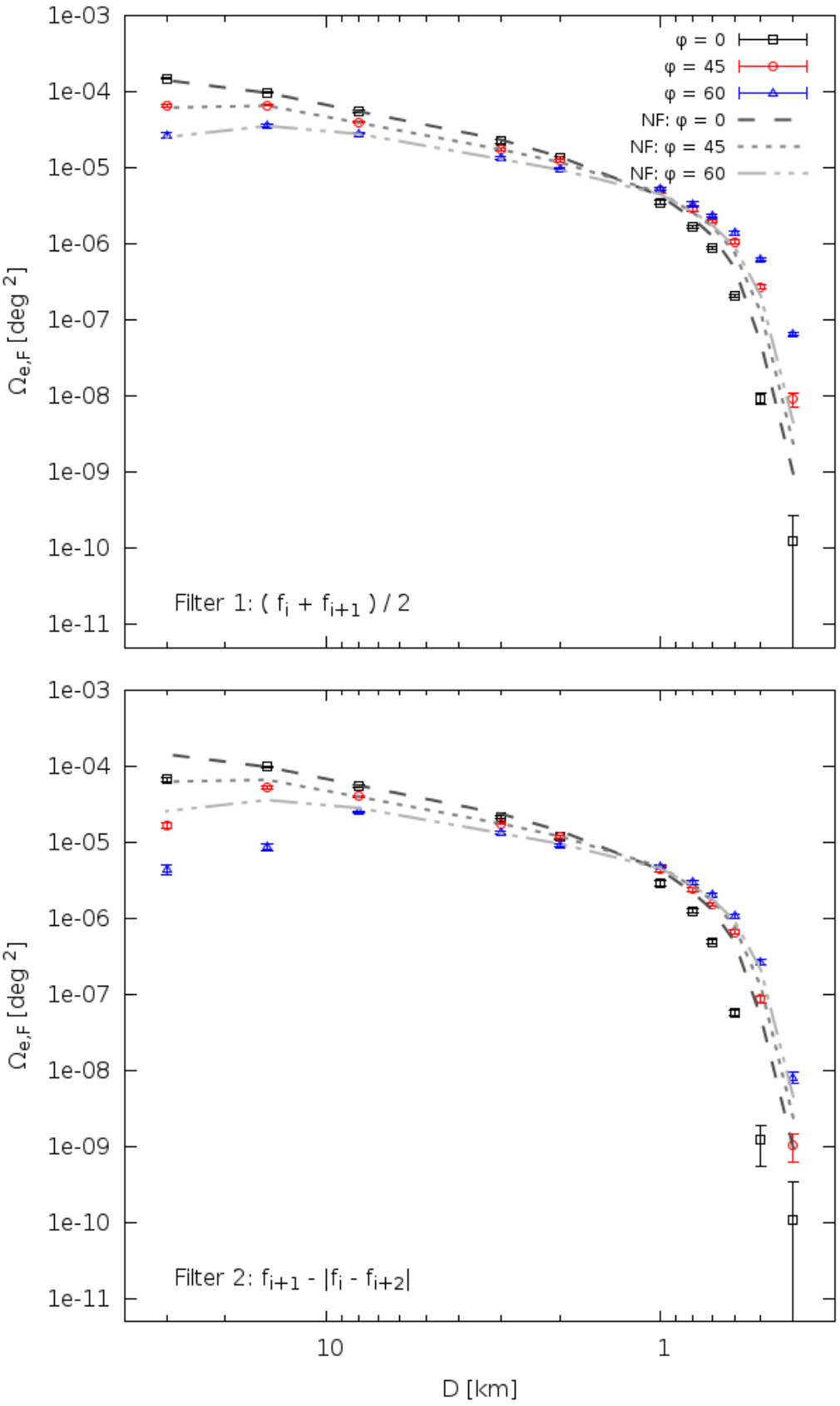

Figure 5.5: Object size, D, vs. effective solid angle, $\Omega_e(D, \phi)$, plot. The top panel corresponds to the filter 1 and the bottom one to filter 2, as labeled, where the black square symbols are the values for the $\phi = 0^o$, the red circles for $\phi = 45^o$ and the blue triangle for $\phi = 60^o$.

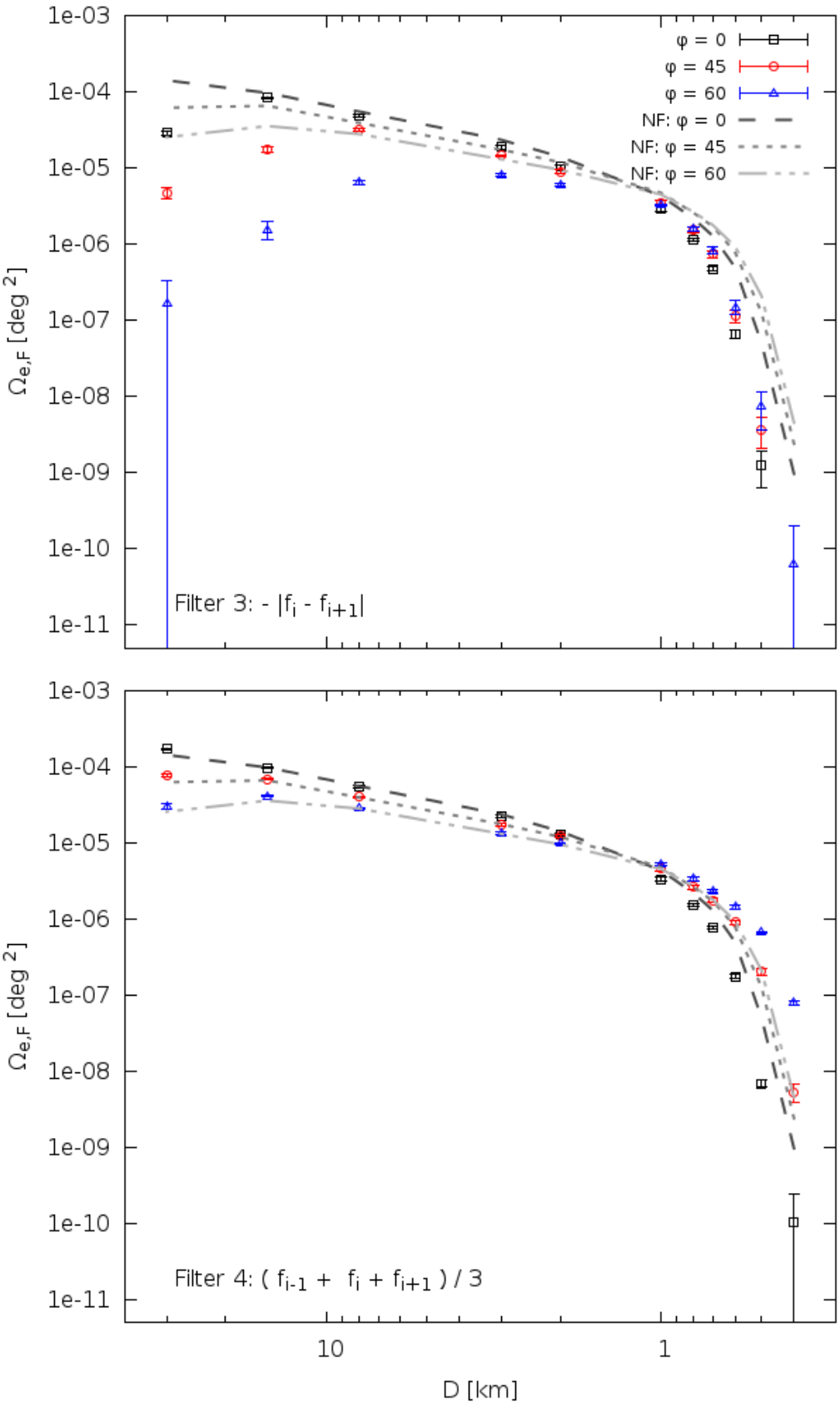

Figure 5.6: D vs. $\Omega_e(D, \phi)$ plot. The top panel corresponds to the filter 3 and the bottom one to filter 4. Notation as Figure 5.5.

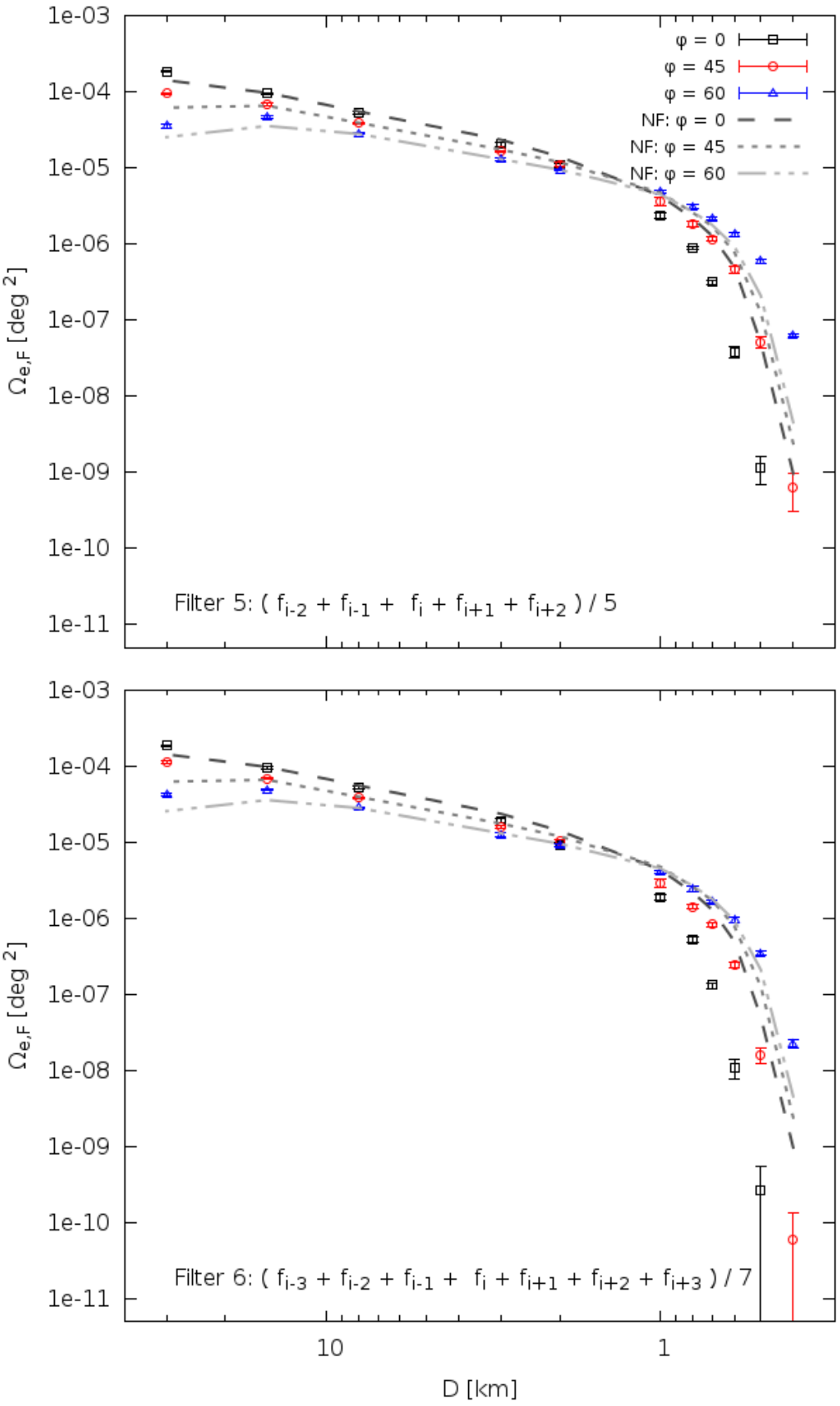

Figure 5.7: D vs. $\Omega_e(D, \phi)$ plot. The top panel corresponds to the filter 5 and the bottom one to filter 6. Notation as Figure 5.5.

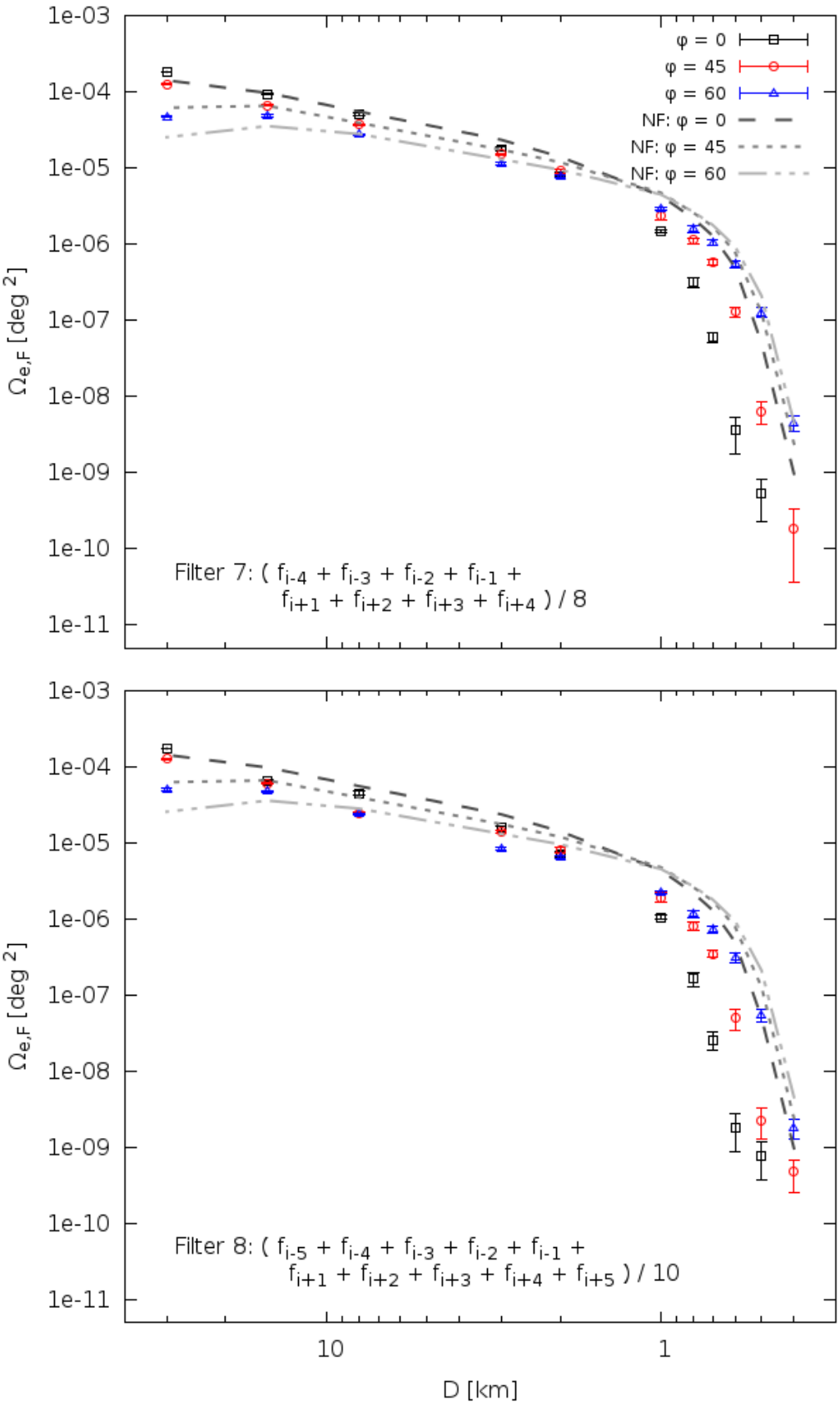

Figure 5.8: D vs. $\Omega_e(D, \phi)$ plot. The top panel corresponds to the filter 7 and the bottom one to filter 8. Notation as Figure 5.5.

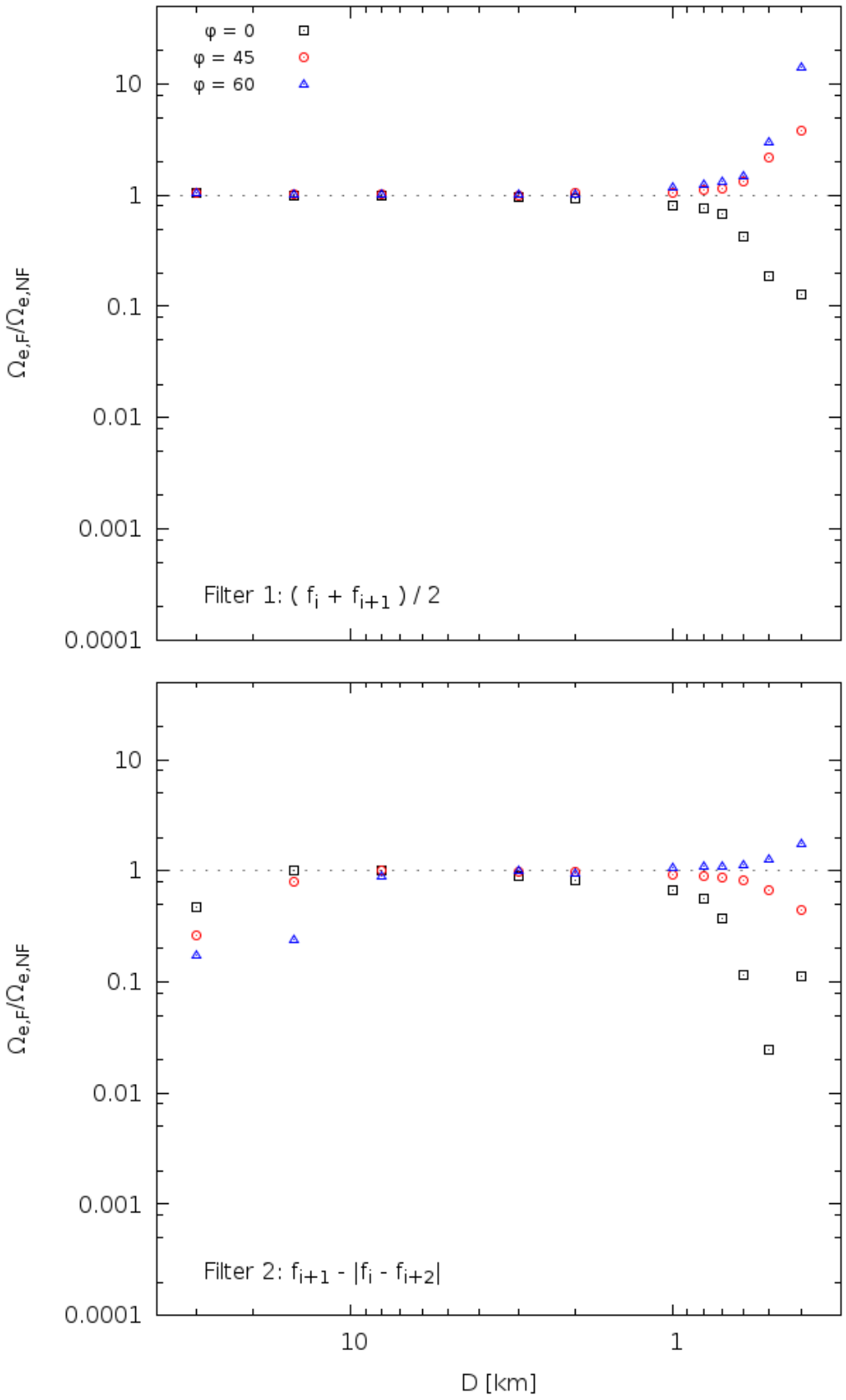

Figure 5.9: D vs. $\Omega_e(D, \phi)$ plot. The top panel corresponds to the filter 1 and the bottom one to filter 2, as labeled, where the black square symbols are the values for the $\phi = 0^o$, the red circles for $\phi = 45^o$ and the blue triangle for $\phi = 60^o$.

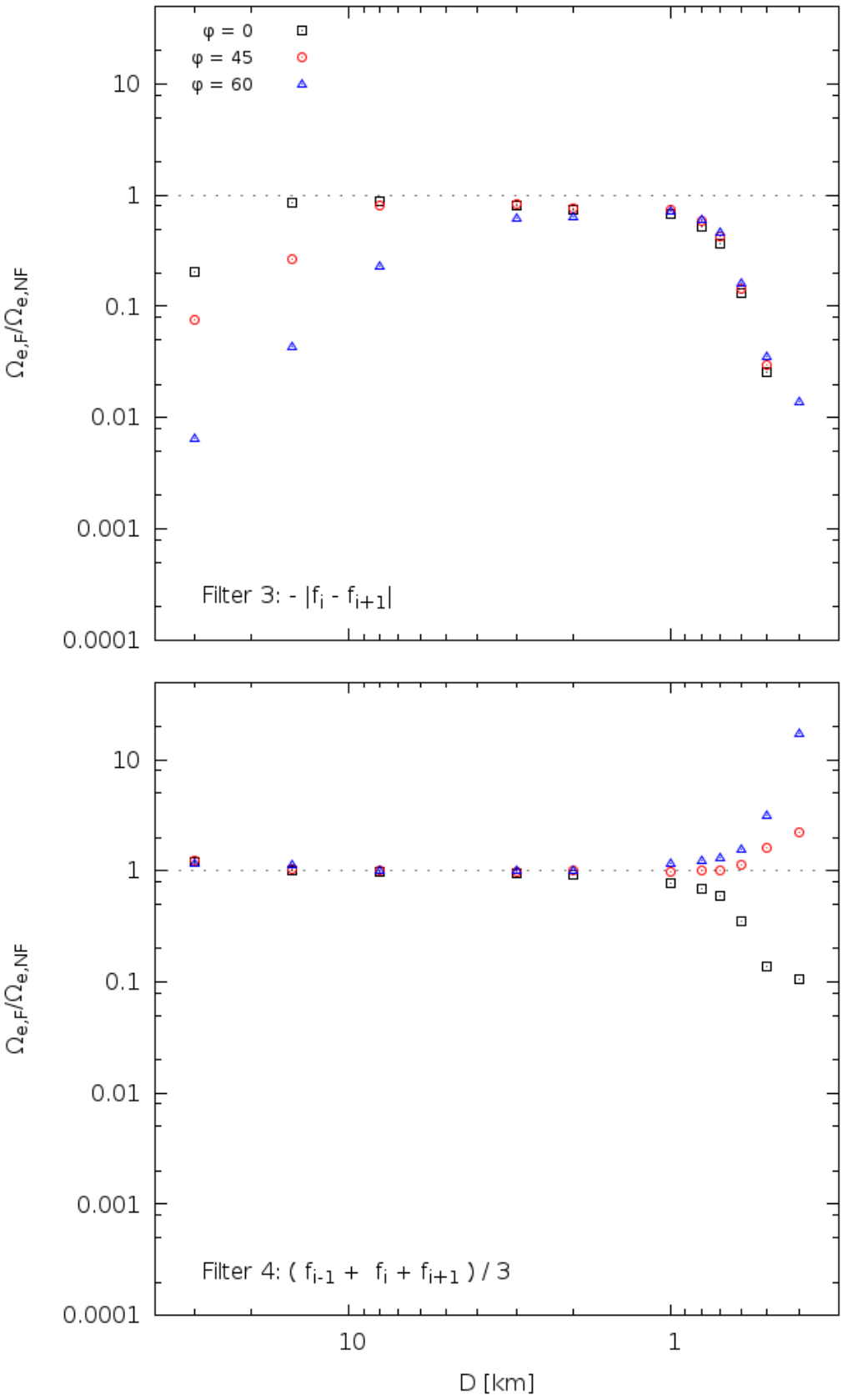

Figure 5.10: D vs. $\Omega_e(D, \phi)$ plot. The top panel corresponds to the filter 3 and the bottom one to filter 4. Notation as Figure 5.9.

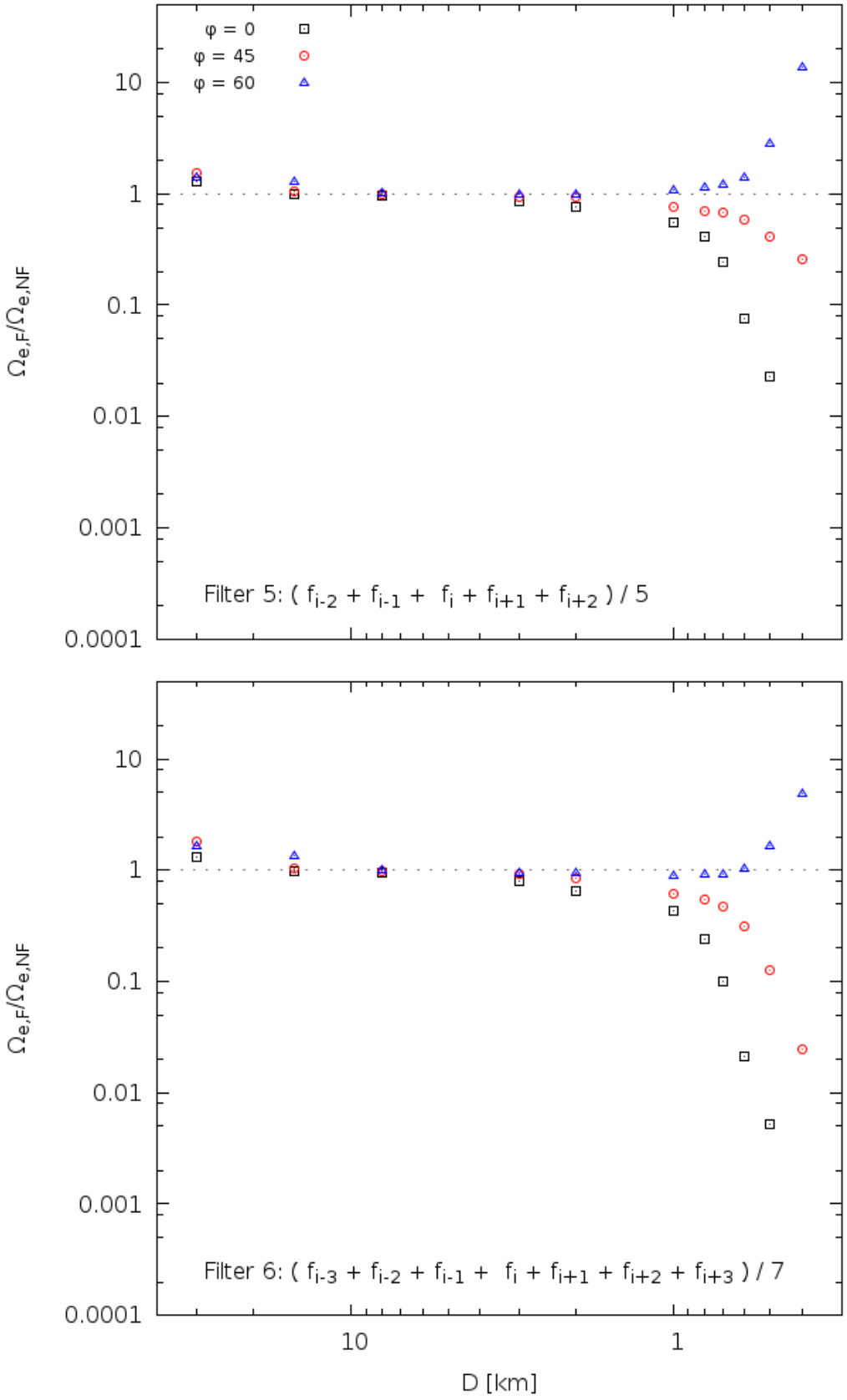

Figure 5.11: D vs. $\Omega_e(D, \phi)$ plot. The top panel corresponds to the filter 5 and the bottom one to filter 6. Notation as Figure 5.9.

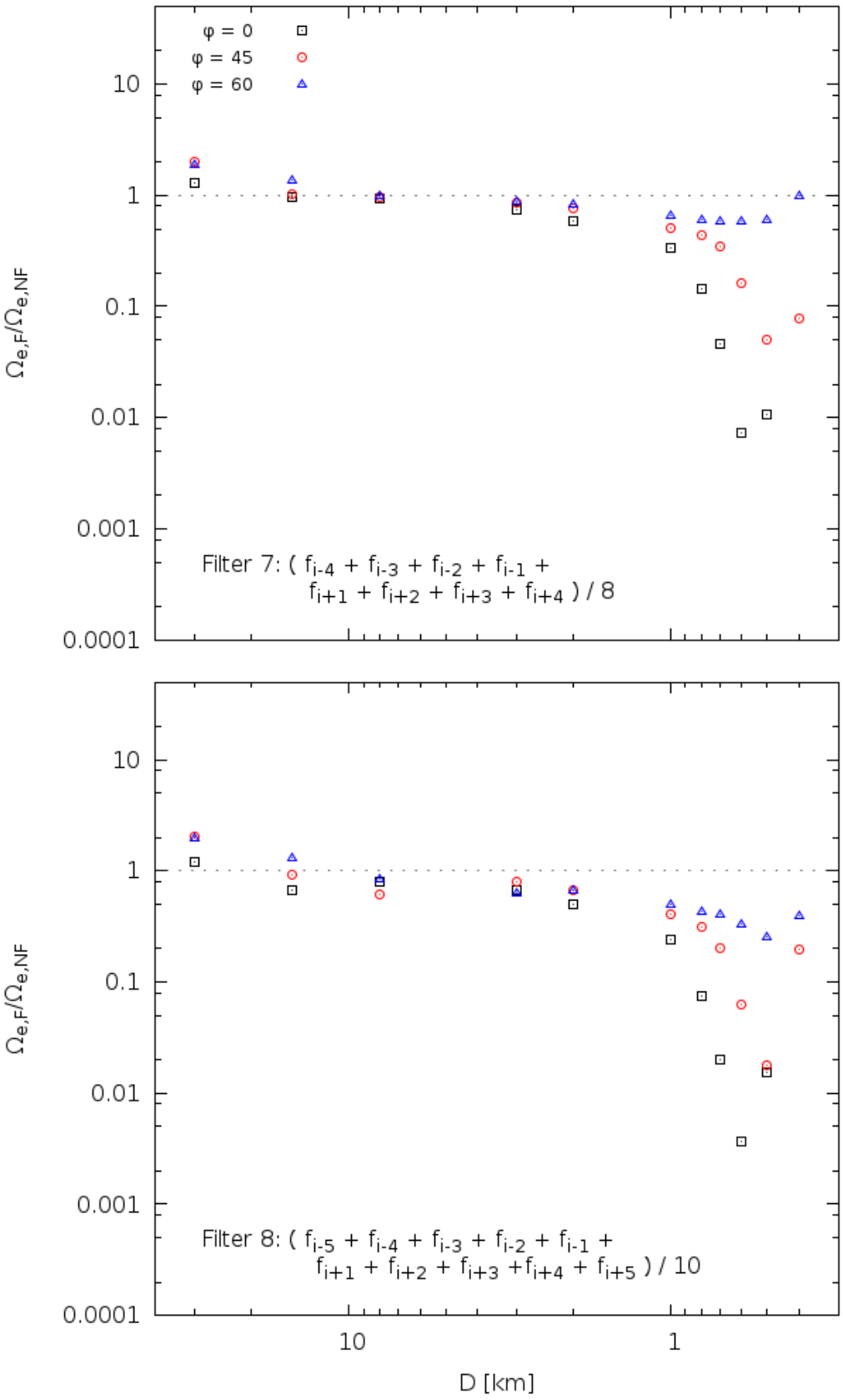

Figure 5.12: D vs. $\Omega_e(D, \phi)$ plot. The top panel corresponds to the filter 7 and the bottom one to filter 8. Notation as Figure 5.9.

ble value.

ϕ [°]\D [km]	0.4	0.5	0.6	0.7	0.8	1	2	3	8	15	30
0	NF	NF	NF	NF	NF	NF	NF	NF	NF	F2	F5 or F6
45	F1	F1	F1	F1	F1	F1	F1	F1	F2	F4	F8
60	F4	F4	F4	F1	F1	F1	F1	F1	F4	F6	F8
$\delta_{max} < 10\%$	-	-	-	-	F1	F1	F1	NF	F1	F6	F8

Table 5.2: Filters that maximize $\Omega_e(D, \phi)$.

If there is not necessity of having an unique filter per object size, the filters shown in Table 5.2 will be more than sufficient to increase significantly the efficiency of detection.

5.2.1 *Signal-to-noise ratio histograms.*

In order to exclude, in the future, stars which do not provide enough sensitivity to occultation events and that contribute to the total number of lightcurves, we carried out a study of how many events where recovered with certain SNR for a specific object size and opposition angle (being b and t_{off} random values).

	TOTAL FIELD STARS	FIELD STARS $m \leqslant 14.2$
NO.	3245	1322
MAX. SNR	76.95	76.95
MIN. SNR	2.74	7.77

Table 5.3: Summary of the F0V stars contained in the TAOS field catalog and the number of stars with mag < 14.2.

The code `SNRhist.py` was written to analyze the behavior of SNR of recovered events, it reads the SNR data from the output file[2] in step 9 of Section 4.2 and calculates the necessary information to construct a SNR histogram for a certain combination of D and ϕ. Giving as a result an output file (in table form) with the binned SNR and its corresponding recovered objects number. Afterwards the

2 Recovered light curves output file.

histograms where plotted as shown in Figure 5.14, 5.15 and 5.16.

The minimum bin of SNR for big objects is ~ 7, which is the approximate value of SNR that corresponds to the restriction in stellar magnitude ($m \leqslant 14.2$) given to the recovery code. As summarized in Table 5.3, the number of stars in the chosen TAOS field is of 3245, in contrast, the amount of stars in the field with $m \leqslant 14.2$ is 1322 that represent less than half of the stars in the field.

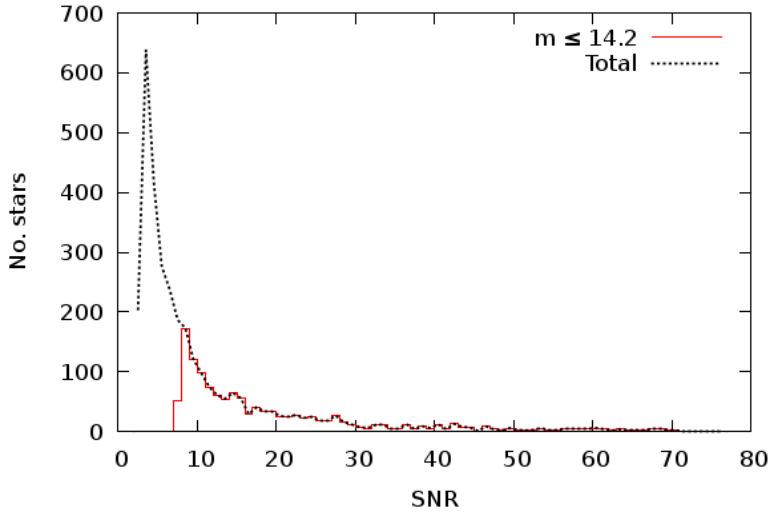

Figure 5.13: SNR distribution for the TAOS star field chosen.

The SNR distribution shown in Figure 5.14 and 5.15 for objects with $D > 1$ km, reflects the distribution corresponding to the chosen field of stars, which evidently has a greater amount of stars with $SNR < 10$ ($m > 13.83$), see Figure 5.13.

For objects with $D \leqslant 1$ km the minimum SNR value increases, the same happens when the opposition angle decreases or tends to zero. In such a way that, for example, for objects of $D = 0.5$ km the inferior limit of the SNR for $\phi = 60$ is 21, and for $\phi = 0$, 32. On the other hand, it seems that the SNR distribution for objects with $D > 1$ km is independent of the opposition angle as summarized in Table 5.4. As happens with the SNR inferior limit, the value of SNR where the maximum amount of lightcurves occurs is shifted to greater values, specially for objects with $D \lesssim 1$ km (see Table 5.4).

D [KM]	SNR PEAK			SNR INFERIOR LIMIT		
	$\phi = 60$	$\phi = 45$	$\phi = 0$	$\phi = 60$	$\phi = 45$	$\phi = 0$
30	8	8	8	7	7	7
15	8	8	8	7	7	7
8	8	8	8	7	7	7
3	8	8	8	7	7	7
2	8	8	9	7	7	7
1	15	18	27	7	8	12
0.8	22	27	42	9	13	14
0.7	27	27	43	12	15	19
0.6	42	42	57	15	21	24
0.5	46	57	57	21	26	32
0.4	57	63	60	27		

Table 5.4: SNR peak (the value of SNR with higher event recovered) and SNR inferior limit in function of the size and the opposition angle. As it can be seen, the peak shifts to greater values as the object size decreases, as well as the opposition angle decreases.

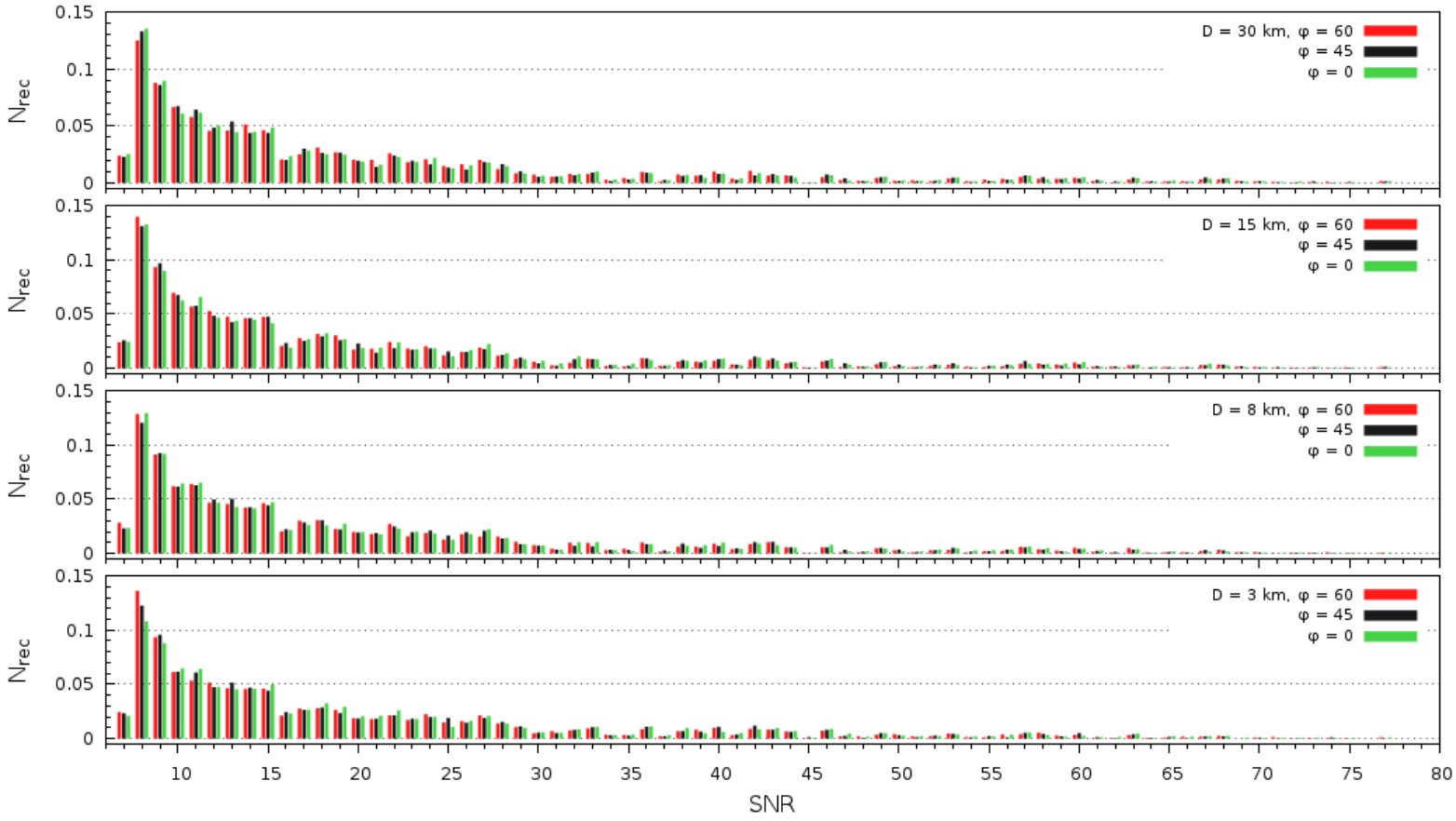

Figure 5.14: SNR histogram for objects of D = 30, 15, 8 & 3 km

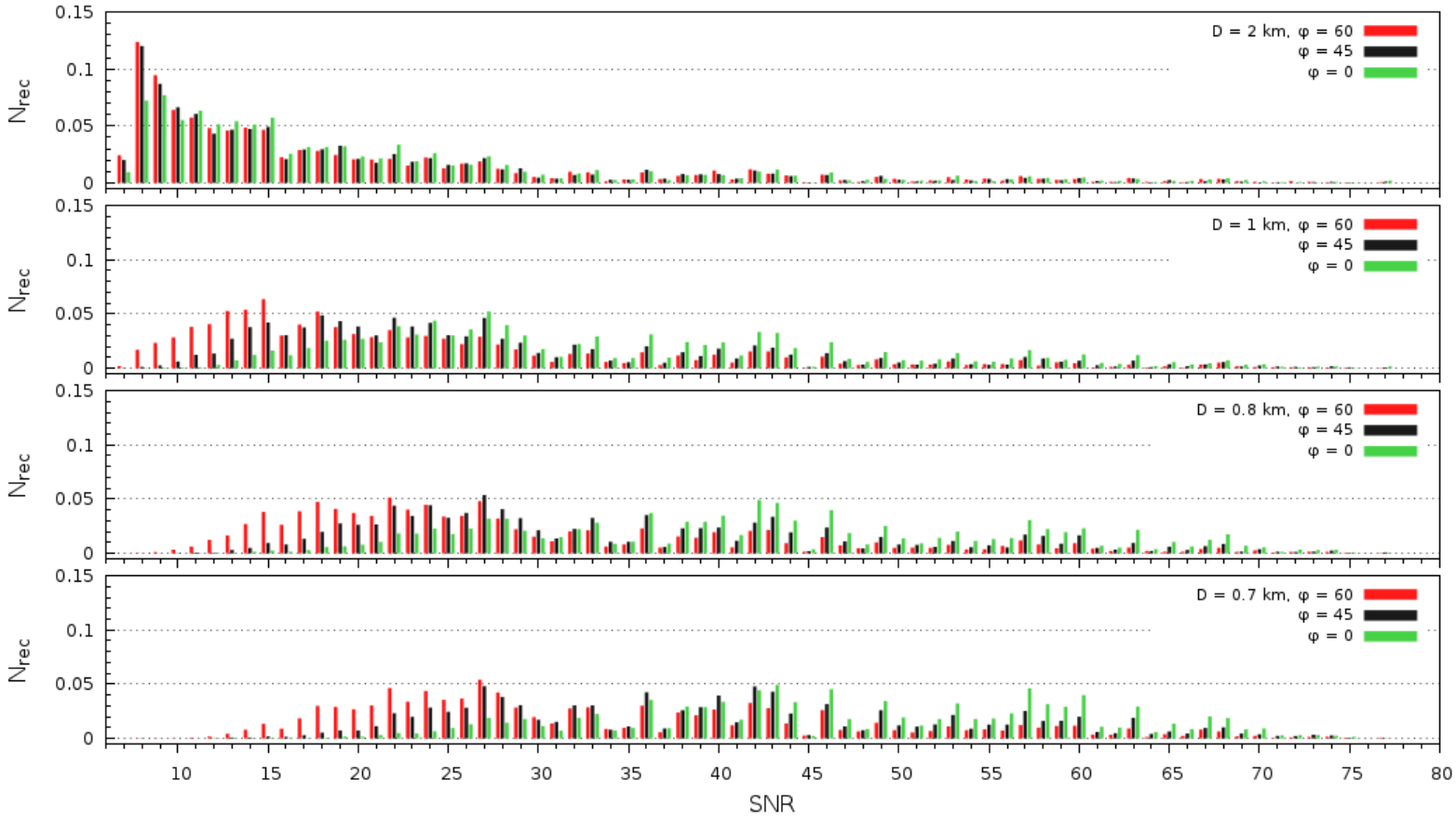

Figure 5.15: SNR histogram for objects of D = 2, 1, 0.8 & 0.7 km

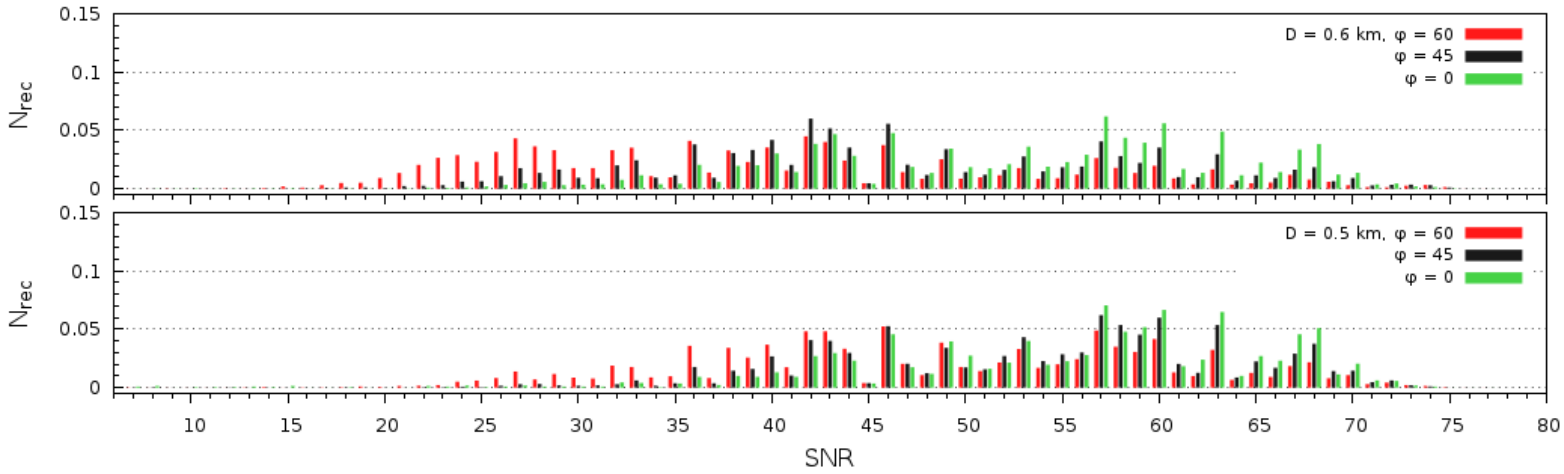

Figure 5.16: SNR histogram for objects of D = 0.6 & 0.5 km

5.2.2 *Effective solid angle of a combination of filters.*

This could be considered a by-product of the filtering process. It was done to have a comparison with the results of Zhang et al. (2013), who also used filters to improve the significance of any candidate event given that the rank product statistic described by Lehner et al. (2010) has the disadvantage of being inefficient at detecting longer duration occultation events. The study of Zhang et al. (2013) includes the estimation of the effective solid angle of combinations of two filters based on the fact that more than one filter[3] can detect the same event.

A new program was written, `fil_comb_rec.py`, to conduct the combination of filters by pairs from a sample of them. We chosen Fo = NF, F1, F4, F5, F6, F7 and F8, giving as a result 21 unique combinations. Once the combinations are determined, it reads the file, as example, `all_d30.0km_60grad.dat` (in step 10 of Section 4.2) and searches the corresponding columns for each filter in the pair with the purpose of finding the number of occurrences of p-value $< 5 \times 10^{-12}$ without discriminating whether it occurs in one or both of the filters. The threshold p-value had to be reduced a factor of 2 because we have to treat each filter as independent test, and the false positive rate would double otherwise (Lehner et al., 2010). Finally, `fil_comb_rec.py` calculates the $\Omega_{e,FF'}$, the sub-index FF' refers to the combination of the two different filters. The same procedure is repeated for each of the combinations as well as each object size and opposition angle.

In Figures 5.17, 5.18, 5.19, 5.20 and 5.21 we plot the effective solid angle for the combination of filters (each one properly labeled) normalized by the Fo & F1 combination. Zhang et al. (2013) concluded that the best combination of filters was the equivalent to Fo & F1. We plot the ratio of each combination with the Fo & F1 pair to determine easily the advantages or disadvantages of each pair.

Our selection criteria for the filter combinations are very similar to that used by Zhang et al. (2013). We focus on two of the three criteria of Zhang et al. (2013), 1) maximize the sensitivity at D = 1 km and 2) maximize the sensitivity at D = 30 km, in order to bring, as Zhang et al. (2013) explain, the upper limit as close as possible to the current detection limits. The calculated effective solid angles of the 1-km and 30-km objects, for the different combinations of filters we considered, are presented in Table 5.6 and 5.7.

In Tables 5.6 and 5.7, the values marked with an asterisk denote the maximum value of $\Omega_{e,FF'}$. The deviation to maximum (Equation 5.1 and 5.2) is also applied to help determine a unique filter that includes all the opposition angles (last column

3 Considering filters with a different amount of points taken into account (window size).

of the tables). From this we obtain as the best pair of filters for the 1-km object, the Fo & F1 pair, and for the 30-km object, the F6 & F8 pair.

ϕ [°]\D [km]	1	30
		F1 & F6
0	NF & F1	F1 & F7
		F1 & F8
45	NF & F1	F1 & F8
60	F1 & F6	F6 & F8

Table 5.5: Combination of filters that maximizes $\Omega_e(D, \phi)$ in function of ϕ for object sizes $D = 1$ & 30. The δ_{max} was not considered in the selection of these filters.

F & F′	$\Omega_{e,FF'}(\phi = 0)$	$\Omega_{e,FF'}(\phi = 45)$	$\Omega_{e,FF'}(\phi = 60)$	δ_{max} [%]
Fo & F1	*4.560×10^{-6}	*5.550×10^{-6}	5.371×10^{-6}	1.07
Fo & F4	4.459×10^{-6}	5.276×10^{-6}	5.374×10^{-6}	3.44
Fo & F5	4.297×10^{-6}	4.836×10^{-6}	5.287×10^{-6}	7.78
Fo & F6	4.229×10^{-6}	4.718×10^{-6}	4.823×10^{-6}	11.79
Fo & F7	4.201×10^{-6}	4.659×10^{-6}	4.435×10^{-6}	14.67
Fo & F8	4.185×10^{-6}	4.638×10^{-6}	4.393×10^{-6}	15.17
F1 & F4	3.519×10^{-6}	5.004×10^{-6}	5.415×10^{-6}	11.70
F1 & F5	3.422×10^{-6}	4.941×10^{-6}	*5.550×10^{-6}	11.98
F1 & F6	3.409×10^{-6}	4.920×10^{-6}	5.314×10^{-6}	13.61
F1 & F7	3.406×10^{-6}	4.912×10^{-6}	5.156×10^{-6}	14.63
F1 & F8	3.405×10^{-6}	4.909×10^{-6}	5.149×10^{-6}	14.69
F4 & F5	3.210×10^{-6}	4.565×10^{-6}	5.385×10^{-6}	16.77
F4 & F6	3.201×10^{-6}	4.550×10^{-6}	5.216×10^{-6}	17.95
F4 & F7	3.198×10^{-6}	4.545×10^{-6}	5.138×10^{-6}	18.47
F4 & F8	3.197×10^{-6}	4.544×10^{-6}	5.134×10^{-6}	18.50
F5 & F6	2.318×10^{-6}	3.495×10^{-6}	4.813×10^{-6}	33.16
F5 & F7	2.313×10^{-6}	3.485×10^{-6}	4.790×10^{-6}	33.40
F5 & F8	2.313×10^{-6}	3.481×10^{-6}	4.790×10^{-6}	33.42
F6 & F7	1.787×10^{-6}	2.781×10^{-6}	3.993×10^{-6}	46.25
F6 & F8	1.788×10^{-6}	2.781×10^{-6}	3.994×10^{-6}	46.24

TABLE 5.6 CONTINUED IN NEXT PAGE...

F & F′	$\Omega_{e,FF'}(\phi = 0)$	$\Omega_{e,FF'}(\phi = 45)$	$\Omega_{e,FF'}(\phi = 60)$	δ_{max} [%]
F7 & F8	1.388×10^{-6}	2.323×10^{-6}	2.694×10^{-6}	59.72

Table 5.6: Effective solid angle for the 1-km object, taking into account the combination of filters (column 1), and the different opposition angles (column 2 through 4). Marked with an asterisk is the maximum $\Omega_{e,FF'}$ per opposition angle. In the last column are the values of δ_{max}.

F & F′	$\Omega_{e,FF'}(\phi = 0)$	$\Omega_{e,FF'}(\phi = 45)$	$\Omega_{e,FF'}(\phi = 60)$	δ_{max} [%]
Fo & F1	1.417×10^{-4}	6.345×10^{-5}	2.612×10^{-5}	41.07
Fo & F4	1.617×10^{-4}	7.051×10^{-5}	2.826×10^{-5}	34.27
Fo & F5	1.822×10^{-4}	8.703×10^{-5}	3.266×10^{-5}	23.46
Fo & F6	1.854×10^{-4}	1.045×10^{-4}	3.859×10^{-5}	14.50
Fo & F7	1.851×10^{-4}	1.209×10^{-4}	4.339×10^{-5}	7.20
Fo & F8	1.851×10^{-4}	1.304×10^{-4}	4.638×10^{-5}	2.80
F1 & F4	1.595×10^{-4}	6.754×10^{-5}	2.670×10^{-5}	36.45
F1 & F5	1.823×10^{-4}	8.635×10^{-5}	3.236×10^{-5}	23.82
F1 & F6	$*1.858 \times 10^{-4}$	1.045×10^{-4}	3.853×10^{-5}	14.47
F1 & F7	$*1.858 \times 10^{-4}$	1.215×10^{-4}	4.354×10^{-5}	6.82
F1 & F8	$*1.858 \times 10^{-4}$	$*1.312 \times 10^{-4}$	4.673×10^{-5}	2.24
F4 & F5	1.825×10^{-4}	8.797×10^{-5}	3.279×10^{-5}	23.08
F4 & F6	1.855×10^{-4}	1.057×10^{-4}	3.892×10^{-5}	13.96
F4 & F7	1.855×10^{-4}	1.221×10^{-4}	4.406×10^{-5}	6.38
F4 & F8	1.855×10^{-4}	1.311×10^{-4}	4.739×10^{-5}	1.87
F5 & F6	1.849×10^{-4}	1.068×10^{-4}	3.925×10^{-5}	13.59
F5 & F7	1.849×10^{-4}	1.228×10^{-4}	4.524×10^{-5}	5.53
F5 & F8	1.849×10^{-4}	1.309×10^{-4}	4.826×10^{-5}	1.46
F6 & F7	1.840×10^{-4}	1.230×10^{-4}	4.587×10^{-5}	5.21
F6 & F8	1.840×10^{-4}	1.306×10^{-4}	$*5.010 \times 10^{-5}$	0.46
F7 & F8	1.818×10^{-4}	1.299×10^{-4}	4.874×10^{-5}	1.95

Table 5.7: Same as Table 5.6 for a 30-km object.

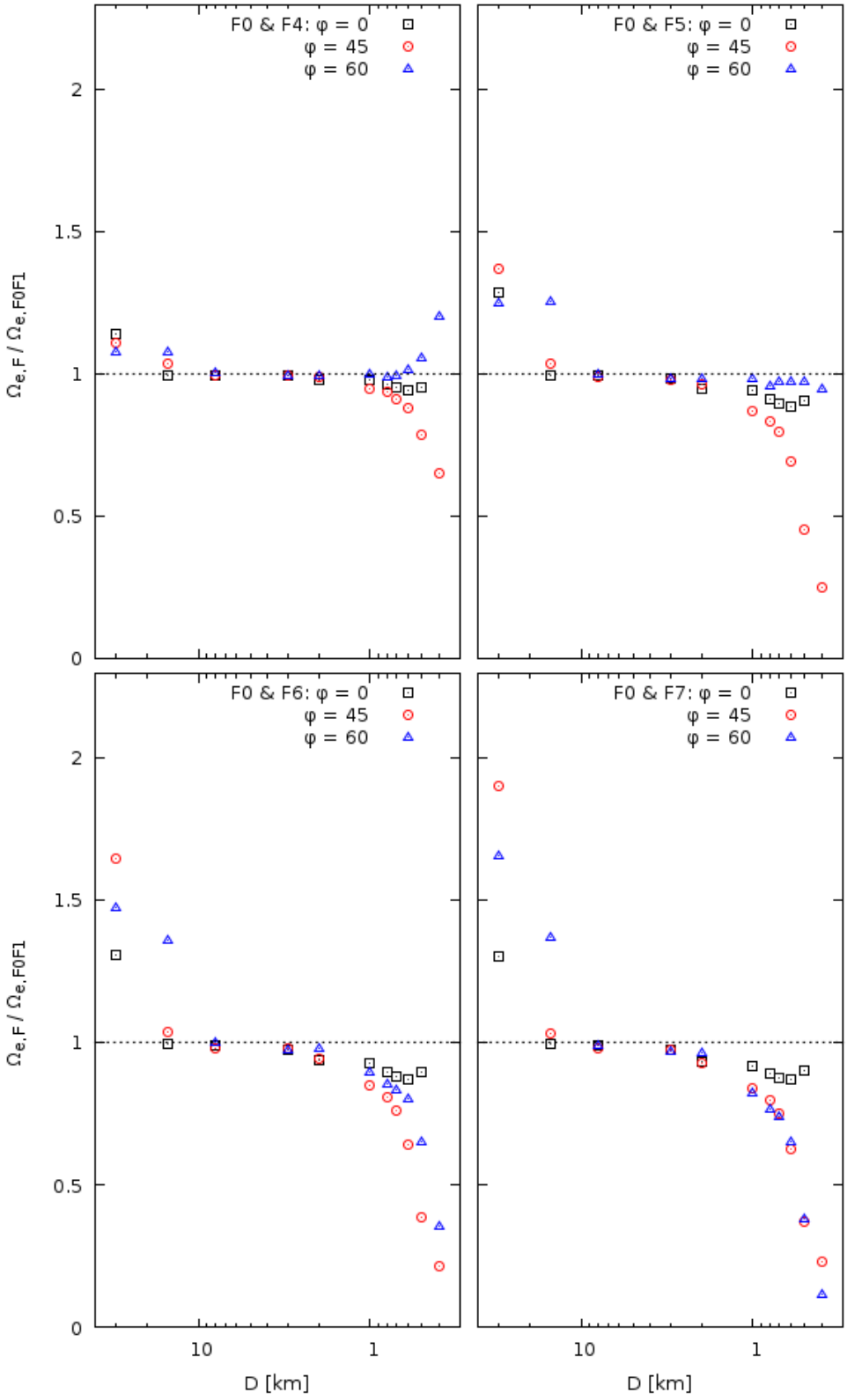

Figure 5.17: Ratio of the effective solid angle for the combinations of filters, $\Omega_{e,FF'}(D,\phi)$, and the corresponding quantity for the Fo & F1 pair. Each color-shape corresponds to different opposition angle, ϕ, black-squares: $\phi = 0$, red-circles: $\phi = 45$ and blue-triangles: $\phi = 60$. Top left: Fo & F4 pair; top right: Fo & F5 pair; bottom left: Fo & F6 pair; bottom right: Fo & F7 pair.

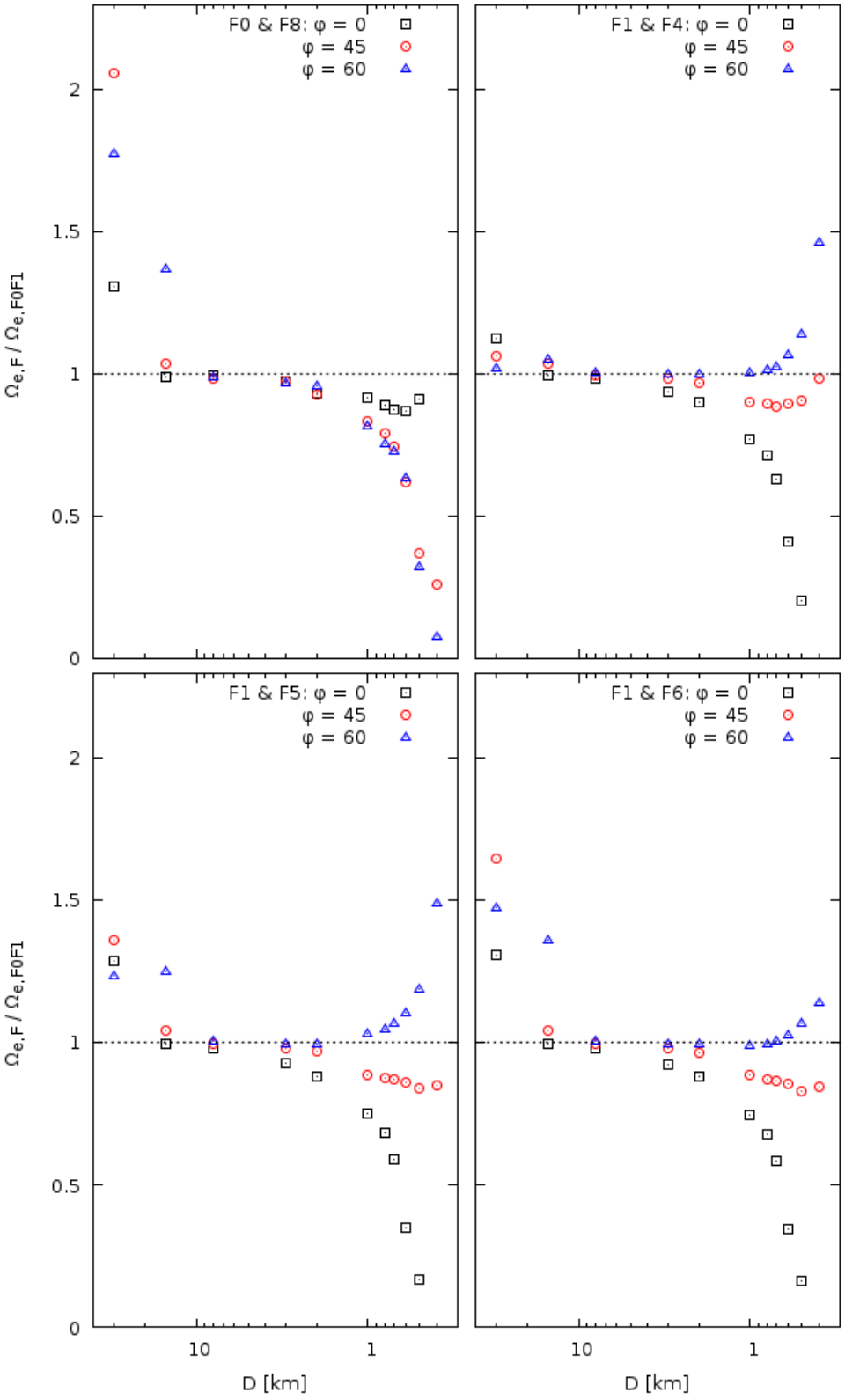

Figure 5.18: $\Omega_{e,F\,F'}(D,\phi)$, weighted by F0 & F1 combination. Same notation as Figure 5.17. Top left: F0 & F8 pair; top right: F1 & F4 pair; bottom left: F1 & F5 pair; bottom right: F1 & F6 pair.

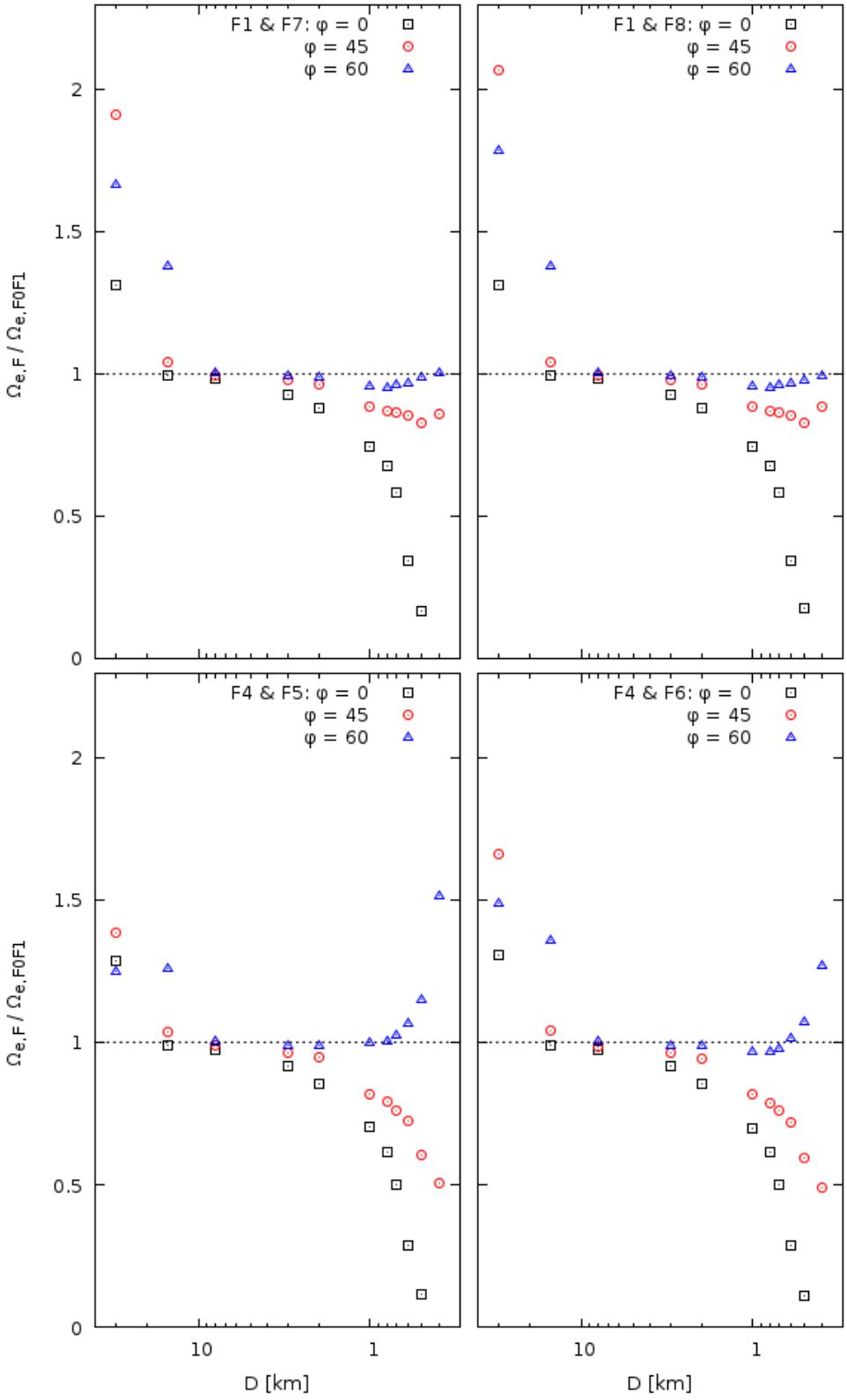

Figure 5.19: $\Omega_{e,F\,F'}(D,\phi)$, weighted by F0 & F1 combination. Same notation as Figure 5.17. Top left: F1 & F7 pair; top right: F1 & F8 pair; bottom left: F4 & F5 pair; bottom right: F4 & F6 pair.

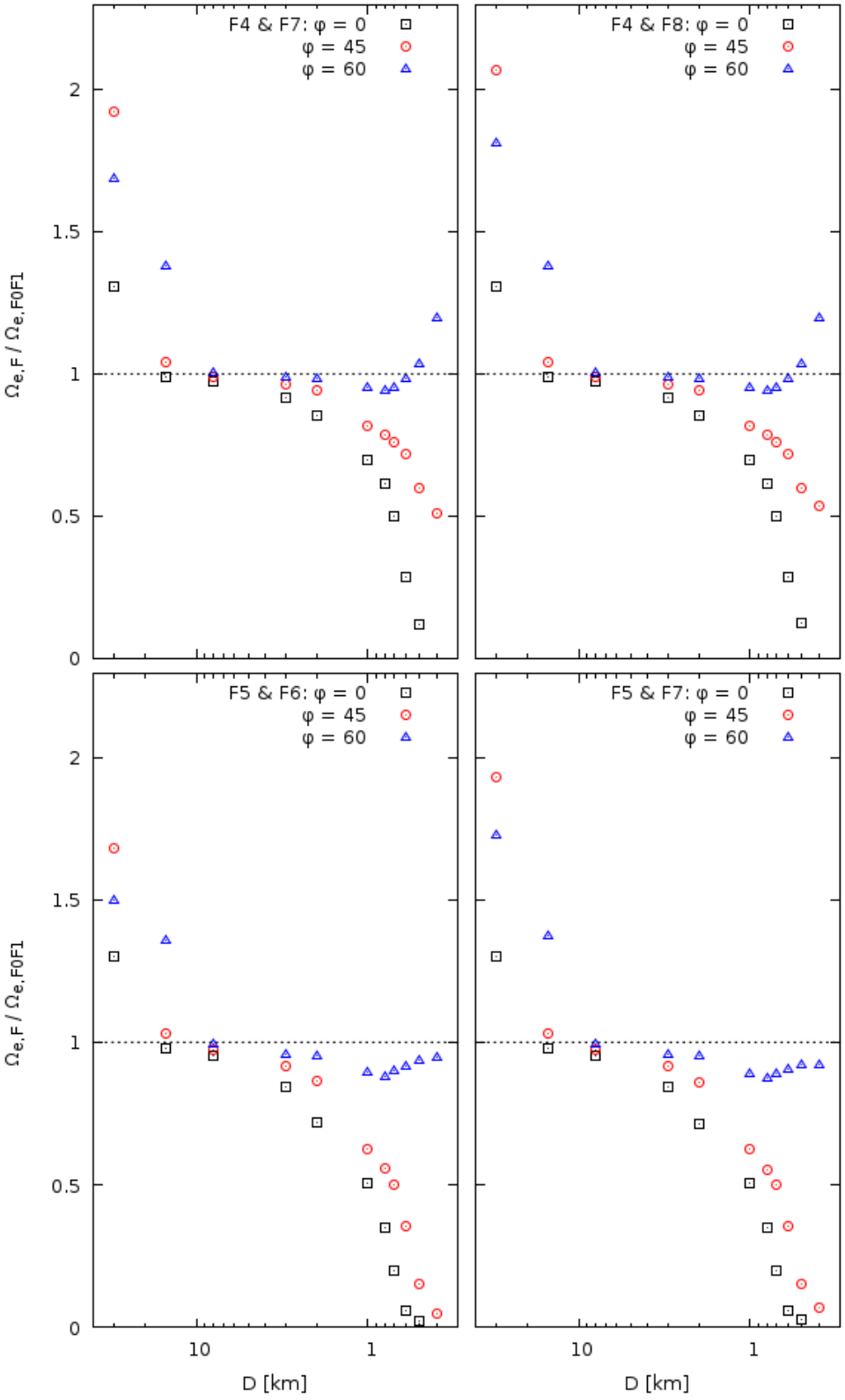

Figure 5.20: $\Omega_{e,F\,F'}(D,\phi)$, weighted by Fo & F1 combination. Same notation as Figure 5.17. Top left: F4 & F7 pair; top right: F4 & F8 pair; bottom left: F5 & F6 pair; bottom right: F5 & F7 pair.

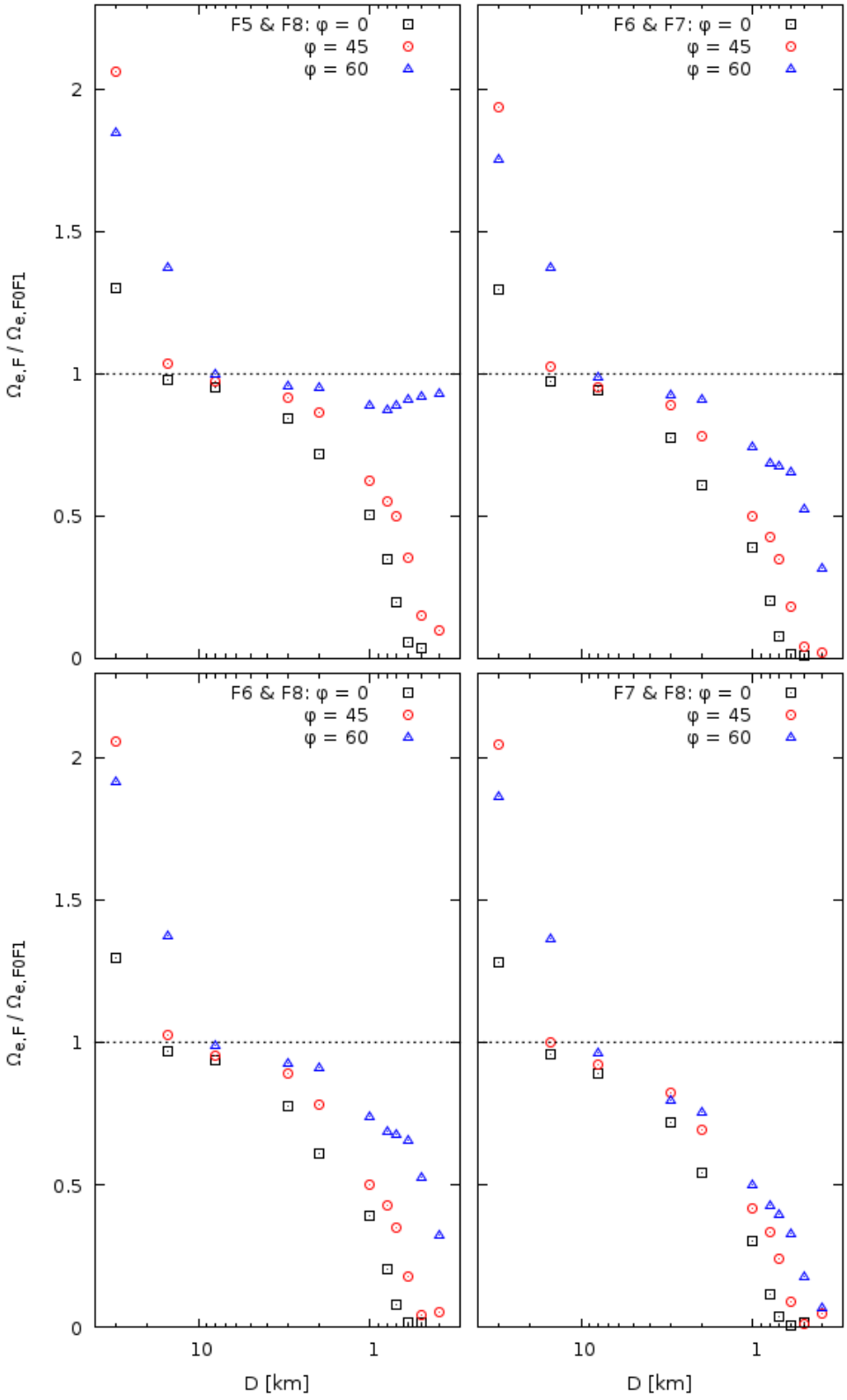

Figure 5.21: $\Omega_{e,F\,F'}(D,\phi)$, weighted by F0 & F1 combination. Same notation as Figure 5.17. Top left: F5 & F8 pair; top right: F6 & F7 pair; bottom left: F6 & F8 pair; bottom right: F7 & F8 pair.

6

Discussion and Conclusions.

Lightcurves of stellar occultations by KBOs were simulated and analyzed for the TAOS I project, with a sampling rate of 10 Hz. The main purposes our work were:

1. To study if there would be an improvement in the occultation detection efficiency as a resultf of the increased sampling rate, in comparison with measurements with the previous sampling frequency of TAOS I project, 5 Hz.

2. If the use of algebraic filters on the lightcurve data would increase the detection efficiency for the 10 Hz sampling frequency.

An improvement in the detection efficiency was expected, given that the number of observed points in the lightcurve is increased by a factor of two as we increase the sampling frequency, but it was not clear by how much. In addition to the detection efficiency we also obtained the effective solid angle, $\Omega_e(D)$ for the TAOS I project, a survey-dependent quantity.

The lightcurves were simulated with a set of codes written by the TAOS team, based on the calculations of Nihei et al. (2007), which handle among other things, the creation and finite sampling of the occultation lightcurves, considering also the effect of diffraction in function of parameters that vary with the observations and the inclusion of the expected observational random noise. The shape of a diffraction lightcurve depends mostly on three parameters: the size of the body, the distance of the object to Earth and the brightness of the source star, which can be related to its apparent angular size and its apparent magnitude. The simulation of the observational lightcurve depends, besides the diffraction, on when (time offset, t_{off}) and where (impact parameter, b) the event is observed with respect to the center of the diffraction pattern in time and space. Certainly, it is not the same to observe the occultation event in the middle of the shadow of the diffraction pattern ($b = 0$ km and $t_{off} = 0$ s) than at the edge of the pattern, in the latter case the flux drop will be smaller and probably the event could be confused with the background noise.

The simulations carried out in this thesis were divided into two stages which had in common the KBO distance to Earth, $\Delta = 43$ AU. The first stage considered systematic variations of: object size, D, apparent stellar magnitude, M_*, and spectral type, impact parameter, b, and time offset, t_{off}. Such stage can be considered

as a descriptive study of the behavior of the $p-value$ given the mentioned parameters and can be observed in the form of probability color maps (Figure 5.1 to 5.3). The second part was an attempt to estimate the recovery efficiency of the survey by using random values of b, t_{off}, M_* and stellar angular size, θ_* and selecting those events whose $p-value$ where below the threshold ($p-value < 10^{-11}$) (Lehner et al., 2010). In such manner we obtained the survey detection efficiency and also the effective solid angle, $\Omega_e(D,\phi)$, which "measures" the improvement of the TAOS I project by sampling at 10 Hz in comparison with results from the 5 Hz sampling data. In the calculation of the Ω_e, we also considered the use of "filters", algebraic combination of flux values, with the main purpose of assessing whether it is possible that their use may increase the detection efficiency of a given event.

The probability color maps of Section 5.1 show the best conditions to maximize the number of detections of occultations. First, it is best to inspect stars with a small magnitude, i. e., a smaller angular size. These two conditions additionally depend on the size of the object desired to detect. Objects larger than the Fresnel scale (in this case $F = 1.39$ km) are easily detected in almost all cases, i. e., are independent of the luminosity and size characteristics of the star. If the object has a size $D \leqslant F$ its detection depends heavily on the characteristics of the star monitored. It should be noted that the spectral type in these cases is important only to the extent that it is related to the brightness and size of the star, which in turn corresponds to a given angular size.

It is important to establish how much the detection of KBOs increases making observations at a rate of 10 Hz. The detection efficiency, ϵ, is, basically, the ratio between the number of recovered lightcurves and the total simulated, this value is different for each combination of object size and opposition angle, ϕ. Previously this same study was performed for the TAOS I data with a cadence of 5 Hz (Zhang et al., 2013; Bianco et al., 2010; Zhang et al., 2008) in terms of the detection efficiency and the effective solid angle. By the only fact of changing the observational cadence, not taking into account the filtering, and comparing with the results of Zhang et al. (2013), we obtained an increment in the ability to detect occultation events measured by the quotient $\triangle\Omega_e(D) = \Omega_e(10\,\text{Hz}, D)/\Omega_e(5\,\text{Hz}, D)$ where D is given in kilometers, for three important sizes: $\triangle\Omega_e(30) \sim 3$, $\triangle\Omega_e(1) \sim 13$ and $\triangle\Omega_e(0.5) \sim 200$.

The procedure to study of detection efficiency which also allowed us to analyze the SNR distribution, is important to exclude the observation and/or simulation of stars which does not provide enough sensitivity to occultation events and that contribute to the total number of lightcurves. Objects with sizes $D \leqslant 1$ km would only be detected crossing in front of stars with high SNR. Depending on the ob-

ject size the inferior limit of SNR required could be as high as ~ 32. This effect is expected, as seen in the probability color maps, the event detection for these objects is almost impossible in stars with $m \gtrsim 11$. It was noted that the SNR value of the maximum peak in the SNR distribution, SNR value that has the maximum occurrence, shifts to larger values when the size of the object decreases (Table 5.4). For objects with $D > 1$ km, these peak and the entire SNR distribution matches the one of the sub-sample of TAOS field (stars with $m \leqslant 14.2$) (Figure 5.13), this could mean that their detection is only constrained, up to this point, by the limits in magnitude of the survey.

As commented before, the shape of the lightcurves depends on several parameters. Some lightcurves presented a flux drop involving more than one measurements, a multipoint flux drop. The fluxes of a multipoint drop could take the same rank, even considering random noise. This is a problem for the rank statistics because the $p-value$ gets less significative. Such is the case of the object of $D = 30$ km that is expected to be easily identified, meaning that it would have a significant $p-value$, but as the probability color maps showed, its mean $p-value$ is $\sim 10^{-10}$, one order of magnitude lower that the threshold.

Eight filters were designed and applied to the lightcurves with the purpose of dissipating the multipoint flux drop and, therefore, increase the detection probability. We calculated the corresponding Ω_e and compared these results to those obtained without filtering. Two of the filters, F2 & F3, involving absolute values, proved no significant increase on the detection of occultation events for any of the objects considered in this study ($\Omega_{e,F2}(D_i) < \Omega_{e,F0}(D_i)$ and $\Omega_{e,F3}(D_i) < \Omega_{e,F0}(D_i)$), as shown in Figure 5.9 and 5.10. The rest of the filters showed varying degrees of detection improvement in function of the object size and opposition angle, which involves that there is not a single filter that increments the detection of all object sizes at the same time (see Figure 5.9 to 5.12). But not only that, even considering single size objects, the best filter is not the same for different opposition angles. That is why we defined the "deviation to maximum" parameter, $\delta_{max}(D)$, to determine which filter is useful with a confidence of 90% for an object size regardless the opposition angle. The filter that accomplishes $\delta_{max} < 10\%$ for almost all the sizes is F1, except for $D = 3$, 15 & 30 km (Table 5.2). If we take the maximum value of $\Omega_e(D)$ among the 8 filters and obtain the quotient $\triangle Omega_e(D)$, as previously defined, we can see a clear improvement on the occultation event detection, with the application of the filters, at 10 Hz versus 5 Hz of $\triangle\Omega_e(30) \sim 4$, $\triangle\Omega_e(1) \sim 15$ and $\triangle\Omega_e(0.5) \sim 700$. This results encourage the future application of the present filters while reducing the observational data of TAOS I, sampling at 10 Hz, with the updated cameras.

Using the information of the recovered events for the different filters, a code to search for the joint detection of a given combination of filters (in pairs) was written, in such combinations the F2 & F3 filters were not included. Zhang et al. (2013) made a similar study for a cadence of 5 Hz and different filters, in that work was pointed out that it is necessary to reduce the threshold $p-value$ as a function of how many filters are combined together. For the present thesis, this implied the reduction of the original threshold $p-value$ in half, i. e., $p-value = 5\times10^{-12}$. The resulting effective solid angle was calculated and graphed in Figure 5.17 to 5.21. The effective solid angle was weighted by the Fo & F1 combination, which is the best combination of filters according to Zhang et al. (2013), so that the advantages of the other combinations are easily perceived. The best filter couple, again, depends on the object size and opposition angle, as done for a single filter, the deviation to maximum parameter was calculated for D = 1 & 30 km objects. The filter couple that minimized δ_{max} for those objects was chosen for that size. For the 1-km object, the filter pair which minimizes the value of δ_{max} is FO & F1, and F6 & F8, for the 30-km object. In order to fully compare these results with the ones of Zhang et al. (2013), it necessary to know the window size, w_s, of our filters. For Fo, F1, F6 and F8, the window size is $w_s = 1,\ 2,\ 8\ \&\ 10$ respectively. Our resulting pair of filters for the 1-km object is comparable with Zhang et al. (2013), in contrast, the window sizes of the selected pair for the 30-km object do not matches between them.

Bibliography

R. L. Allen, G. M. Bernstein & R. Malhotra (2001). *The Edge of the Solar System*. Astrophys. J., Lett., vol. 549: pp. L241–L244.

R. L. Allen, G. M. Bernstein & R. Malhotra (2002). *Observational Limits on a Distant Cold Kuiper Belt*. The Astron. J., vol. 124: pp. 2949–2954.

M. A. Barucci, H. Boehnhardt, D. P. Cruikshank & A. Morbidelli (2008a). *The Solar System Beyond Neptune*, chap. The Solar System Beyond Neptune: Overview and Perspectives. University of Arizona Press, (pp. 3–10).

M. A. Barucci, H. Boehnhardt, D. P. Cruikshank, A. Morbidelli & R. Dotson, eds. (2008b). *The Solar System Beyond Neptune*. University of Arizona Press.

G. M. Bernstein, D. E. Trilling, R. L. Allen, M. E. Brown, M. Holman & R. Malhotra (2004). *The Size Distribution of Trans-Neptunian Bodies*. The Astron. J., vol. 128: pp. 1364–1390.

F. B. Bianco, Z. W. Zhang, M. J. Lehner, S. Mondal, S. K. King, J. Giammarco, M. J. Holman, N. K. Coehlo, J. H. Wang, C. Alcock, T. Axelrod, Y. I. Byun, W. P. Chen, K. H. Cook, R. Dave, I. de Pater, D. W. Kim, T. Lee, H. C. Lin, J. J. Lissauer, S. L. Marshall, P. Protopapas, J. A. Rice, M. E. Schwamb, S. Y. Wang & C. Y. Wen (2010). *The TAOS Project: Upper Bounds on the Population of Small Kuiper Belt Objects and Tests of Models of Formation and Evolution of the Outer Solar System*. The Astron. J., vol. 139: pp. 1499–1514.

M. Born & E. Wolf (1980). *Principles of optics: Electromagnetic theory of propagation, interference and diffraction of light*. 6th edn. Pergamon Press.

M. E. Brown (2001). *The Inclination Distribution of the Kuiper Belt*. The Astron. J., vol. 121: pp. 2804–2814.

E. I. Chiang & M. E. Brown (1999). *Keck Pencil-Beam Survey for Faint Kuiper Belt Objects*. The Astron. J., vol. 118: pp. 1411–1422.

L. Dones, H. F. Levison, M. J. Duncan & P. R. Weissman (2004). *Simulations of the Formation of the Oort Cloud I. The Reference Model*.

M. Duncan, T. Quinn & S. Tremaine (1987). *The formation and extent of the solar system comet cloud*. aj, vol. 94: pp. 1330–1338.

M. J. Duncan & H. F. Levison (1997). *A scattered comet disk and the origin of Jupiter family comets*. Science, vol. 276: pp. 1670–1672.

M. J. Duncan, H. F. Levison & S. M. Budd (1995). *The Dynamical Structure of the Kuiper Belt*. The Astron. J., vol. 110: p. 3073.

K. E. Edgeworth (1938). *The evolution of the solar system*. Manuscript Nos. 19869/47 and /48.

K. E. Edgeworth (1943). *The evolution of our planetary system*. Journal of the British Astronomical Association, vol. 53: pp. 181–188.

K. E. Edgeworth (1944). *Origin of the Solar System*. Nature, vol. 153: pp. 140–141.

K. E. Edgeworth (1949). *The origin and evolution of the Solar System*. Mon. Not. R. Astron. Soc., vol. 109: pp. 600–609.

J. L. Elliot, S. D. Kern, K. B. Clancy, A. A. S. Gulbis, R. L. Millis, M. W. Buie, L. H. Wasserman, E. I. Chiang, A. B. Jordan, D. E. Trilling & K. J. Meech (2005). *The Deep Ecliptic Survey: A Search for Kuiper Belt Objects and Centaurs. II. Dynamical Classification, the Kuiper Belt Plane, and the Core Population*. The Astron. J., vol. 129: pp. 1117–1162.

J. A. Fernandez (1980). *On the existence of a comet belt beyond Neptune*. Mon. Not. R. Astron. Soc., vol. 192: pp. 481–491.

J. A. Fernández, T. Gallardo & A. Brunini (2004). *The scattered disk population as a source of Oort cloud comets: evaluation of its current and past role in populating the Oort cloud*. icarus, vol. 172: pp. 372–381.

J. A. Fernandez & W. H. Ip (1984). *Some dynamical aspects of the accretion of Uranus and Neptune - The exchange of orbital angular momentum with planetesimals*. Icarus, vol. 58: pp. 109–120.

R. A. Fisher (1925). *Statistical Methods For Research Workers*. Cosmo study guides. Cosmo Publications.

B. Gladman (2002). *Nomenclature in Kuiper Belt*. Highlights of Astronomy, vol. 12: pp. 193–198.

B. Gladman, M. Holman, T. Grav, J. Kavelaars, P. Nicholson, K. Aksnes & J. M. Petit (2002). *Evidence for an Extended Scattered Disk*. Icarus, vol. 157: pp. 269–279.

B. Gladman, J. J. Kavelaars, P. D. Nicholson, T. J. Loredo & J. A. Burns (1998). *Pencil-Beam Surveys for Faint Trans-Neptunian Objects*. The Astron. J., vol. 116: pp. 2042–2054.

B. Gladman, B. G. Marsden & C. Vanlaerhoven (2008). *The Solar System Beyond Neptune*, chap. Nomenclature in the Outer Solar System. University of Arizona Press, (pp. 43–57).

R. S. Gomes (2000). *Planetary Migration and Plutino Orbital Inclinations*. The Astron. J., vol. 120: pp. 2695–2707.

R. S. Gomes, A. Morbidelli & H. F. Levison (2004). *Planetary migration in a planetesimal disk: why did Neptune stop at 30 AU?* Icarus, vol. 170: pp. 492–507.

J. M. Hahn & R. Malhotra (1999). *Orbital Evolution of Planets Embedded in a Planetesimal Disk*. The Astron. J., vol. 117: pp. 3041–3053.

C. Hayashi (1981). *Structure of the Solar Nebula, Growth and Decay of Magnetic Fields and Effects of Magnetic and Turbulent Viscosities on the Nebula*. Progress of Theoretical Physics Supplement, vol. 70: pp. 35–53.

J. Heisler & S. Tremaine (1986). *The influence of the galactic tidal field on the Oort comet cloud*. icarus, vol. 65: pp. 13–26.

S. Howell (2006). *Handbook of CCD Astronomy*. Cambridge Observing Handbooks for Research Astronomers Series. Cambridge University Press.

D. Jewitt & J. Luu (1993). *Discovery of the candidate Kuiper belt object 1992 QB1*. Nature, vol. 362, no. 6422: pp. 730–732.

D. Jewitt, J. Luu & B. G. Marsden (1992). *1992 QB1*. IAU Circ., vol. 5611: p. 1.

D. Jewitt, J. Luu & B. G. Marsden (1993a). *1993 RO*. IAU Circ., vol. 5865: p. 1.

D. Jewitt, J. Luu & B. G. Marsden (1993b). *1993 RP*. IAU Circ., vol. 5867: p. 1.

D. Jewitt, J. Luu & C. Trujillo (1998). *Large Kuiper Belt Objects: The Mauna Kea 8K CCD Survey*. The Astron. J., vol. 115: pp. 2125–2135.

J. Kavelaars, L. Jones, B. Gladman, J. W. Parker & J. M. Petit (2008). *The Solar System Beyond Neptune*, chap. The Orbital and Spatial Distribution of the Kuiper Belt. University of Arizona Press, (pp. 59–69).

D. W. Kim, P. Protopapas, C. Alcock, Y. I. Byun, J. Kyeong, B. C. Lee, N. J. Wright, T. Axelrod, F. B. Bianco, W. P. Chen, N. K. Coehlo, K. H. Cook, R. Dave, S. K. King, T. Lee, M. J. Lehner, H. C. Lin, S. L. Marshall, R. Porrata, J. A. Rice, M. E. Schwamb, J. H. Wang, S. Y. Wang, C. Y. Wen & Z. W. Zhang (2010). *The Taiwan-American Occultation Survey Project Stellar Variability. I. Detection of Low-Amplitude δ Scuti Stars*. The Astron. J., vol. 139: pp. 757–764.

G. P. Kuiper (1951a). *On the Origin of the Solar System*. In *50th Anniversary of the Yerkes Observatory and Half a Century of Progress in Astrophysics*, edited by J. A. Hynek. (p. 357).

G. P. Kuiper (1951b). *On the Origin of the Solar System*. Proceedings of the National Academy of Science, vol. 37: pp. 1–14.

M. J. Lehner, C. Alcock, T. Axelrod, F. Bianco, Y. I. Byun, W. P. Chen, K. H. Cook, R. Dave, I. de Pater, J. Giammarco, S. K. King, T. Lee, J. Lissauer, S. L. Marshall, S. Mondal, T. Nihei, J. Rice, M. Schwamb, A. Wang, S. Y. Wang, C. Y. Wen & Z. W. Zhang (2006). *TAOS - The Taiwanese-American Occultation Survey*. Astronomische Nachrichten, vol. 327: p. 814.

M. J. Lehner, F. B. Bianco & T. C. Nihei (2008). *The TAOS Ligthcurve Generator Library*.

M. J. Lehner, N. K. Coehlo, Z. W. Zhang, F. B. Bianco, J. H. Wang, J. A. Rice, P. Protopapas, C. Alcock, T. Axelrod, Y. I. Byun, W. P. Chen, K. H. Cook, I. de Pater, D. W. Kim, S. K. King, T. Lee, S. L. Marshall, M. E. Schwamb, S. Y. Wang & C. Y. Wen (2010). *The TAOS Project: Statistical Analysis of Multi-Telescope Time Series Data*. Publ. Astron. Soc. Pac., vol. 122: pp. 959–975.

M. J. Lehner, S.-Y. Wang, P. Ho, T. Lee & C. Alcock (2007). *Program Project Proposal: TAOS-2 the next generation Taiwan American Occultation Survey.* Institute of Astronomy and Astrophysics - Academia Sinica.

M. J. Lehner, C. Y. Wen, J. H. Wang, S. L. Marshall, M. E. Schwamb, Z. W. Zhang, F. B. Bianco, J. Giammarco, R. Porrata, C. Alcock, T. Axelrod, Y. I. Byun, W. P. Chen, K. H. Cook, R. Dave, S. K. King, T. Lee, H. C. Lin, S. Y. Wang, J. A. Rice & I. de Pater (2009). *The Taiwanese-American Occultation Survey: The Multi-Telescope Robotic Observatory*. Publ. Astron. Soc. Pac., vol. 121: pp. 138–152.

A. O. Leuschner (1932). *The Astronomical Romance of Pluto*. Publ. Astron. Soc. Pac., vol. 44: p. 197.

H. F. Levison (1996). *Comet Taxonomy*. In *Completing the Inventory of the Solar System*, edited by T. Rettig & J. M. Hahn, vol. 107 of *Astronomical Society of the Pacific Conference Series*. (pp. 173–191).

C. L. Lin, Z. W. Zhang, W. P. Chen, S. K. King, H. C. Lin, J. H. Wang, S. Mondal, C. Alcock, T. Axelrod, F. B. Bianco, Y. I. Byun, N. K. Coehlo, K. H. Cook, R. Dave, I. de Pater, P. Descamps, M. J. Lehner, D. W. Kim, T. Lee, J. J. Lissauer, S. L. Marshall, R. Porrata, P. Protopapas, J. A. Rice, M. E. Schwamb, S. Y. Wang & C. Y. Wen (2009). *A Close Binary Star Resolved from Occultation by 87 Sylvia*. Publ. Astron. Soc. Pac., vol. 121: pp. 359–364.

P. Lowell & L. Observatory (1915). *Memoir on a trans-Neptunian planet*. Memoirs of the Lowell Observatory. T.P. Nichols.

J. Luu, D. Jewitt & B. G. Marsden (1993). *1993 FW*. IAU Circ., vol. 5730: p. 1.

J. X. Luu & D. Jewitt (1988). *A two-part search for slow-moving objects*. aj, vol. 95: pp. 1256–1262.

R. Malhotra (1993). *The origin of Pluto's peculiar orbit*. Nature, vol. 365: pp. 819–821.

R. Malhotra (1995). *The Origin of Pluto's Orbit: Implications for the Solar System Beyond Neptune*. The Astron. J., vol. 110: p. 420.

B. G. Marsden (1992). *1992 QB1*. IAU Circ., vol. 5633: p. 1.

R. Michel, J. Echevarría, R. Costero, O. Harris, J. Magallón & K. Escalante (2003). *Seeing Measurements at San Pedro Mártir Observatory using the DIMM Method*. Rev. Mex. Astron. y Astrof., vol. 39: pp. 291–301.

Minor-Planet-Center (2012). *MPC Database Search*. http://www.minorplanetcenter.net/search. Online; Accessed: 19/09/2012.

A. Morbidelli (2005). *Origin and Dynamical Evolution of Comets and their Reservoirs*. ArXiv Astrophysics e-prints.

A. Morbidelli & M. E. Brown (2004). *Comets II*, chap. The kuiper belt and the primordial evolution of the solar system. (pp. 175–191).

A. Morbidelli, V. V. Emel'yanenko & H. F. Levison (2004). *Origin and orbital distribution of the trans-Neptunian scattered disc*. Mon. Not. R. Astron. Soc., vol. 355: pp. 935–940.

K. Muinonen, E. Bowell & K. Lumme (1995). *Interrelating asteroid size, albedo, and magnitude distributions.* Astronomy and Astrophysics, vol. 293: pp. 948–952.

T. C. Nihei, M. J. Lehner, F. B. Bianco, S. K. King, J. M. Giammarco & C. Alcock. (2007). *Detectability of Occultations of Stars by Objects in the Kuiper Belt and Oort Cloud*. The Astron. J., vol. 134: pp. 1596–1612.

J. H. Oort (1950). *The structure of the cloud of comets surrounding the Solar System and a hypothesis concerning its origin*. Bulletin of the Astronomical Institutes of the Netherlands, vol. 11: pp. 91–110.

J. M. Petit, J. J. Kavelaars, B. J. Gladman, R. L. Jones, J. W. Parker, C. Van Laerhoven, P. Nicholson, G. Mars, P. Rousselot, O. Mousis, B. Marsden, A. Bieryla, M. Taylor, M. L. N. Ashby, P. Benavidez, A. Campo Bagatin &

G. Bernabeu (2011). *The Canada-France Ecliptic Plane Survey-Full Data Release: The Orbital Structure of the Kuiper Belt*. The Astron. J., vol. 142: 131.

F. Roques, M. Moncuquet & B. Sicardy (1987). *Stellar occultations by small bodies - Diffraction effects*. The Astron. J., vol. 93: pp. 1549–1558.

S. A. Stern (1995). *Collisional Time Scales in the Kuiper Disk and Their Implications*. The Astron. J., vol. 110: p. 856.

S. A. Stern (1996). *On the Collisional Environment, Accretion Time Scales, and Architecture of the Massive, Primordial Kuiper Belt.* The Astron. J., vol. 112: p. 1203.

TAOS-II (2012). *TAOS II*. http://taos2.asiaa.sinica.edu.tw/index.php. Online; Accessed: 14/12/2012.

C. W. Tombaugh (1946). *The Search for the Ninth Planet, Pluto*. Leaflet of the Astronomical Society of the Pacific, vol. 5: p. 73.

C. A. Trujillo & M. E. Brown (2002). *A Correlation between Inclination and Color in the Classical Kuiper Belt*. Astrophys. J., Lett., vol. 566: pp. L125–L128.

J. H. Wang, M. J. Lehner, Z. W. Zhang, F. B. Bianco, C. Alcock, W. P. Chen, T. Axelrod, Y. I. Byun, N. K. Coehlo, K. H. Cook, R. Dave, I. de Pater, R. Porrata, D. W. Kim, S. K. King, T. Lee, H. C. Lin, J. J. Lissauer, S. L. Marshall, P. Protopapas, J. A. Rice, M. E. Schwamb, S. Y. Wang & C. Y. Wen (2009). *Upper Limits on the Number of Small Bodies in Sedna-Like Orbits by the TAOS Project*. The Astron. J., vol. 138: pp. 1893–1901.

P. Wiegert & S. Tremaine (1999). *The Evolution of Long-Period Comets*. icarus, vol. 137: pp. 84–121.

I. P. Williams, A. Fitzsimmons & D. O'Ceallaigh (1993). *1993 SB and 1993 SC*. IAU Circ., vol. 5869: p. 1.

A. T. Young (1967). *Photometric error analysis. VI. Confirmation of Reiger's theory of scintillation*. The Astron. J., vol. 72: p. 747.

A. T. Young (1974). *3. Observational Technique and Data Reduction*. In *Astrophysics Optical and Infrared*, edited by N. Carleton, vol. 12, Part A of *Methods in Experimental Physics*. Academic Press, (pp. 123 – 192).

A. T. Young (1993). *Scintillation noise in CCD photometry*. The Observatory, vol. 113: pp. 41–42.

Z. W. Zhang, F. B. Bianco, M. J. Lehner, N. K. Coehlo, J. H. Wang, S. Mondal, C. Alcock, T. Axelrod, Y. I. Byun, W. P. Chen, K. H. Cook, R. Dave, I. de Pater, R. Porrata, D. W. Kim, S. K. King, T. Lee, H. C. Lin, J. J. Lissauer,

S. L. Marshall, P. Protopapas, J. A. Rice, M. E. Schwamb, S. Y. Wang & C. Y. Wen (2008). *First Results from the Taiwanese-American Occultation Survey (TAOS)*. Astrophys. J., Lett., vol. 685: pp. L157–L160.

Z. W. Zhang, D. W. Kim, J. H. Wang, M. J. Lehner, W. P. Chen, Y. I. Byun, C. Alcock, T. Axelrod, F. B. Bianco, N. K. Coehlo, K. H. Cook, R. Dave, I. de Pater, J. Giammarco, S. K. King, T. Lee, H. C. Lin, S. L. Marshall, R. Porrata, P. Protopapas, J. A. Rice, M. E. Schwamb, S. Y. Wang & C. Y. Wen (2009). *The TAOS Project: High-Speed Crowded Field Aperture Photometry*. Publ. Astron. Soc. Pac., vol. 121: pp. 1429–1439.

Z. W. Zhang, M. J. Lehner, J. H. Wang, C. Y. Wen, S. Y. Wang, S. K. King, Á. P. Granados, C. Alcock, T. Axelrod, F. B. Bianco, Y. I. Byun, W. P. Chen, N. K. Coehlo, K. H. Cook, I. de Pater, D. W. Kim, T. Lee, J. J. Lissauer, S. L. Marshall, P. Protopapas, J. A. Rice & M. E. Schwamb (2013). *The TAOS Project: Results From Seven Years of Survey Data*. Submitted to ApJ.